EXPERIMENTAL AND COMPUTATIONAL INVESTIGATIONS OF

CANDIDATE FUEL SALT MELT PROPERTIES AND CORROSION AND

IRRADIATION DAMAGE IN NICKEL FOR A MOLTEN CHLORIDE FISSION

SYSTEM

A Dissertation

by

ELIZABETH SHERIDAN SOOBY

Submitted to the Office of Graduate and Professional Studies of
Texas A&M University
in partial fulfillment of the requirements for the degree of

DOCTOR OF PHILOSOPHY

Chair of Committee,	Peter M. McIntyre
Committee Members,	Karl T. Hartwig
	Helmut G. Katzgraber
	Lin Shao
	Winfried Teizer
Head of Department,	George R. Welch

December 2014

Major Subject: Physics

ABSTRACT

A novel technology for accelerator-driven subcritical fission is being developed. A proton beam produces spallation and drives fission in a molten salt core. The motivation of the development is its capacity to destroy the transuranic elements in spent nuclear fuel and thereby provide a safe way to close the nuclear fuel cycle. Chloride-based transuranic salts have optimum properties for this purpose, and nickel appears to be attractive as a candidate material for the vessel structure.

The phase diagrams for the $NaCl$-UCl_3 and $NaCl$-UCl_3-$CeCl_3$ systems are investigated, in which Ce was used as a surrogate for Pu. Accurate measurements of the solidus and liquidus phase boundaries of each system are made using differential scanning calorimetry. Significant discrepancies are observed in comparison to previous results.

A remarkable phenomenon is observed in molten salt corrosion at the interface between chloride-based molten salt and pure nickel. Significant grain boundary etching is observed in all corrosion experiments, typical of salt corrosion; furthermore there is evidence of material transport during the corrosion process. Our hypothesis is that surface layer is formed in which Ni is continuously removed from and deposited onto the surface. The re-deposited layer is conformal even to the nano-scale, and appears to fill corroded grain boundaries.

An experiment is conducted in which radiation damage and molten salt corrosion are produced simultaneously on a nickel surface. Proton beam irradiation is used to simulate neutron damage, and the nickel sample is thinned to allow damage deposition characteristic of neutrons at the salt-nickel interface. It was concluded that heat

transfer will pose a difficult challenge for using ion-beam radiation as a stimulant to study appreciable radiation damage in molten salt-based systems.

DEDICATION

To my parents.

ACKNOWLEDGEMENTS

First and foremost, I thank my parents, Dr. Maureen Sheridan Fenton, the late Charles Sooby, and my stepfather Ray Fenton for their support and encouragement of my decision to pursue a Ph.D. in Physics. Their unwavering confidence in me is unparalleled in value. I cannot thank my fiancé Brandon enough for his support and encouragement throughout this process, particularly in the time I spent away, researching at Los Alamos. Special thanks are due to the rest of my family for keeping tabs on me while always showing their support, particularly my siblings Micah, Andrea, John, and Chris Fenton. I especially have to thank the handful of great friends who have stuck by my side through thick and thin along the road to this degree: Ann Blumer, Steven Feazel, Kim Fox, Katie Lewallen, and Todd Schneck. I don't know what I would have done without each of you keeping me sane and my spirits high, often times from across the country.

The scope of research detailed in this dissertation would not have been possible without the continued mentoring and support of Prof. Peter McIntyre, my dissertation adviser and PhD committee Chair. I would also like to thank Professors Kart T. Hartwig, Helmut Katzgraber, Lin Shao, and Winfied Teizer who each provided persistent support and encouragement throughout the degree process, proving to be exemplary committee members.

I have had tremendous support from our collaborators both domestically and abroad. Dr. Terry Holesinger, Ph.D. took me under his wing during my first graduate school summer in 2010, via an internship at Los Alamos National Laboratory. With him I completed my Master of Science research. During the summer of 2011, I worked with Prof. Mathieu Salanne of The University of Pierre and Marie Curie

2011. No office could possibly be as cozy as ours, disco ball included! She has not only been an excellent office/lab-mate, but she has also been a great friend whose family I have grown to adore. It goes without saying that Indara Suarez is crazy, but I must thank her for watching the cat from time to time and always remembering me when she shops for Swiss chocolate and Italian coffee. Likewise, without Shiner's Ruby Redbird and Messina Hof's Private Reserve Cabernet, Texas would be almost unbearable; special thanks go to each of these great Texas traditions. Special thanks are due to my roommate Ellie Figueroa for ensuring I never drank alone after a long day in the lab. I would also like to thank the Texas A&M Physics and Astronomy Department staff, faculty, and my fellow graduate students for their support during my enrollment.

Last but certainly not least, I acknowledge with my utmost appreciation the constant support of my best friend and soon-to-be husband, Brandon. He has been my rock for the last two and a half years, and I cant wait to see where our lives take us from here. Thank you for being patient with and supportive of me and this trying experience, honey.

TABLE OF CONTENTS

LIST OF TABLES

1. INTRODUCTION*

As an undergraduate physics student, science was described to me as the study of nature. The interaction of particles with matter has been at the forefront of physics research since its infancy. The Bohr model of the atom was the first to describe our building blocks of matter as a positively charged nucleus with negatively charged electrons orbiting this nucleus, similar to the orbital motion studied in astronomy and cosmology. Since the Bohr model was theorized in 1913, physicists have dug deeper into the structure of the atom. The trail of discoveries from protons, neutrons, electrons, quarks, leptons, to most recently the discovery of Higgs Boson spans 100 years of particle physics discoveries. Even though a vast amount of our physical world has been studied, scientists and engineers are still investigating the effects of elementary particle interactions with matter. Discussed in this dissertation will be the effect of irradiation damage and corrosion on metal lattices, the polarity of ions on bulk physical properties of ionic liquids, and ionic interactions on the phase behavior of compositions of salts.

1.1 Background

Nuclear power plants provide 11% of the world's electricity.[1] The 67,000 ton used nuclear fuel (UNF) inventory amassed by the US reactor fleet over the last 40+ years of operation, motivates the ongoing effort to develop and implement nuclear waste management protocols beyond short-term storage.[2] The Accelerator Research Laboratory (ARL) at Texas A&M University (TAMU) lead by Prof. Peter McIntyre is proposing a method for Accelerator based Destruction of Actinides in Molten

---

*Portions reproduced with permission from "Candidate molten salt investigation for an accelerator driven subcritical core," *Journal of Nuclear Materials*, 440,(2013) 298-303. Copyright 2013 Elsevier.

salt (ADAM) to burn transuranic (TRU) waste produced in conventional reactors.[3] ADAM marries two advanced technologies: 1) an Accelerator Driven System and 2) a Molten Salt Reactor. Each of these technologies have been studied in multiple countries during the last 20-50 years; therefore each have an intricate research and development history which I will introduce before elaborating on the specific design parameters of ADAM relevant to this dissertation work.

1.1.1   Accelerator Driven Systems

The concept of an Energy Amplifier (EA) was introduced by Carlo Rubbia and his team in 1993.[4] His original proposal described a method for the amplification of nuclear energy using "accelerator induced nuclear cascades" more commonly referred to as spallation. His proposal is the first to introduce the concept of a nuclear reactor driven by an external source. To continually produce power in a conventional reactor, a nuclear reaction chain must produce on average more neutrons in its reactions than initiated the reaction. To simplify: if you assume a single neutron generates one fission in each neutron-nucleus pair, then more than one neutron must be produced per reaction, when the entire ensemble is averaged. The multiplication factor, the ratio of the number neutrons post reaction to the number of neutrons prior to the reaction is k_{eff}, also referred to as the criticality factor. In a critical reactor k_{eff}=1. In a conventional reactor, $k_{eff} \geq 1$. Control rods are required in this configuration to keep the reactor multiplication factor from going super critical, a growing chain reaction, (also known as a bomb). The novelty of the EA proposal allowed for a supplemental neutron source. The reactor core can be inherently subcritical, and the additional neutrons are supplied by the accelerator via spallation.[4]

Rubbia mathematically described the neutron economy as:

$$N_{\text{tot}} = N_1 \sum_{n=1}^{n=\infty} k^{(n-1)} = \frac{N_1}{1-k} \qquad (1.1)$$

Where N_1 is the incident number of neutrons produced by the spallation source and k is related to the previously defined multiplication factor, k_{eff}.[4] Ensuring the reactor is inherently subcritical allows the accelerator to act as an on/off switch to the core. Once the accelerator is turned off, the supplemental neutron source is no longer active, and the core shuts down over time.[†]

Rubbia proposed either depleted uranium, (^{238}U), or natural thorium as the fertile fuel for his energy amplifier.[4] The Thorium fuel cycle was preferred, since Thorium is more naturally abundant than uranium and tends to breed less minor actinides. As I will discuss later, thorium fuel cycles are often proposed to enhance the energy production of a nuclear device though it is not ideal for transuranic waste destruction.

Rubbia's group demonstrated the EA concept experimentally in 1995 at CERN, exposing a sub-critical, water moderated nuclear system to a low intensity beam of energy 600 MeV up to 2.75 GeV.[5] They found the ratio of the energy produced by their driven device to the energy supplied by the proton beam to be 30. The results from this early experiment give physical validation to a large number of computation modeling efforts of ADS concepts.

The CERN team gave rise to an entirely new field for both accelerator and nuclear physicists as well as nuclear engineers. The proton driver of an ADS system should be engineered for reliability and beam sustainability. Popular criticisms of proposed ADS unity include beam trips and down time due to accelerator maintenance. Proton

---

[†]The above description is simplified for the sake of brevity. More factors are taken into account, particularly in the defining k. Moderators, delayed neutrons, and other key reactor configuration parameters must be taken into account. For a more in depth description of the reactor physics pertinent to accelerator driven systems, see ref [4].

beam power high enough to drive an efficient energy multiplier configuration is also a common knock on the ADS community. As a point of reference, a chart plotting beam power of existing accelerators and accelerator concepts is displayed in Figure 1.1.[6]
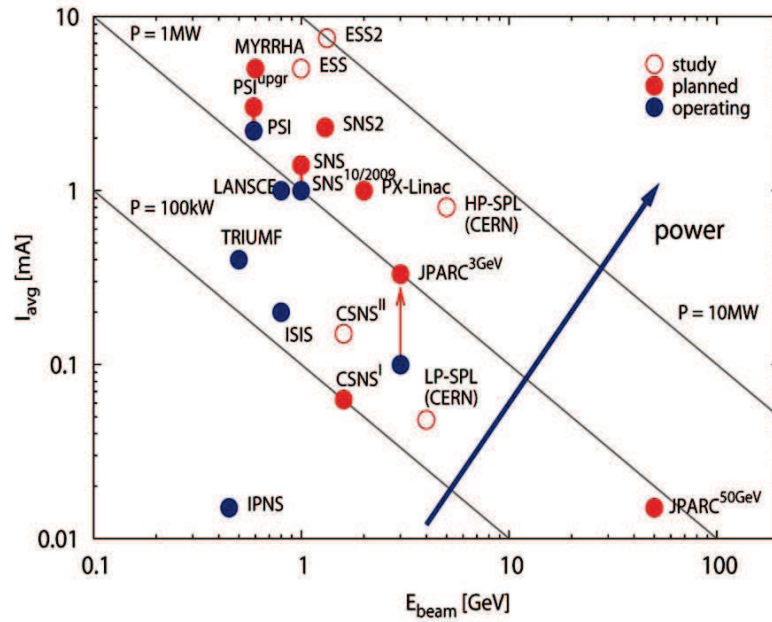
Figure 1.1: Displayed in this plot are the existing accelerators and accelerator concepts represented by their beam power capability. The x-axis is beam energy on a logarithmic scale.. The y-axis is beam current. Therefore the highest power accelerators are in towards the upper right quadrant. Multi-megawatt beam powers are necessary to drive an ADS system. Therefore, a new design is necessary.[6]

1.1.2   Molten Salt Reactor History

The Molten Salt Reactor Experiment (MSRE) paved the way for molten salt technology in the nuclear industry. After its four years of run time, the salt systems were only beginning to be understood. The MSRE, (composition: LiF-BeF_2-ZrF_4-UF_4,

65%-30%-5%-0.1%), ran from 1964-1969, following a four year design and development campaign. The reactor sustained 1.5 years of full power operation at 7 MW_{TH}. The primary vessel was made of Hastelloy-N, a high nickel-chrome alloy. The secondary coolant was also a fluoride-based salt, $LiF-BeF_2$.[7]

The MSRE proved to be a successful test of a mobile fuel concept, and a breeder design was proposed as a next step in the development efforts.[7] Unfortunately this effort was discontinued in 1976.[7] An over-head view of the MSRE can be seen in Figure 1.2.   A number of molten salt reactor (MSR) designs have been proposed since
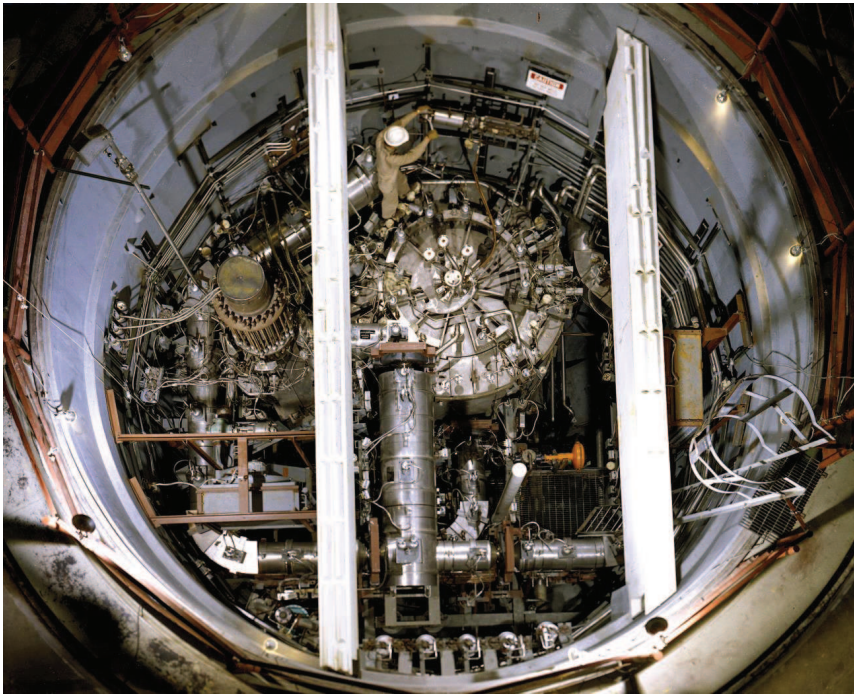
Figure 1.2: Rosenthal, 2010 displays an overhead image of the MRSE. The large dome to the upper right is the core. The intricate piping and pumping system displayed here illustrates the complex operating systems necessary. Image courtesy of Oak Ridge National Laboratory, U.S. Department of Energy.[8]

the MSRE. These concepts are typically optimized for one of two primary purposes: power production or transuranic waste burning. Several proposed thorium-cycle configurations are designed to minimize waste production while producing considerable amounts of power. These designs include Thorims-NES,[9] TIER,[10] TASSE,[11] and TMSR,[12] which are all optimized for power production with some Pu/TRU burning capabilities. AMSTER,[13] SPHINX,[14] and AMSB[15] are designed to be Pu/TRU burners. AMSTER is a critical reactor and the AMSB has to be paired with a concept like Thorims-NES, which is configured for power production;[9] the U/Th fluoride salt proposed in all of these designs can only contain a small mole percent of Pu(TRU) fluoride salts without high operating temperatures (700+ °C).

The issues common to fast-spectrum molten salt systems include high operating temperatures, limited actinide solubility, and restricted actinide burning rates. There are several benefits to designing an MSR to operate with a fluoride-based fuel salt. Fluoride salts are very well studied from both a computational modeling perspective as well as an experimental approach,demonstrated in the MSRE. Additional benefits include very low vapor pressures, a key property to maintaining a non-pressurized reactor. There is only one fluorine oxidation state, limiting the number of corrosion products which can form. It should be noted that the oxidation state of the halogen does not dominate the corrosion behavior of the salt, though it does simplify the computational modeling of such a system.

Primarily due to the limited actinide solubility in fluoride host salts, at practical operating temperatures (500-700 °C), a chloride host salt has been investigated by a number of MSR design groups. REBUS-3700 (a European fast spectrum molten salt reactor concept),[16] proposed to operate with a chloride molten salt system, which was then computationally evaluated in 2009 by Beneš. Beneš states the isothermal phase diagram of the $NaCl-UCl_3-PuCl_3$ indicates that any inlet temperature above 600 °C

for the REBUS allows for a broad composition map of a chloride salt reactor, with a significant molar % of plutonium to be dissolved into the fuel salt.[17] The larger solubility of plutonium and other transuranics in chloride salt systems permits a higher inventory of waste products to be transmuted in a fuel cycle. This one feature of the chloride salt system is critically enabling to any transmutation focused design.

The destruction of TRU requires that the core must not contain significant amounts of ^{238}U; the subsequent breeding of TRU would compete with TRU destruction. A TRU-burner must therefore either be fueled by only TRU or with a mixture of TRU and Th. The Japan Atomic Energy Research Institute (JAERI) proposed a NaCl-PuCl$_3$ subcritical core which was also driven by a proton driver in the 1990's.[18] The JAERI design optimized for TRU transmutation. The accelerator driver proposed in the model was a linear accelerator (LINAC), but the concept lost traction in Japan in the late 1990's, due to the growing popularity of solid, mixed oxide fuel fast reactors.

1.2 Motivation

1.2.1 Radiation Damage in Metals

To quantify the simultaneous effects of radiation damage and corrosion on metals, we must first understand each phenomenon separately. Radiation damage in metals can be described by basic scattering theory: a fast neutron displaces an atom from its position in the metal lattice. The radiation damage event causes a transfer of kinetic energy from the incident neutron to the lattice atom. This event is referred to as the "primary knock-on atom" (PKA).[19] The PKA displaces the atom, which goes on to create additional atom displacements. A cascade of displacements causes a collection of defects in the material and the event ends when the PKA settles in the lattice as an interstitial.[19] See Figure 1.3, where a face centered cubic lattice is displayed.

This cartoon shows the PKA in the third image and the interstitial-vacancy pair in the forth image. The bulk effects in the metal caused by radiation damage events
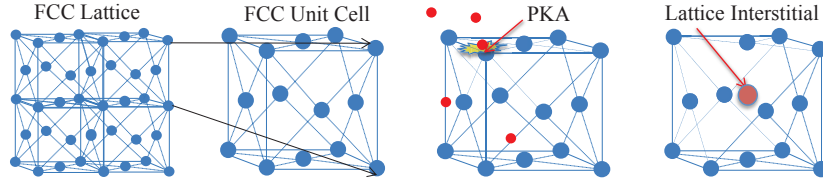
Figure 1.3: Diagram showing progression from the primary knock on atom to the lattice interstitial and vacancy pair.

(e.g. embrittlement, swelling, creep) result from the point defects and defect clusters caused by these neutron-atom interactions.

Fast spectrum reactor and fusion reactor R&D have been ongoing since the 1950's. Material selection for these applications is challenging due to the extent of radiation damage sustained by the structural components.[20] The primary factors which influence a material's bulk response to irradiation, pertaining to the source of radiation, are listed below:

1) **Type of irradiation: Ion, Neutron, Electron, or Photon**   Ionization and charged particle interactions dominate the energy transfer in an ion or electron collision with a nucleus. Focusing on only the recoil energy in this collision and not the interaction cross-section, neutron-particle interactions are dominated by kinetic energy transfer, rather than the ionization effects of the charged particles. Photons are likely to force the target atom into a momentarily excited state; however the kinetic energy transfer is relatively low as compared to other forms of irradiation

2)   Energy Spectra of the applied radiation   The energy spectra of the incident irradiation particles largely effects the type of reaction, (n,p), (n,γ), etc.

3)   Flux of irradiating particles through the material   The flux of irradiating particles will effect the rate of damage accumulation. In more recent years, irradiation rate has been a focus of attention among radiation materials scientists. With increased rate, the defects will accumulate before they can be annealed out in high temperature reactors. Likewise, when irradiating at increased rates, the damage implanted can be over estimated due to this lack of annealing.

These factors make up what I will refer to as the "radiation environment". Mimicking the irradiation environment of any reactor application is therefore a challenge, particularly the dose rate effect.

Computational modeling can partially bridge the gap between conceptual designs and their anticipated performance; however, experimental testing of these candidate materials is imperative to accurately predicting their behavior in the radiation environment for the duration of the service lifetime. It is important to produce a comparable radiation environment to the Accelerator-based Destruction of Actinides in Molten salt (ADAM).

In-core radiation is one method to expose a potential material to high neutron flux. In-core irradiation provides neutron damage uniformly across the sample. On the other hand the energy of the incident neutrons is much lower in the thermal-spectrum reactors which are most commonly available for materials testing. Fast-spectrum research reactors, such as BOR-60 in Russia,[21] can be used to deliver fast neutron damage for materials testing. Exposure of a sample to the extent of neutron damage it would sustain in a 50+ year lifetime in a fast reactor would take >20 years of in-core irradiation, making this an unrealistic route for preliminary

testing of candidate materials for novel applications. Spallation neutrons from high energy proton sources, such as those at the Spallation Neutron Source (SNS) and the Paul Scherrer Institute (PSI), can provide more rapid neutron damage doses;[22] even so, this increased rate can lead to effects which are not representative of the true radiation environment.

In 1969 the concept of charged particle simulation of neutron damage in metals was first realized.[23] Since then ion beam simulation of neutron damage in metals has become a prolific field. Heavy ion bombardment to simulate fast neutron damage advanced materials testing capabilities for these applications.[24, 25] Damage that once took years of irradiation exposure could now be simulated in a material in under an hour. Ions interact primarily through ionizing interactions with the orbital electrons, and this discrepancy limits the scope of phenomena attributed neutron damage can be validly simulated using an ion beam.

Was (2007) provides a mathematical description for each type of interaction relevant to this study.[19] Neutron-nucleus collisions are fundamentally different than ion-nucleus collisions. Because the neutron has no charge, its collision with a metal atom can be approximated by hard sphere collision kinetics mediated by the strong interaction. Equation (1.2) describes the average energy transfer from a hard-sphere potential mediated collision (Born-Mayer potential), like that of a neutron-nucleus collision.

$$\bar{T} = \frac{\gamma E_i}{2} \tag{1.2}$$

E_i is the incident energy of the radiation particle, a neutron in this case. For Equation (1.2) and the following equations γ is defined in Equation (1.3)

$$\gamma = \frac{4(M/m)}{(1 + \frac{M}{m})^2} \tag{1.3}$$

M is the mass of the target and m the mass of the incident particle.

Depending on the type of collision: elastic, inelastic, (n, 2n) where the incident neutron is absorbed and 2 neutrons are then ejected by the nucleus, or (n,γ) when the neutron is absorbed and a gamma particle is emitted, the energy transfer cross section can be derived.[19] For the case of ion-atom events, the collision is governed by interactions between electron clouds, the electron cloud and the nucleus, and between nuclei.[19] The Coulombic potential mediates the reaction kinetics for light ion collisions (e.g. protons), since the ion-atom event is dominated by charged particle interactions. The energy transfer in an ion-atom is described by simple Rutherford Scattering, an interaction governed by the Coulombic potential. The average energy transferred in one of these collisions is described in Equation (1.4).

$$\bar{T} \approx E_\mathrm{d} \ln(\frac{\gamma E_\mathrm{i}}{E_\mathrm{d}}) \tag{1.4}$$

E_d is defined as the displacement energy. When first referencing the damage to a lattice, the concept of an atom being displaced from its lattice position and becoming an interstitial was introduced. There is a threshold energy required to displace this atom, and that energy is E_d.

Within this dissertation work, I will attempt to simulate neutron damage using protons. Referring back to Equations (1.2) and (1.4), it is not evident that these can be correlated. In 1970's the concept of a universal unit to compare total doses of damage induced in a target material by either charged particle or neutron irradiation was introduced.[26] The DPA (displacements per atom) is the unit of total damage or dose that will be used here, (i.e. a 10 DPA dose describes a material in which all of its atoms have been displaced 10 times).

To quantify radiation damage, damage rate must first be calculated.[19] Was (2007) outlines the mathematical description of the damage rate, displayed here in Equation (1.5)

$$R_{\mathrm{d}} = N \int_{\check{E}}^{\hat{E}} \phi(E_{\mathrm{i}}) \sigma_{\mathrm{D}}(E_{\mathrm{i}}) dE_{\mathrm{i}} \tag{1.5}$$

N is defined as the lattice atom density, $\phi(E_{\mathrm{i}})$ is the particle flux, and $\sigma(E_i)$ the displacement cross section which is defined in Equation (1.6).

$$\sigma_D = \int_{\check{T}}^{\hat{T}} \sigma(E_{\mathrm{i}}, T) \nu(T) dT \tag{1.6}$$

Was (2007) goes on to describe $\sigma(\mathrm{E}_i, T)$ as the probability that an incident particle of energy E_{i} will cause a recoil of energy T (transferred energy). Lastly $\nu(T)$ is the resulting number of displaced atoms from the PKA.[19] More on how to calculate DPA can be found in Section 3 of this dissertation.

There are computational efforts across the globe attempting to model the defect structures formed by neutron and ion irradiation to approximate the effect to the structural material. Reactor testing can be expensive in both time and cost. There are very few research reactors remaining in the US, HFIR and ATR among them, however they are both cutting back on long term academic irradiation studies. BOR-60 in Russia is a great fast spectrum test reactor. Unfortunately there are political hurdles to testing there. Returning to the literature, there are some neutron damage studies assessing the effect of different doses and dose rates at various temperatures.

Budylkin et al investigated the strength and ductility of nickel as functions of temperature after irradiation to 70 DPA in a Russian test reactor.[27] Figure 1.4 displays results from their study. Increased strength and decreased elongation are common characteristics in irradiated materials- irradiation hardening. Ni and its
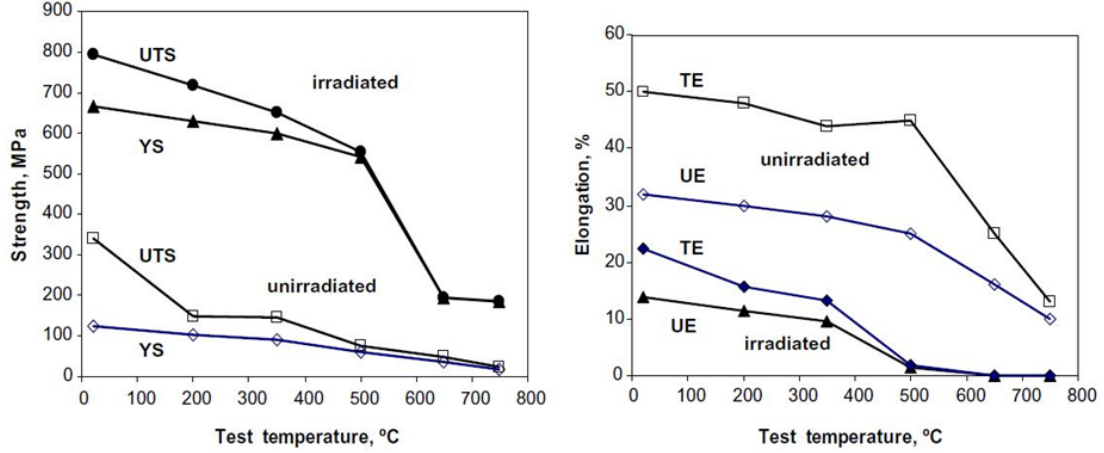
Figure 1.4: Ultimate Tensile Strength (UTS) and Yield Strength (YS) (left) and Total Elongation (TE) and Uniform Elongation (UE) (right) plotted for pure nickel samples both irradiated to 70 DPA and unirradiated as reported by Budylkin et al.[27]

alloys are susceptible to swelling from dislocations and void formation during irradiation as well as embrittlement from He formation at grain boundaries. In a thermal spectrum, the (n,α) reaction on ^{59}Ni is the primary source of He generation in Ni. Several studies have abandoned Ni and Ni-based alloys for fast-spectrum applications for this reason.[28]

As seen in Figure 1.5, the ^{59}Ni α reaction cross section has a peak around 200 eV.[‡] The ADAM spectrum has a reduced neutron fluence in this energy range. He generation is primarily driven by a ^{58}Ni (n,α) reaction in the spectrum from 1-10 MeV. This cross section is well below a barn, and therefore He embrittlement is mitigated by having an 'ultra' fast spectrum. Being an FCC material, nickel is prone to swelling in irradiation environments. At high temperature some of the effects which cause swelling can anneal (the interstitial finds its vacancy, for example). BCC materials, such as Nb, are less prone to these effects. Alloying and additives can be adopted into a material to help mitigate swelling.[30]

[‡]Cross Sections as reported in ENDF/B-VII.1

13
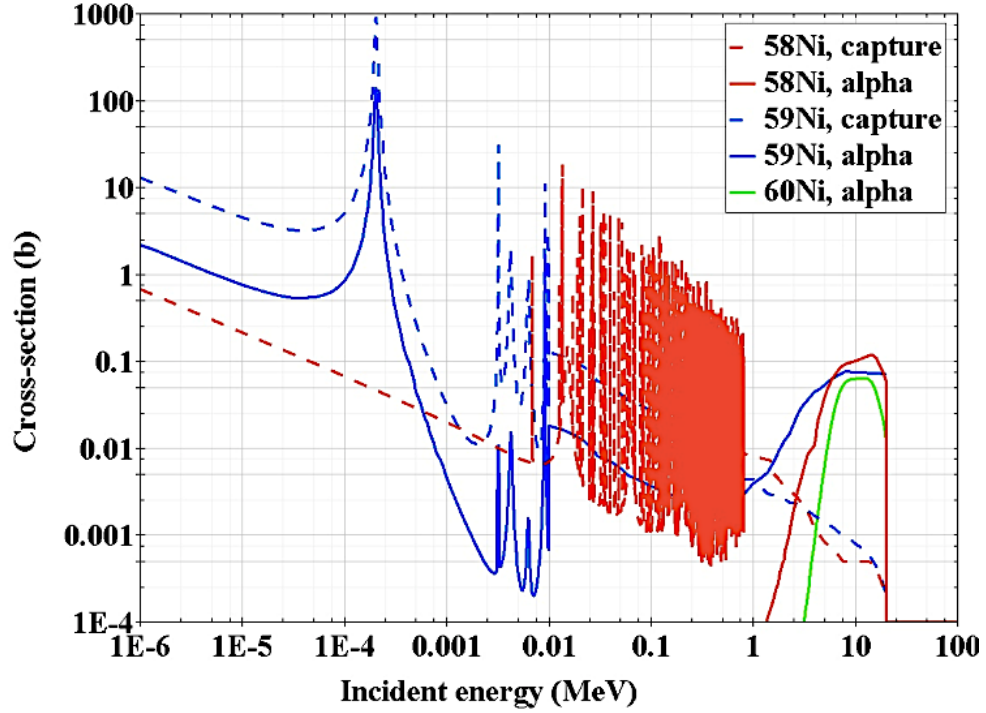
Figure 1.5: Reaction Cross Section vs. Incident Neutron Energy for Ni Isotope Capture and Decay.[29]

Along with radiation environment comes material activation. Activation is again dependent on the energy of the incident particles and the cross section for reactions. Niobium is initially investigated for a vessel material for its corrosion and swelling resistance. Unfortunately, the ^{93}Nb(n, γ) $\rightarrow$ ^{94}Nb is non-negligible, and ^{94}Nb has a 20,300 year, 2 MeV β^- half life.

1.2.2   Molten Salt Corrosion

The materials science and reaction chemistry of molten salt corrosion must first be understood before confidence in one material can be placed. The factors which affect the susceptibility of a material to corrosion are electrochemical, physical chemical, thermodynamic, and metallurgical. A great deal of preliminary structural material investigation for ADAM comes from the reports resulting from the materials and ce-

14

ramics studies from the Oakridge National Laboratory Molten Salt Reactor Program. While the MSRE and MSBR (Molten Salt Breeder Reactor) programs focused their studies to fluoride systems, the corrosion kinetics are similar to that in a chloride system. Utilizing both thermal-convection and forced-circulation loops, one study claims to confirm the relationship of time, alloy chromium content, and mass loss.[31] Previous studies assessed alloy corrosion by oxidation.[32,33] These studies concluded that the alloys were corroded by oxidation and shedding of the least nobel metal (e.g. Cr in Hastelloy-N).[32,33]

The molten halide salts play by a unique set of corrosion rules which are dominated by their ionic nature. When choosing a material which will be exposed to a high temperature (550 -700 °C) molten, halide salt, there are specific considerations. For example, unlike in aqueous solutions the corrosion of metals in molten salts can occur without oxidation of the metal ion.[34] Edeleanu outlines the corrosion driving phenomena: Redox potential Equilibration, metal nobility, and stability of metal halide.

Redox Potential Equilibration

Sridharan and Allen give a great discussion of the effect of the reduction-oxidation (REDOX) potential in a salt melt on the corrosivity of the salt on a vessel material. The REDOX potential is directly related to the valence states of the cation in the salt. Higher valence states drive corrosion, as they have more potential to reduce.[35] Sridharan and Allen give the example of the UF_4 to UF_3 transition driving Cr depletion in the MSRE via the reaction in Equation 1.7.[35]

$$Cr + 2UF_4 = 2UF_3 + CrF_2 \qquad (1.7)$$
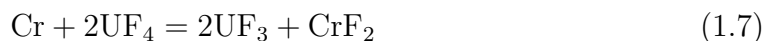
In the MSRE, extra UF_3 was added to drive Equation 1.7 to the left.[35] The redox potential of a salt can be experimentally measured as well as calculated via the Nernst equation, Equation (1.8), to predict corrosion due to shifts towards an oxidative salt. The lower the redox potential, (i.e. the more reducing), the less corrosive the salt.

$$e_M = e_M^\circ + 2.3\frac{RT}{2F}\log\left(\frac{[M^{+2}]}{[M]}\right) \tag{1.8}$$

However, if the redox potential is pushed to a fully reducing regime, reduction of actinide metal becomes a major concern.[35] While the 6 valence states of U still form chlorides, they are much less stable than the fluorides and therefore will not drive the kinds of redox shifts seen in the MSRE; though experimental measurements of the redox potential in a ADAM host salt are still necessary. The same stability caveat holds true for Am and Pu.

Metal Nobility

Several studies have confirmed that the presence of dissimilar metals in a molten salt melt can accelerate corrosion.[34–36] The oxidation reduction reaction that occurs is not actually between the host salt and the least noble metal, but rather between the primary material's corrosion product and the least noble metal. For example, in a nickel-chromium alloy, $NiCl_2$ will form in the salt and then the Ni will reduce and oxidize the Cr in the alloy via the reaction in Equation (1.9).

$$NiCl_2 + Cr \Rightarrow CrCl_2 + Ni \tag{1.9}$$

Then, additional $NiCl_2$ will form via galvanic corrosion to reach equilibrium, allowing the process to continue. The MSRE saw this as resulting in Cr leaching from Hastelloy-N and Ni plating in cold sections of the heat exchanger.

Stability of Metal Halide

The stability of the corrosion product is a strong determining factor in the corrosion kinetics. Likewise the stability of the host salt will determine the equilibrium concentration of the corrosion product in the salt.

The University of Wisconsin-Madison has teamed up with INL to studied both corrosion and heat transfer of chloride and fluoride molten salts. Olson (2009) provides a thorough explanation of the halide corrosion mechanisms, how it can be minimized, and how it varies in fluorides and chlorides.[36] Studying the Gibbs Free Energy of Formation for a number of chloride and fluoride corrosion products ($CrCl_2$ for example), one finds that the chloride corrosion products are comparably stable to the fluorides. However, the host salt Gibbs Free Energies differ significantly. KCl is less stable than KF, for example, and therefore the $\triangle G$ of reaction in the fluoride system is greater, and therefore more energetically favored than the chloride case.[36] Figure 1.6[§] plots the Gibbs Free Energies of Formation as functions of temperature for both fluoride and chloride host salts. Table 1.1[¶] lists the Gibbs Free Energies of Formation for a number of chloride host salts and corrosion products.

Table 1.1: Gibbs Free Energies of Formation for Common Chloride Host Salts and Corrosion Products at 600 °C.

Host Salt Chloride Compound	Free Energy of Formation kcal/mol-Cl	Corrosion Product Chloride Compound	Free Energy of Formation kcal/mol-Cl
KCl	-84	$AlCl_3$	-42
LiCl	-80	$CrCl_2$	-34
NaCl	-79	$FeCl_2$	-28
$PuCl_3$	-61	$NiCl_2$	-21
$MgCl_2$	-60	$MoCl_2$	-19
UCl_3	-54	WCl_2	-15

[§]Calculated using HSC Chemistry 7.1 software.
[¶]Calculated using HSC Chemistry 7.1 software.
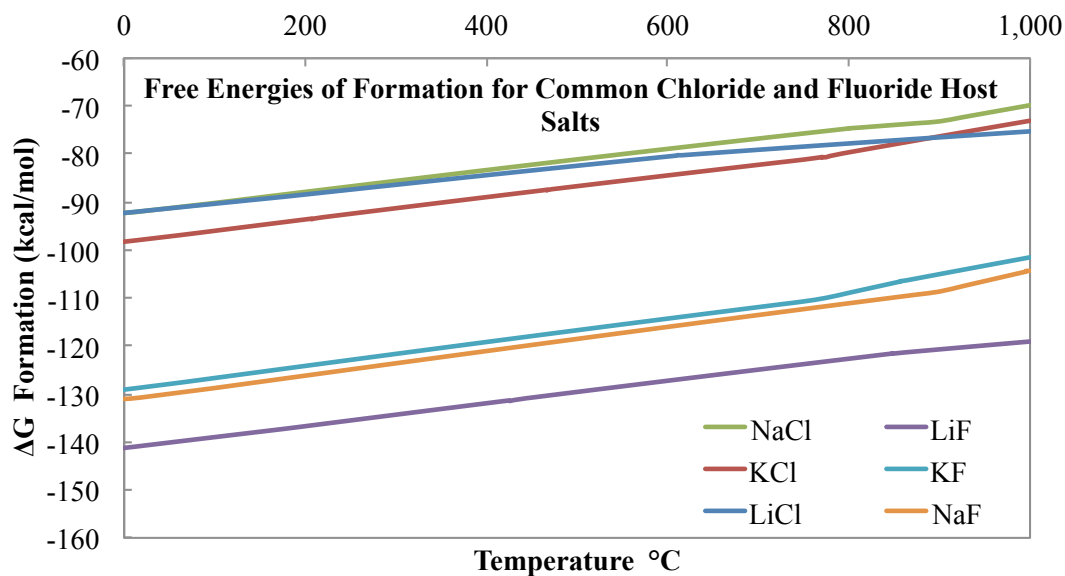
Figure 1.6: Plotted are the Gibbs Free Energies of Formation as functions of temperature for common chloride and fluoride host salts. The lower stability (less Gibbs-negative) of the chlorides can actually lower the susceptibility of metals to corrosion in chlorides.

The more stable (Gibbs negative per mol Cl) the corrosion product, the more likely it is to form in a given melt. Al will be the most energetically favorable corrosion product or the ones listed here. Unlike the passivating oxide layer typically associated with Al alloys, $AlCl_3$ will be appreciably soluble in the molten salt melt. Al would not be a good choice for vessel material in the case of a UCl_3 fueled reactor as that equilibrium condition can drive more corrosion than compared to W in a KCl melt. For alloys, even if the primary alloying element is not energetically favored to chemically oxidize, corrosion can be driven galvanically as discussed earlier. Also, the stability can adjust the REDOX potential of the overall melt.

These energies of formation are also a function of temperature. Figure 1.7 [∥]plots the Gibbs Free Energies of Formation for common chloride corrosion products as functions of temperature.
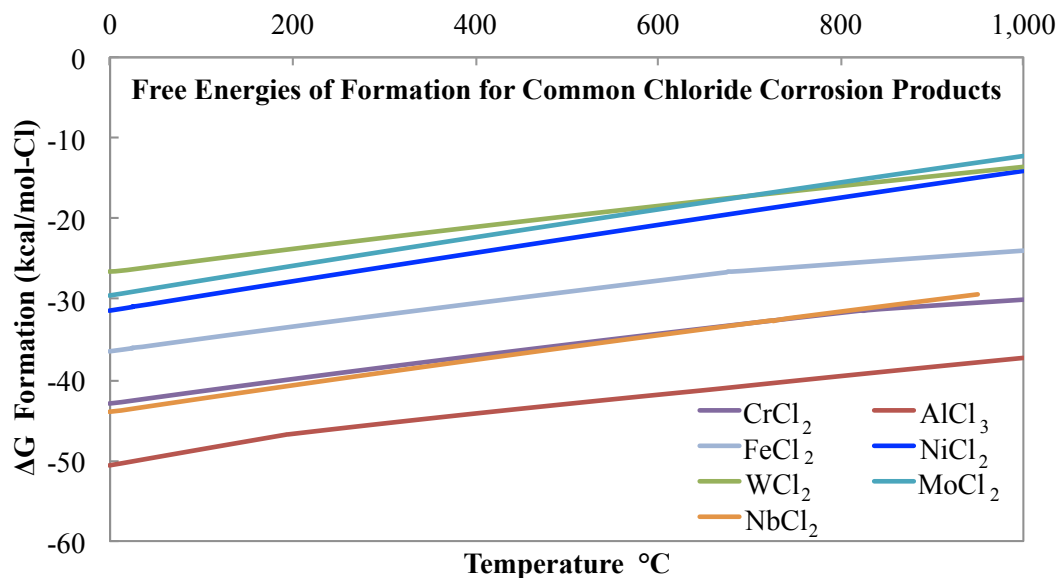
Figure 1.7: Plotted are the Gibbs Free Energies of Formation as functions of temperature for common chloride corrosion products. The products become less stable at higher temperatures as Cl_2 gas becomes more stable.

The $FeCl_2$ trend can be misleading. While that individual chloride has similar energetics to nickel, it also forms $FeCl_3$ with a similar kcal/mol-Cl $\triangle G$. Nickel, which is typically proposed for molten salt applications, has only one stable chloride with a relatively low $\triangle G$.

Impurities are the biggest driver of corrosion in molten salts.[34,35] The impurities can be either in the salt, (water and oxides), or in the metal (sulfur, in particular). Water causes a particular problem. HCl can form and that chemical itself is very

[∥]Calculated using HSC Chemistry 7.1 software.

corrosive to most metals. The MSRE observed that the fission product tellurium was a strong corrosion driver, as it migrated up grain boundaries.[33] A resulting study investigated adapting Hastelloy-N to be more resistive to irradiation embrittlement and grain boundary attack by tellurium.[33] From initial neutronics calculations, ADAM will produce tellurium in comparable amounts; however there will be a constant effort to separate and remove fission products from the core. The ORNL study proposed alloying Hastelloy-N with 1-3% Nb. Though, the results of this study were inconclusive, as funding was cut to the program.

Oxides pose a big threat to corrosion in molten chloride salts. A particular example outlined by the Japanese in 1997 noted the favorable formation of NdOCl, an oxy-chloride, via the reaction described in Equation (1.10).[37]

$$NiO + NdCl_3 \Rightarrow NiCl_2 + NdOCl \qquad (1.10)$$

Assessing the other actinides, the same reaction will occur with UCl_3 in the presence of NiO. Even more energetically favorable is the same reactions but with FeO rather than NiO. Therefore, it is not so much oxygen as a contaminant, but rather surface oxides present on the vessel before introduction to the salt melt.

As pure oxidation of the vessel material is not the route to corrosion in chlorides, but rather galvanic corrosion and impurity driven corrosion, the majority of the material loss occurs in the early lifetime of the vessel liners. This point is represented well in the bilinear nature reported in K. Sridharan and T. R. Allen's chapter, "Corrosion in Molten Salts," which compiles a wealth of data from the MSRE testing of vessel materials in fluoride salts.[35] The impurity driven corrosion period is stated as lasting up to 250 hours, then the material loss rate reduces dramatically. Therefore, to test corrosion of vessel materials, like metals, pure salt compounds, dry atmo-

spheres, and clean/etched sample surfaces are requisite to avoid year-long corrosion testing.

2. ACCELERATOR-BASED DESTRUCTION OF ACTINIDES IN MOLTEN SALT*

Marrying the two concepts discussed in the first part of Section 1, ADAM is an accelerator driven molten salt reactor. The accelerator acts as the on/off switch to fission, supplying the additional neutrons for power production. The molten salt is both the spallation target and the reactor fuel. The fuel-salt is circulated around the core and through the heat exchanger, though never leaving the primary containment vessel. A CAD drawing of the core as presented by the ARL team in 2013 is displayed in Figure 2.1.[38] Labeled are a handful of key components to this single ADAM Core. The primary heat exchanger fluid is LiCl-KCl eutectic, which is a low melt chloride salt commonly used in pyroprocessing. Three beam windows are submerged into the molten salt core. Through each of these windows passes a 4 mA, 800 MeV proton beam. Spallation occurs in the salt, with the dense fuel salt acting as the spallation target. A cartoon of the spallation process is displayed in Figure 2.2

The core is optimized to have a burn rate equivalent to 5.6% of its transuranic inventory per year, leading to a total of 18 years of optimal operation to destroy the transuranic contents of the originally fueled core.[38] Transuranic salt must be added regularly to sustain k_{eff} and keep the burn rate at 5.6% as the inventory depletes.

Three of the cores described in Figure 2.1 are incorporated in the ADAM system. A strong focusing cyclotron delivers three lines of 12 mA beam current to each core, distributed in the three beam windows.[38]
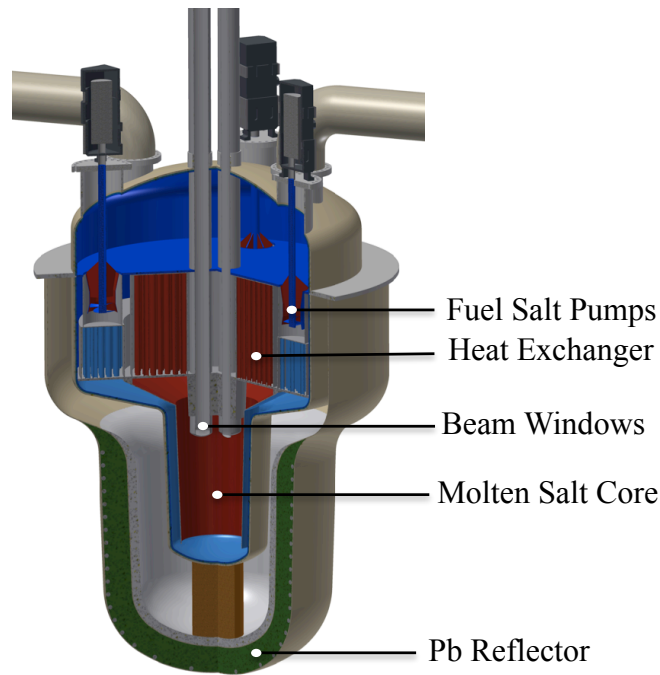
Figure 2.1: CAD drawing of an ADAM molten salt core. Three beam windows each deliver 4 mA, 800 MeV proton beams into the dense fuel-salt spallation target. Molten salt pumps circulate the fuel salt around the core to the primary heat exchanger, where a LiCl-KCl coolant salt contained in U-tubes takes away the excess heat. No fuel salt ever leaves the core during normal operation.
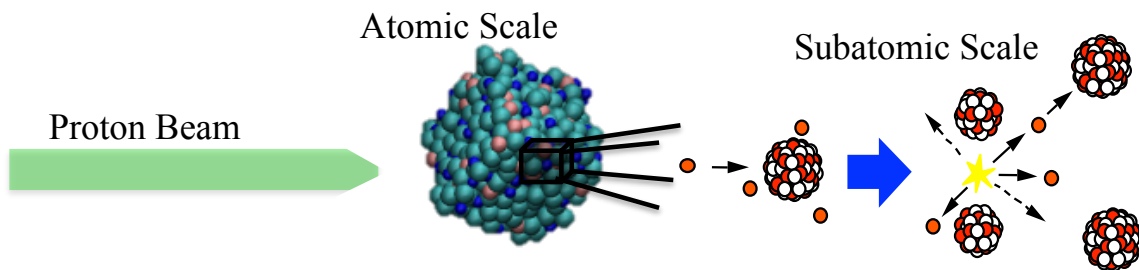
Figure 2.2: Cartoon describing spallation in the ADAM core, once the beam has passed through the beam window. The 'atomic scale' image is an MD simulation of the actinide salt. The large red and white items to the far right are the individual heavy nuclei breaking into small nuclei via fission induced by spallation neutrons.

2.1 Strong Focusing Cyclotron for Enhanced Beam Power: The Driver

An accelerator complex comprised of two strong focusing cyclotrons supplies the beam power to the core. A diagram of the conceptual accelerator complex is displayed in Figure 2.3 as it is reported by ARL in 2013.[38]
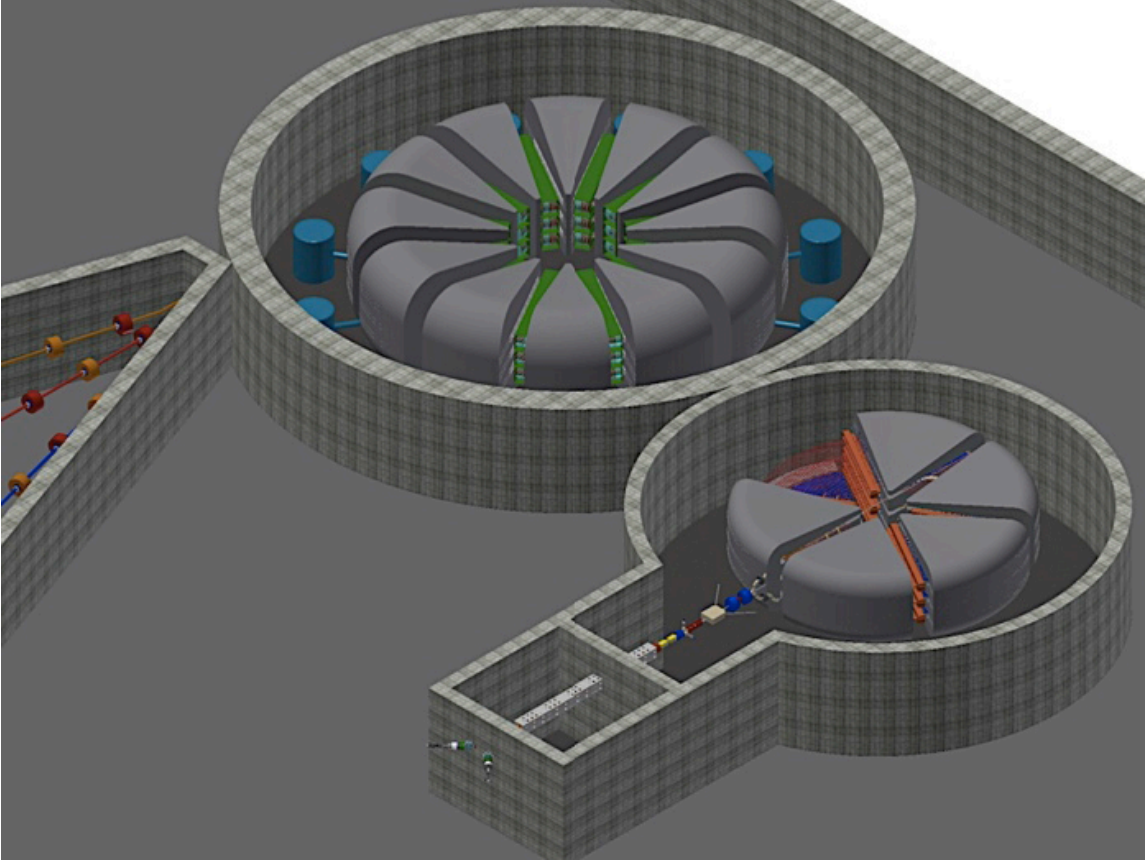
Figure 2.3: CAD drawing of the ADAM accelerator complex. An injector feeds the TAMU100, the smaller of the two cyclotrons. The TAMU 100 accelerates the injected protons to 100 MeV. The 100 MeV proton beams are then injected into the TAMU800 which accelerates these 100 MeV protons to 800 MeV. The resulting three beam lines are transfered to the cores via a 'switch yard.'[38]

The cyclotrons are designed to supply the enough beam power to the core to drive fission, and with that introduces the need to have one cyclotron footprint that has the power of three combined beam orbits. A cutaway of the conceptual TAMU100 3-stack as most recently reported,[38] is displayed in Figure 2.4.
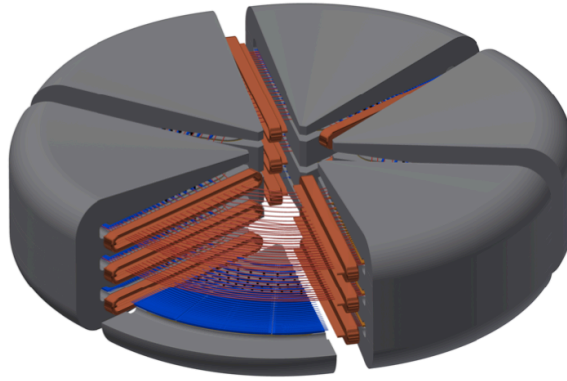
Figure 2.4: CAD drawing of the TAMU-100, a flux-couple cyclotron which feeds the TAMU800. Three individual beam planes exist in the same flux-coupled magnetic field.

The primary focus of this dissertation lies in the molten salt core, which is fed by the accelerator complex. More on the accelerator facility, design, and R&D can be found in the ARL group's publications.[38,39]

2.2 Molten Salt Fuel Selection: The Core

The molten salt core consists of actinides dissolved into a NaCl host salt. A chloride-based molten salt has been chosen for a number of reasons. As discussed earlier in Section 1 of this dissertation, there are a large number of fluoride salt reactors proposed. The primary advantage of chlorides over fluorides is the actinide solubility at comparatively low temperatures. Table 2.1 summarizes some of the

primary points of comparison between these two salt systems. Although chloride

Table 2.1: Comparison of Chlorides and Fluorides

	Fluorides	Chlorides
Actinide Solubility at Acceptable Temperature	Low	High
Vapor Pressure	Very Low	Low
Operating Temperature	700 °C+	500 °C+
Electro-negativity (Pauling Scale)	3.98	3.16
Number of Oxidation States	1	8
Number of Stable Actinide Ionization States	Several	1

salts will prove to have a more complex corrosion chemistry than fluorides due to the increased number of oxidation states, studies have shown that chloride salts are not as chemically aggressive and are less corrosive.[36,40] In addition, chlorides have higher actinide solubility at lower melt temperatures than fluoride salts.[41] This allows for a substantial actinide content to be dissolved in the NaCl molten salt, which aids in optimizing the fast neutronics.

Chlorides do, however, pose a couple of additional issues. ^{36}Cl (0.3 Myr. half-life) production posed a problem for proposed chloride molten salt reactors in the past. Although ^{35}Cl has a significant capture cross-section, the neutron captures are predominantly of thermal neutrons and thus actually help in hardening the neutron spectrum. The amount of sulfur produced in the year equates to 265 g and is primarily produced by (n,p) reactions from ^{35}Cl. Sulfur poses as a corrosion driving contaminant in the salt system, facilitating the formation of sulfides in the salt. As displayed in Figure 2.5, a secular equilibrium is reached for S in approximately one year, where the rate of production is equal to the decay rate of S to ^{35}Cl.
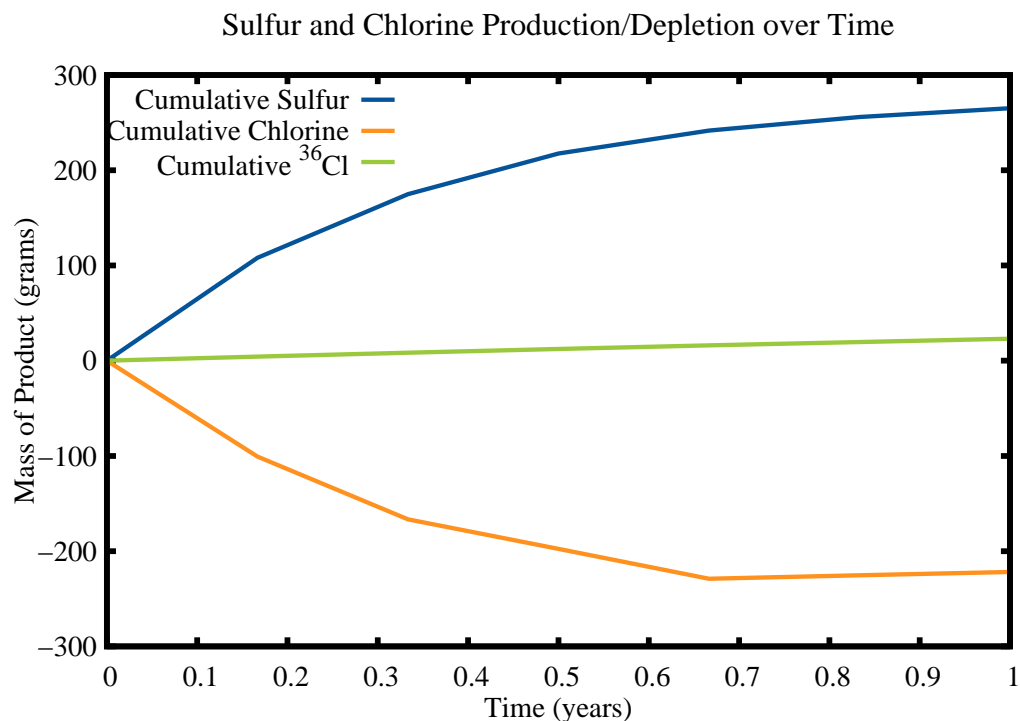
Figure 2.5: The production of Sulfur in a single ADAM core in one year (blue) plotted with the ^{36}Cl production and total Chlorine destruction. Total production amounts are 265 g S (total), -222 g Cl (total), and 23 g ^{36}Cl.

Molten salt cores possess inherent complications including, but not limited to, oxide precipitation, redox potential fluctuations, volatile gas formation, and fission product solubility limits. Oxide control is a priority for both fluoride and chloride molten salt cores. Oxides can form from either the presence of free oxygen or from oxide dissolution into the salt from either the vessel materials or heat exchanger materials. Free oxygen in the salt will cause the actinides to precipitate as oxides. These precipitates can become a major issue if the resulting oxides were to agglomerate and deposit on the walls of the vessel, creating hot spots.

The MSRE also faced this concern, with uranium as the fissile material. One solution to this problem is to incorporate an "oxygen getter" to the salt composition. ZrF_4 was used in the MSRE to prevent UO_2 production.[42] An analog to this technique is not feasible for the ADAM core as $ZrCl_4$ will volatilize in our operating temperature range. A quick investigation of the chemistries of similar metals provides no obvious chemical oxygen getter for chloride salts. Other methods must be adapted; (i.e. sacrificial anodes or metal additives to the salt which will preferentially oxidize). Further research is necessary to solve this problem; however minimizing the availability of pure oxygen in the salt will be a necessary first step to solving this issue.

Host salts such as LiCl, KCl, and the corresponding eutectic are not suitable for a fast spectrum core. Li moderates the system, and there is a ^{39}K (n,α) reaction which produces ^{36}Cl readily in the ADAM spectrum. NaCl has been modeled with actinides in previous studies and there has been a modest experimental effort in the past. However, there is a lack of experimental data for physical and thermal transport properties in salts with actinide chlorides. In order to estimate the properties of candidate salt systems needed for the ADAM design, the collaboration has turned to a well-proven Molecular Dynamics (MD) code which will be discussed in more detail in Section 3 of this dissertation.

The fission products produced during the lifetime of ADAM comprise transition metals, noble gases, lanthanides, halides, and rare earths. All of these, with the exception of the noble gases (Xe and Kr), form chlorides or other halides in the ADAM operating temperature range. The primary question is whether or not these fission products will dissolve in the salt, volatilize, or precipitate out of solution. For example, cesium forms several stable halides in the ADAM operating temperature, though which species will form in the salt will be determined by halide availability.

More than likely, CsCl will form, as many of other fission products have M^{+2} states. Technetium is of primary concern, as it will need to be separated from the salt pot. The energetically favored chloride, $TcCl_5$, is volatile at our operating temperature range. The volatile fission production necessitates further understanding of gas solubility in the salt. Furthermore, will $TcCl_5$ be dissolved in the salt as a gas, or will it come off as a gas and be able to be removed? A similar question can be posed for the iodides and other volatile halide fission products. During operation of the MSRE, a continuous flow of helium was used to remove fission product gases as well as any stray oxygen and other contaminants.[40] The gases then passed through charcoal scrubbers. Experimental work will have to be performed to confirm a similar gas sparging technique can be used on ADAM fuel salts.

Lastly, reduction/oxidation potential (redox potential) monitoring and control can help to limit corrosion and control salt composition.[40] The redox nature of the salt influences the amount of material loss due to galvanic corrosion, since the molten salt is an electrolyte. While many groups have discussed redox potential control in fluorides by either adding a stabilizing component to the salt or electrolytically controlling the potential of the salt, very little work has been done with the chlorides. The primary driver of redox fluctuations in fluoride MSR designs is the UF_4/UF_3 ratio. In the ADAM core, there is very little U content. Therefore, the ADAM core already has a significantly decreased issue concerning redox equilibration. More on the REDOX potential of the ADAM core salt can be found at the end of Section 1 of this dissertation.

In the end, the best way to settle on the specific fuel salt for the ADAM core is to combine computational modeling with experimentation. Section 3 of this dissertation will go into the various modeling techniques employed to help answer some of

these questions, and Section 4 contains the details of salt synthesis routes and phase diagram experimental investigations.

3. ENABLING COMPUTATIONAL TECHNIQUES[*]

3.1 Molecular Dynamics

A polarizable ion model (PIM)[43,44] has been developed by Madden and collaborators to model ionic liquids, including both fluoride and chloride molten salt systems.[45–48] We are using their model to estimate density, thermal conductivity, heat capacity, viscosity, and electrical conductivity of candidate molten salt systems for ADAM. These physical and transport properties are crucial to modeling the neutronic behavior and heat transport properties of the ADAM core.

There are five fundamental interactions which govern the behavior of ionic liquids. These factors are described below and can be found in Madden and Wilson's work from 2006:[44]

1. **Intermolecular Bonds**

The PIM model does not take into account intermolecular bonding. For a molecular dynamics model of an ionic liquid, the repulsive and electrostatic properties of the two ions (e.g. Be^{+2} and F^{-1}) more accurately describe this "bond", from a physical point of view, than the typical covalent bond. In short, we are not ignoring the intermolecular interactions, but rather not describing them as covalent bonds.

2. **Repulsive**

This could comprise the largest portion of the interaction potential. It is usually morphed from the hard-sphere potential.

$$V_{\text{repulsion}} = \sum_{i,j>i} B^{ij} \exp(-a^{ij} r^{ij}) \qquad (3.1)$$

3. **Dispersion**

The dispersion term has a very small impact on the ionic system's interaction potential; however it plays a large role in predicting density. It is an attractive potential.

$$V_{\text{dispersion}} = -\sum_{i,j>i}[f_6^{ij}\frac{C_6^{ij}}{(r^{ij})^6} + f_8^{ij}\frac{C_8^{ij}}{(r^{ij})^8}] \tag{3.2}$$

4. **Electrostatics**

The electrostatic potential describes the charge-charge interaction. It is described by the Coulombic potential. The electrostatic and the repulsive potentials essentially "make" a molten salt.

$$V_{\text{charge-charge}} = \sum_{i,j>i}\frac{q^i q^j}{r^{ij}} \tag{3.3}$$

5. **Polarization Effects**

Like the dispersion potential, polarization effects play small but crucial roles in making this model physical. For example, without this polarization potential, a molecule like Be_2F would align itself as seen in Figure 3.1. However, this is grossly
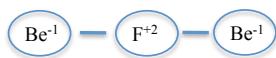
Figure 3.1: Example of the bond structure modeling ionic bonding without polarization effects.

unphysical. Because the fluoride atom is polarized, the molecule really should be modeled with the F ions polarization, see Figure 3.2. The polarization potential is
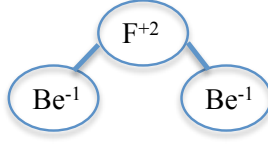
Figure 3.2: Example of the bond structure when properly modeling ionic bonding with polarization effects.

displayed in Equation (3.4).

$$V_{\text{pol.}} = -\sum_{i,j>i}(q^i\mu_\alpha^j g_D^{ij}(r^{ij}) - q^j\mu_\alpha^i g_D^{ji}(r^{ij})) \bigtriangledown_\alpha \frac{1}{r^{ij}} \sum_{i,j>i} -\mu_\alpha^i\mu_\beta^j \bigtriangledown_\alpha \bigtriangledown_\beta \frac{1}{r^{ij}} + \sum_i \frac{1}{2\alpha^i \mid \vec{\mu}^i \mid^2}$$

(3.4)

From these potentials described mathematically in Equations (3.1)-(3.4), the equation of motion can be solved at every time step throughout a given simulation via a familiar Equation (3.5)

$$m^i\dot{\vec{v}} = \sum_{j\neq i}\vec{F}^{j\rightarrow i} = -\frac{\delta V}{\delta \vec{r}^i}$$

(3.5)

The MD code accepts an input file, and within the input file the user must define the parameters which describe each of these interaction potentials. These potentials are solved for via DFT calculations made over time prior to the implementation into the PIM code. For example, the parameters used to simulate the ADAM fuel salt are listed in Table 3.1.

The PIM code is not a "plug-and-chug" analytical code. Massagin of the run parameters is necessary to model a physical system. A canonical ensemble is used in this particular MD model. To begin a given simulation, the scientist must decide if NVT or NPT is appropriate. For example, when calculating density, the number of particles, pressure, and temperature must be held constant. Setting the number

Table 3.1: Interaction Potential Parameters for ADAM Fuel Salt

Interaction	Source	van der Interactions alpha (a)	Waals (a.u.) A	C6	C8	b6	b8	Polarization Interactions b	(a.u.) c(-+)	c(+-)	Polar. (1st Ion)	Polar. (2nd ion)
Cl-Cl	48	1.53	100	222.26	7455.5	1.7	1.7	1	0	0	20	20
Na-Cl	45	1.726	67.5	37.4	167.3	1.7	1.7	1.76	3	0.697	0.89	20
Na-Na	45	5	1	10	100	1.7	1.7	1	0	0	0.89	0.89
U-Cl	48	1.8	400	97.2	600	1.5	1	1.258	1	1	0	20
U-U	48	3	15	47.7	100	1.5	1	1	0	0	0	0
La(Pu)-Cl	48	1.8	450	97.22	600	1.5	1	1.258	1	1	0	20
La(Pu)-La(Pu)	48	3	15	47.7	100	1.5	1	1	0	0	0	0

of particles, lattice spacing, the appropriate thermostat, and barostat, the program knows to allow the cell volume to adjust to the equilibrium state of the system. When calculating heat capacity at constant volume, we refer back to thermodynamics in Equation (3.6).

$$\left(\frac{\delta U}{\delta T}\right)_V = \left(\frac{\delta U}{\delta T}\right)_V = C_v \tag{3.6}$$

The MD modeling builds on the previous work by Madden et al., who have developed a reliable interaction potential for UCl_3[49] and related compounds[50,51] in the framework of the polarizable ion model. The potentials were tested against available experimental data and they were shown to reproduce them very accurately. In particular the structure and the viscosity of UCl_3 were reproduced with a high degree of accuracy.[49] Recently, a group has shown that these models were able to very accurately predict the activity coefficients, which are usually difficult to simulate.[48]

The density of the fuel salt plays a crucial role in neutronic calculations. Therefore, we have checked the ability of the model to determine the density of $NaCl$-UCl_3 melts of various compositions. The model calculations were compared with experimental data[52] as displayed in Figure 3.3.

The complexity of the ADAM molten salt system would require a very large number of ions and ionic species to be introduced to the MD simulation. Interaction potentials are not available for many of the transuranics and lanthanides in the salt system. Therefore surrogates have to be employed, particularly La for the transuranics. For the present model, the computational cell is simplified by modeling the $NaCl$-$TRUCl_3$-$LnCl_3$ salt as $NaCl$-$PuCl_3$-$LaCl_3$.

The primary reason to use Lanthanum as a surrogate for Plutonium is the availability of interaction coefficients for a $LaCl_3$ system in the presence of $NaCl$ and UCl_3. According to both computational and experimental studies performed for ac-
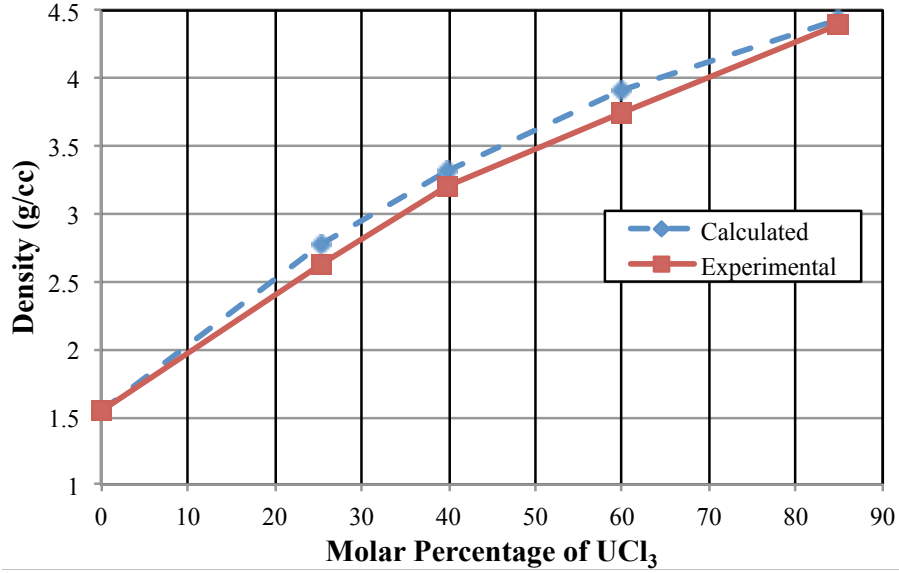
Figure 3.3: Density (g/cc) of a series of NaCl-UCl$_3$ compositions. Experimental data was extracted from reference.[52]

tinide chemistry, cation crystallographic radius and activity coefficient are linearly correlated.[48,53] Looking at the solid state bond distance between Pu-Cl and La-Cl in the PuCl$_3$ and LaCl$_3$ systems, we see only a 0.6% difference between the average Pu-Cl bond lengths and the La-Cl bond lengths.[54] Therefore, for the calculation of the NaCl-UCl$_3$-PuCl$_3$ system, the activities calculated in 2008 for La, U, and Cl interactions can be used as a first order approximation of the Pu containing system. It is assumed that U-La interaction coefficients would be the same as U-U, (and incidentally La-La), and La-Na interaction coefficients are the same as U-Na.

Initial neutronic investigations of the NaCl-PuCl$_3$-LaCl$_3$ system indicate that the core is susceptible to even slight changes in the density of the molten salt. Therefore initial efforts were made to optimize the ratio of NaCl to PuCl$_3$-LaCl$_3$ in the molten salt system.

A composition of NaCl-PuCl$_3$-LaCl$_3$ (69-27.2-3.8 mol%) was chosen for the modeled salt system. Note that this is the simplified system; for neutronic purposes this is NaCl-TRUCl$_3$-LnCl$_3$. The significance of this salt density study can be seen in the slopes of Figures 3.4 and 3.5. The effect of the addition of the lanthanides, though
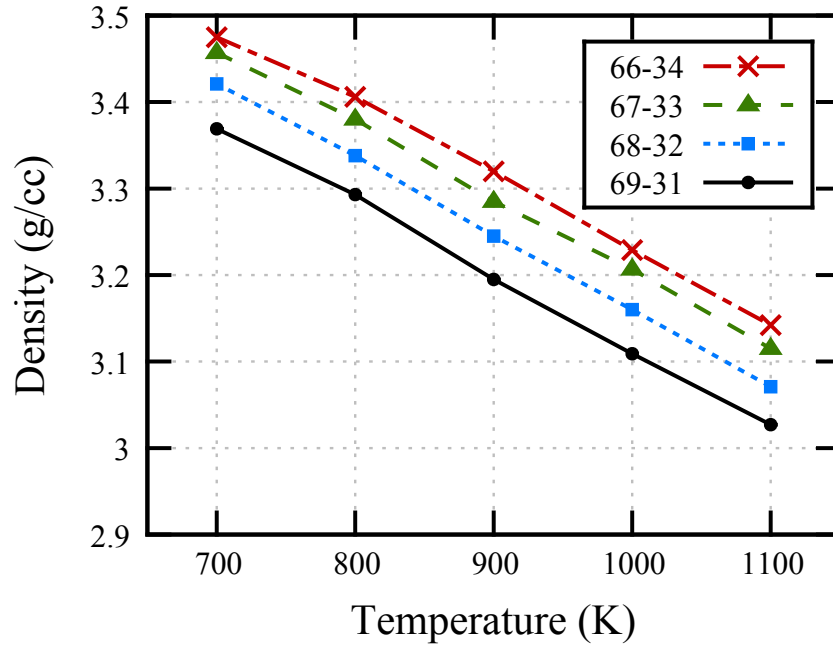
Figure 3.4: Density map (g/cc) of a series of NaCl-PuCl$_3$ compositions as calculated using MD.

they have similar electronic structure, is clear in the Figure 3.5. The core neutronics have been designed to accommodate the effects of an evolving density for the fuel salt on criticality and heat transfer.

Analysis of the MD simulation results for heat capacity, thermal conductivity, and viscosity was taken on by an undergraduate in the ADAM project, Mr. Austin Baty, who prepared an honors thesis on his work helping with the simulations and
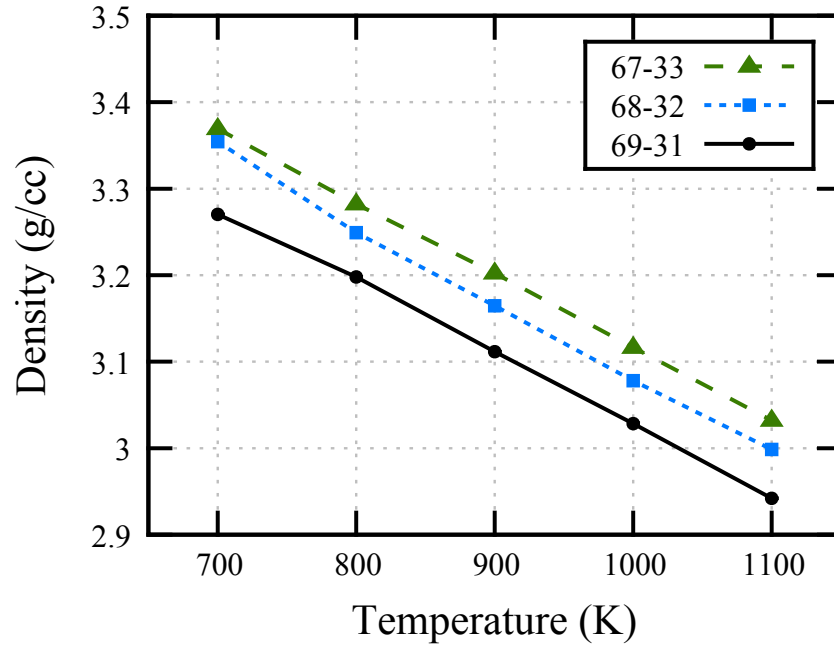
Figure 3.5: Density (g/cc) of a series of NaCl-PuCl$_3$-LaCl$_3$ compositions as calculated using MD.

writing the analysis codes. For more details on the analysis techniques for thermal conductivity and viscosity, reference Baty's thesis.[55]

3.2 Modeling Irradiation Damage in Materials

Irradiation damage experiments are costly in both time and money. There are several methods to simulate the interaction between particles and matter. While none can provide a defect-for-defect comparison, there are ways to optimize each. A recent paper published in 2013 made a comparison of a variety of techniques by simulating both heavy and light ion bombardment in iron and nickel. They report on a commonly used, open-source software SRIM (Stopping Range of Ions in Matter).[56]

SRIM employs a Monte Carlo simulation to predict the stopping range of ions in matter, the energy transfered to the metal lattice, and calculating the average number of displacements per incident ion. SRIM takes into account the energy loss to nuclear collisions, when the incident ion collides with a lattice atom nucleus, as well as the loss to electronic interactions. The majority of the energy transfered to the target is via electronic interactions, not kinetic collisions. An image of the ion/recoil distribution plotted in the x-z plane is displayed in Figure 3.6. As evident in Figure 3.6 the simulation treats the irradiation particles as a point source. The point source can then be mapped across an axis, however it will not account for additional collisions from overlapping straggle.

The comparative analysis published in 2013 compares four methods of estimating the dose delivered to an irradiated target. The control method the authors proposed is the NRT model, which was developed in the 1970's by scientists, Norgett, Robbinson, and Torrens (NRT).[26] The NRT model employs Equation (3.7) as the method to estimate the total number of vacancy-interstitial pairs (Frenkel pairs) produced by a primary knock on atom (PKA).[26]

$$\nu_{\mathrm{NRT}} = 0.8 T_{\mathrm{dam}} \frac{(E_{\mathrm{PKA}})}{2 E_{\mathrm{d}}} \tag{3.7}$$
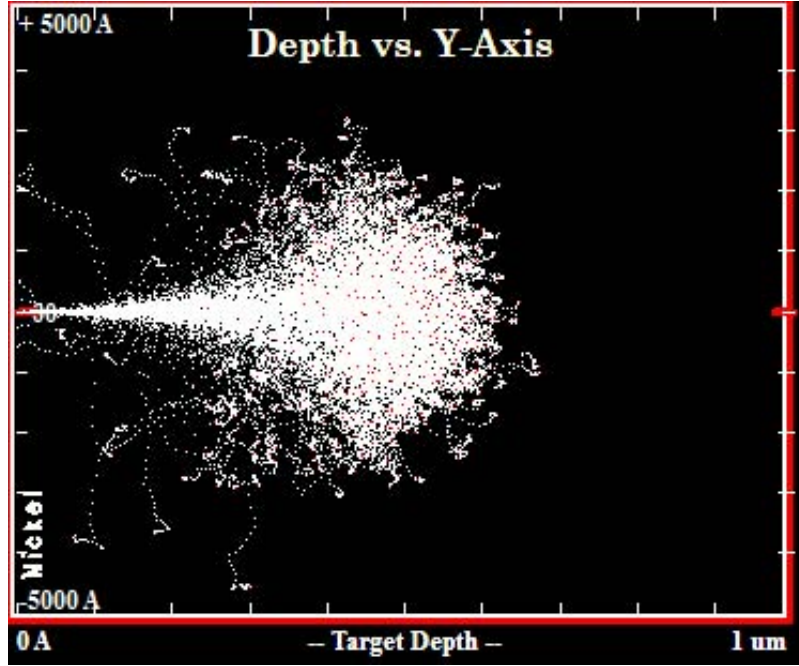
Figure 3.6: The ion/recoil distribution resulting from a Kinchin-Pease simulation run on SRIM-2008. The model input parameters were 100 keV incident H+ ions into 10,000 Å.

T_{dam} is the energy nuclear collision energy, dissipated on contact from the PKA.

In comparing varied operational modes in SRIM, with MD simulation, and the NRT method, a very distinct result reached by the Stoller et al. Within SRIM there are stark contrasts in the results when running two seemingly similar modes. The "Quick Damage Calculation" mode employs a Kinchin-Pease model for calculating vacancies. While the "Full Damage Cascades" would seem to be the more precise route, given its description, it was shown in Stoller's work to over estimate the damage by more than a factor of 2, when compared to both the NRT model and the Kinchin-Pease 'Quick Calculation'. Table 3.2 summarizes the results published in 2013.[57] For more information on the comparative analysis, see Reference [57].

Table 3.2: Comparative Results of DPA Calculation Methods, as reported in Stoller: Displacements obtained for 78.7 keV PKA (50 keV damage energy) in iron (2013)[57]

Model	Analysis Method	Displacements
NRT model	Eq. (3.7) with Tdam = 50 keV	500
SRIM-2008 Kinchin-Pease	Use output with modified NRT	540
SRIM-2008 Kinchin-Pease	Sum of v_i and v_T from vacancy.txt file	530
SRIM-2008 Full Cascade	Use output with modified NRT	572
SRIM-2008 Full Cascade	Sum of v_i and v_T from vacancy.txt file	1099
Molecular dynamics, 50 keV, 100 K, 9 simulations at 15 ps	n/a	168 ±4.04

Referencing the result above from the 2013 study, SRIM-2008 will be used to estimate the damage dose to the SCID sample during the simultaneous irradiation damage and corrosion.

When setting up a calculation in SRIM, the user must define the target material(s), specifying thickness and density. The incident ions can range from hydrogen to uranium with energies 10 keV to 10 MeV. When defining the target, if the incident ion is suspected to penetrate the sample thickness, I have learned that care must be taken to account for the trajectory of the incident ion once it has exited the sample. SRIM does not have a vacuum option for a material. Likewise, if no material is left at the boundary, the output vacancy time data varies broadly. For example, the SCID 1 sample is 90 μm thick. To calculate the dose at the salt interface there are three modeling approaches one can take. The first is the simplest: setting the target thickness in SRIM to 90 μm. Even in the simple approach there are two dose calculations that can be made depending on the analysis route preferred, an integration over the entire sample and a spot calculation at 90 μm for to assess the dose just at the interface. The second defines a second layer of material continuing after the nickel. The second layer in this case would be 'NaCl crystal,' a material found in the SRIM database, and then assigning the crystal the modeled density of NaCl-CeCl$_3$

will more accurately model the physical system; (see the Molecular Dynamics Section of this Section for modeling densities of salts). Lastly, vacuum can be simulated by choosing hydrogen as the second layer and defining it as a gas. The program will allow a user to change the density. Therefore you can lower the density of the gaseous hydrogen up to five orders of magnitude. The idea of simulating vacuum is to minimize the number of collisions which are calculated in the simulation, therefore attaining a better understanding of the ions' trajectories after penetrating the sample. Table 3.3 reports the total vacancies reported by SRIM-2008 with 99,999 5.8 MeV H+ ions using all three boundary methods.

Table 3.3: Interaction Potential Parameters for ADAM Fuel Salt

Modeled System	Total Vacancies/ Angstrom-ion at 90 um	Integrated Vacancies/ ion over first 90 um	DPA/hr at Interface (3 μA beam 2 mm^2 beam spot)
Nickel with SRIM Boundary	0.000139	28.2	0.51
Nickel with NaCl Layer	0.000126	28.0	0.46
Nickel with Simulated Vacuum	0.000125	27.8	0.46
150 um Nickel	0.000113	28.3	0.42

For a quick one hour beam exposure, these discrepancies may be well within the error of the experiment; for longer duration 70-100 hour irradiations these discrepancies can be troublesome. When modeling the system in SRIM, I do not recommend having the built-in boundary in the sample region of interest. I have had no problem adding up to four inches of simulated vacuum to a system, to map the trajectories of penetrating ions to detector.

4. EXPERIMENTAL TECHNIQUES

4.1 Salt Synthesis

Dry, pure salt compounds are both expensive to purchase and challenging to synthesize. These materials are inherently hydroscopic. Several water molecules can be accommodated within the crystal structure of the heavy metal chlorides. For example, $CeCl_3$ can accommodate up to 8 water molecules. There are several routes proposed to produce pure heavy metal chlorides. Three have been investigated in this dissertation work: pyrochemical, dehydration, and inorganic synthesis.

4.1.1 Pyrochemical Heavy Metal Chloride Synthesis

Pyrochemistry arguably offers the most applicable heavy metal chloride salt synthesis route. The ADAM core operates with a $NaCl$-$TRUCl_3$ fuel salt. Most pyrochemistry takes place in an inert environment and readily permits the oxidation of a metal to its chloride in a host salt. Oxide fuel that has been used and discarded from a conventional reaction can be made into a chloride fuel in a NaCl host salt. In collaboration with scientists at Idaho National Laboratory, a conceptual process to synthesize the ADAM fuel was devised during this dissertation work. The process readily produces the fuel salt for the ADAM core. I will briefly describe it here. The process, as it has matured to date, is displayed in Figure 4.1

Step 1: Decladding and Oxide Fuel Recovery from UNF Fuel Pins

The first step separates the UNF (Used Nuclear Fuel) from the cladding. Fuel extraction is achieved by chopping, decladding, and crushing the UNF prior to the pyroprocess or via voloxidation. Voloxidation of the chopped fuel pins is a head-end step involving high temperature oxidation of the UNF. It has been investigated in recent years as a way to both to separate the UNF from the cladding hulls and to
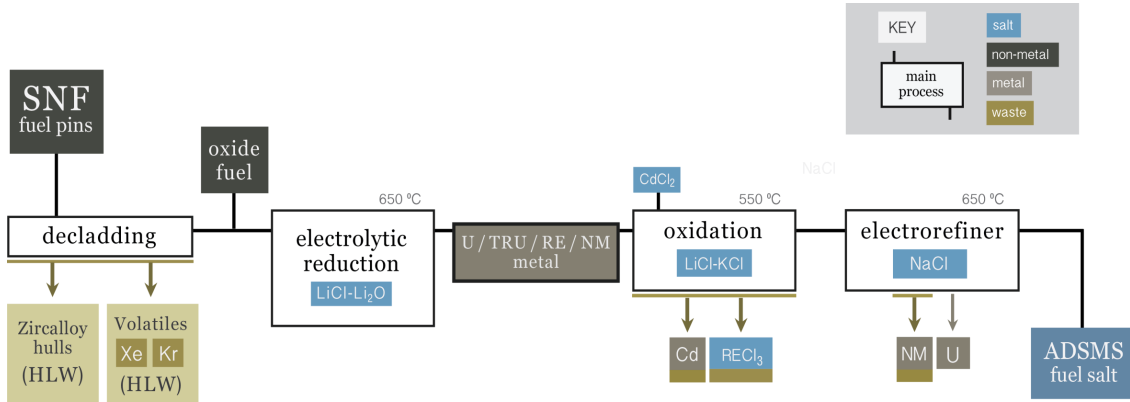
Figure 4.1: Starting at the left of the diagram and then moving to the right describes the steps necessary to create the ADAM fuel salt.

release and trap the volatile fission products.[58,59] Additionally, voloxidation reduces the particle size of the material continuing to electrolytic reduction, increasing the efficiency of that reaction.

Step 2: Electrolytic Reduction

The oxide powder collected during decladding and voloxidation is loaded into a cathode basket. The basket is then lowered into a LiCl-1wt% Li_2O electrolyte salt at 650 °C. Bench scale tests at INL indicate that >98% actinide reduction is expected in the process along with the reduction of 65% of the rare earth content. A number of fission products are expected to dissolve into the host salt during the reduction process (Cs, Ba, I, and Sr).[60]

Step 3: Rare Earth Oxidation

Accumulation of lanthanides (the bulk of the RE fission products) hinders fission in the ADAM core; though this effect is not as severe in the ADAM system as compared to a conventional fuel rod system. Therefore in our preprocessing proce-

dure, the objective will be to remove a majority (70%) of RE fission products, while minimizing the amount of Pu oxidized and sent to waste.

To achieve selective RE separation, an oxidation step is proposed. During the RE oxidation phase, the U/TRU/RE/NM metal contained in the cathode basket from electrolytic reduction is submerged in molten LiCl-KCl at 450 °C. $CdCl_2$ is added to the salt to oxidize the rare earth fission products to metal-chlorides. Thermodynamically, the RE's form more stable chlorides than do the actinides and noble metals. This allows the RE elements to be separated from the actinides in the used fuel by selectively partitioning them into the salt phase. The calculated standard free energy change of reaction for cadmium oxidation with various actinides and lanthanides is shown in Figure 4.2. It should be noted that for small scale experiments, such as the phase diagram study which will be described later, only the oxidation step is necessary, since metallic, high purity Ce and U can be readily purchased. That said, separating the resulting $CeCl_3$ or UCl_3 is non-trivial.

Step 4: Electrorefining: Actinide Oxidation and Uranium Reduction

Finally, the basket contains U/TRU/NM, Dy, Eu, and 20% of the RE as reduced metal. For the recovery of TRU as chlorides, oxidation is necessary. A NaCl-based host salt should be used for this. Pure NaCl requires high (<850 °C) operating temperatures; a NaCl-UCl_3 host salt could prove more practical as that system forms a eutectic and will lower the operating temperature. The objective of this step is to replace UCl_3 with transuranic chlorides via reaction with the U/TRU/NM. The salt will become progressively more suitable for use in the reactor core. This should occur via spontaneous reaction between UCl_3 and the TRU/RE metals. Periodically, the metallic uranium that forms in the electrorefiner can be electrochemically collected on a cathode and removed. At the end of this step, the NM content remains unreacted in the original basket, and will then go to a waste repository after being melted
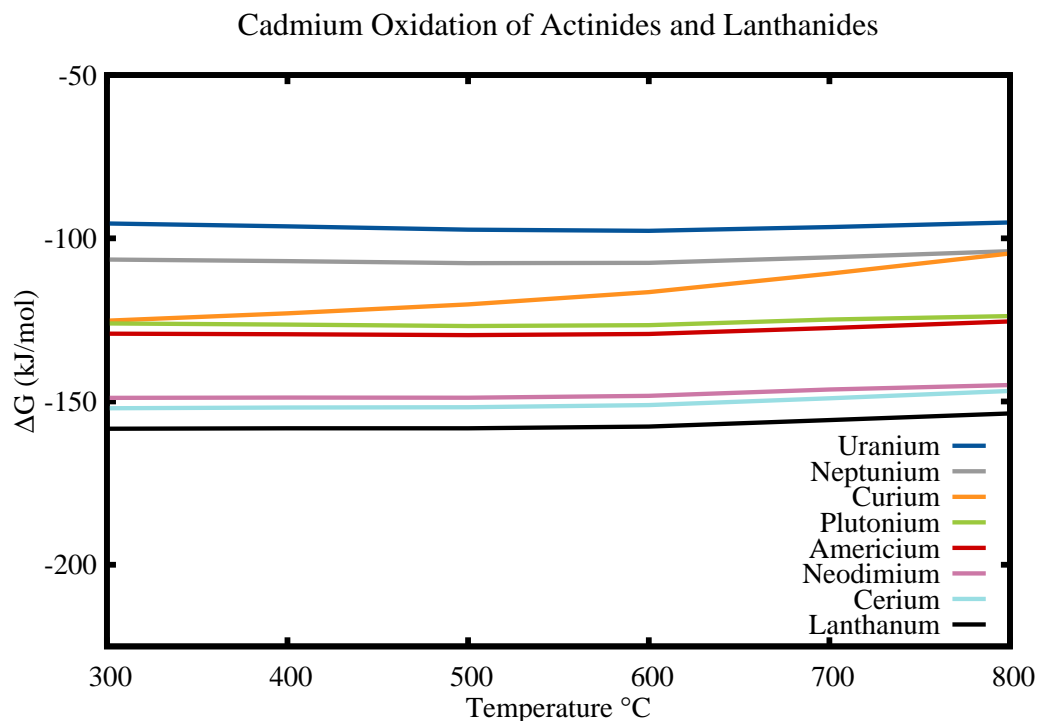
Figure 4.2: Gibbs Energy of Reaction of Reaction for the Cadmium Oxidation Process. Reaction energies calculated using HSC Chemistry 7 software.

into a metal waste form. Once the TRU oxidation has been completed for a given batch of salt, it may be necessary to separate excess NaCl. NaCl segregation can be performed in theory by a zone freeze refining or cold finger operation. The objective is to bring the final composition to that of an ADAM core: NaCl-TRUCl$_3$-LaCl$_3$ (0.68-0.28-0.04 molar fraction).

During the bromide salt investigation, oxidation of La into LaBr$_3$. UCl$_3$, PuCl$_3$, and other actinides can be made via the process explained above. Portions of that process have been well documented during the pyroprocessing efforts at both Argonne National Laboratory and Idaho National Laboratory. When the ADAM project was

considering bromide fuel salts as an alternative to the more well known chlorides, and investigation into the synthesis of these actinide bromide salts was undertaken. The oxidation of La into $LaBr_3$ serves as a surrogate experiment for UBr_3 synthesis. As stated above, $CdCl_2$ is the most commonly known oxidizing agent to oxidize actinide chlorides. A plot of the Gibbs Free Energy of Reaction for the actinides to be oxidized to chlorides using the reaction in Equation (4.1) is plotted in Figure 4.2.

$$3CdCl_2 + 2U \rightarrow UCl_3 + Cd \tag{4.1}$$

$CdBr_2$ will work well for the same oxidation process, however Cd is a RCRA (Resource Conservation and Recovery Act) regulated metal. Since the experiments at CAES are planned to be performed with uranium, the resulting waste from the experiment would qualify as a 'mixed' waste containing both radioactive material and a RCRA metal. Therefore, for the initial oxidation studies, other compounds which could simulate the behavior of $CdBr_2$ were investigated. A plot of the Gibbs Energies of Reaction for $CdBr_2$, $FeBr_3$, and $BiBr_3$ for use as U oxidizers is plotted in Figure 4.3.

Primarily due to cost and material availability, $BiBr_3$ is chosen as a good alternative for $CdBr_2$. $BiBr_3$ also has a low, 219 °C melting point. The only concern posed by the much more negative reaction energy is heat generation during the experiment.

The experiment is performed at the Center for Advanced Energy studies in an argon, positive pressure glove box. A crucible containing 80 g of LiBr-KBr host salt is held at 350 °C. The goal is to make a 9:1 host salt to $LaBr_3$ weight ratio. Therefore, the reactants must yield 8.89 g of $LaBr_3$. In order to do this, a total of 13.79 g of reactants are introduced through the experiment. To start, 2.07 g of La metal and 10.534 g of $BiBr_3$ are loaded into separate stainless steel baskets. The $BiBr_3$ is

47
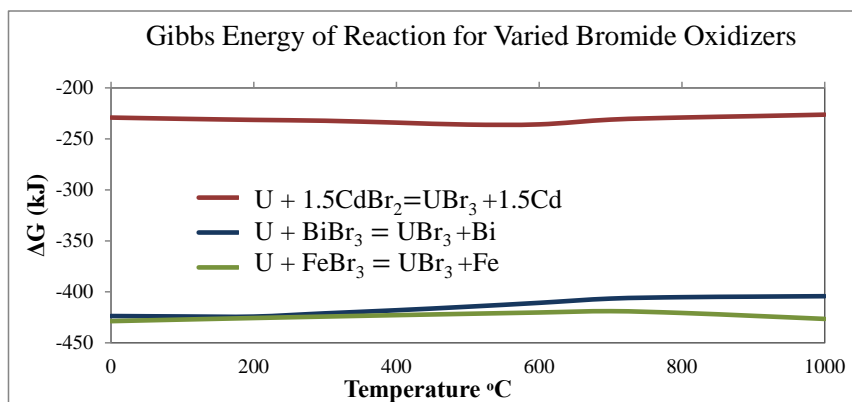
Figure 4.3: Plotted are the Gibbs Energies of Reaction as a functions of temperature for the chemical processes listed. The more negative the reaction energy, the more preferred the reaction products. Therefore the use of $BiBr_3$ or $FeBr_3$ as oxidizers will work well to convert U to UBr_3. The reactions should go to completion quickly.

dissolved into the host salt. Then the basket of La is introduced to the salt. Almost immediately, material is plated onto the stainless Steel basket. It seems that $BiBr_3$ is coming out of solution, as it is possible that as $LaBr_3$ is produced in the reaction the solubility of $BiBr_3$ is reduced. It could also be Bi metal plating onto the basket, as it poses as a 'cold finger' during the experiment. The melting point of Bi metal is 271 °C, and while the experiment is held at 350 °C, the stainless steel rod could be much lower in temperature until the entire system has had time to equilibrate.

An image of the stainless steel basket, taken mid-experiment, is displayed in Figure 4.4. After 20 minutes the system appears to have thermally equilibrated and the precipitate once seen on the stainless steel basket and rod has dissolved into the salt. The salt appears clear with a glass/metallic substance on the bottom. This is a good indication that the salt has not been saturated and that the reaction has gone to completion. The second piece of La metal is added as well as the remaining $BiBr_3$ to complete the reaction. The system is then allowed to equilibrate thermally. Unfortunately, after the remaining reactants are added, the salt does not clear again

Figure 4.4: The image here displays plating of with BiBr$_3$ or Bi metal during the LaBr$_3$ oxidation experiment.

and looks to be uniformly 'sludgy'. This indicates that the host salt is saturated and no more than 10 wt.% LaBr$_3$ can be dissolved into this host salt. An image taken after the completion of the experiment is displayed in Figure 4.5 It is possible that a different host salt could prove to have a higher solubility of LaBr$_3$. The salt from these experiments are to be analyzed via ICP-MS. Samples were taken using the same procedure as described in the 24 hour static corrosion section. Although the large wt percentage LaBr$_3$ dissolved into the salt could prove challenging as this technique is primarily geared for trace elemental analysis.

One additional challenge to pyrochemical salt synthesis is that it must occur in a host salt in order to remain liquid at reasonable temperatures. The host salt requirement poses no problem for the synthesis of the ADAM fuel salt; however, for small scale experiments when high purity chloride compounds are necessary, the

Figure 4.5: Shown here is the salt in the crucible following the LaBr$_3$ synthesis reaction. The sludgy appearance indicates that the salt saturated at some point during the reaction, and could not contain a full 9:1 host salt to LaBr$_3$ ratio.

host salt becomes a nuisance. Separation of CeCl$_3$ or UCl$_3$ is not trivial. Zone freezing has been proposed by a number of groups, however this process is only 80% efficient at best. For phase diagram investigations, salt purity is of the utmost importance. Therefore to acquire salt for small scale experiments the following routes are investigated experimentally.

4.1.2   Salt Dehydration

Hydrated salts are readily acquired commercially and inexpensive. Dimitrov (1996) proposes a drying method for CeCl$_3$-7·H$_2$O.[61] The method proposes a low temperature, vacuum drying over the course of 40 hours employing several holds/soaks at different temperatures: 50 °C (4h), 60 °C (4h), 70 °C (5 hr), 80 °C (7hr), and 140 °C (20hr) on a Schlenk line.[61] A Schlenk line is a processing apparatus used in syn-

thesis work, which allows for moderate atmosphere control, low vacuum capability, and high temperature baking of solutions. These lines are commonly used in organic and inorganic chemical processes. The first 4 of these steps were reported to remove 80% of the water. The vacuum level for this test was 0.05-0.01 Torr.[61] The Fuels Research Lab is capable of much higher vacuum levels, and therefore the time for the dehydration is expected to be less. To test the dehydration procedure, a small amount of $CeCl_3$-$7 \cdot H_2O$ is placed in a platinum crucible atop an Al_2O_3 stage in a Netzsch F1 STA-TGA (Simultaneous Thermal Analysis-Thermogravimetric Analysis). The STA allows a researcher to measure mass loss or gain over time during a reaction. A thermal profile is optimized over the course of three experiments, monitoring mass loss over time. Initially an identical thermal profile to Dimitrov (1996) was tested. The vacuum level achieved in the STA is reported at 0.001 Torr, an order of magnitude better than that of the previous work. The mass loss of the sample is measured to be 31.27%. Theoretically the sample should lose 33.85%. The data for 80 °C max dehydration experiment is plotted in Figure 4.6.

A second vacuum heat treatment was applied to the same sample without opening the furnace to air. The thermal profile ramped slowly to 80 °C, held for 30 minutes, and then ramped slowly (2 K/min) to 140 °C and held for 4 hours. The mass of the sample dropped constantly, well below the theoretical mass loss anticipated. It is suspected that Cl_2 gas was evolving from the sample. Upon removing the sample from the STA, it was massed on a bench top mass balance. The mass consistently increased as it was weighed three separate times. The rapid mass increase is a statement to the salt's extreme hydroscopic nature. Air transfers were decidedly avoided from this point on and the non-investigative salt synthesis heat treatments performed in the glove box furnace.
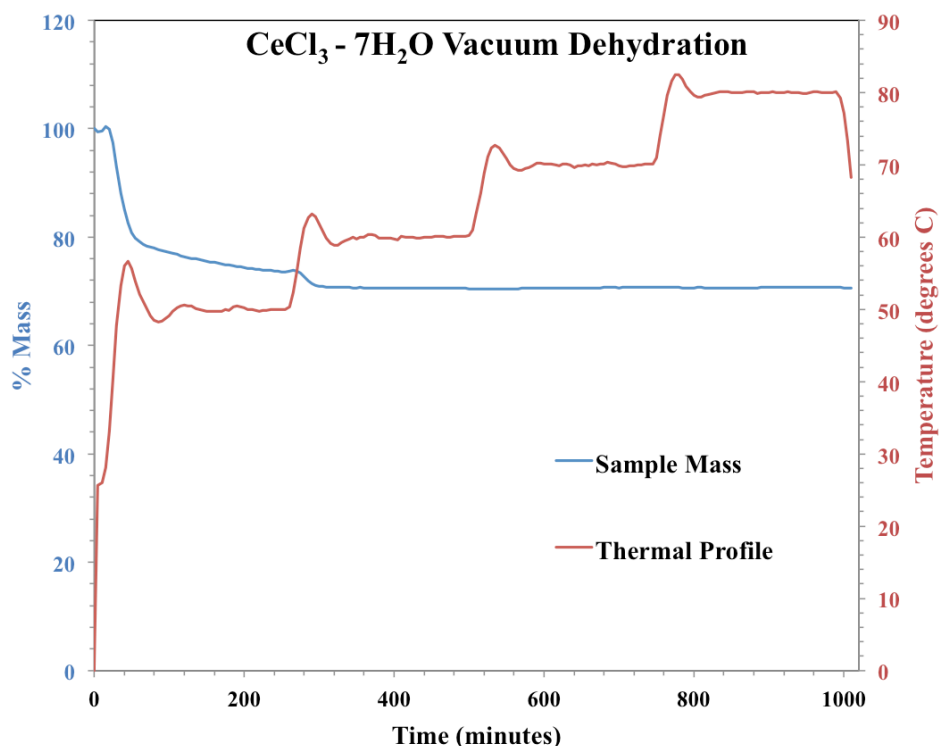
Figure 4.6: Plotted is the mass loss over time of $CeCl_3$. The blue trend is the percentage Mass of the sample and the red trend is the thermal profile, as cited in Dimitrov (1996).

The first experimental dehydration proves to be both too long in duration for practical applications and facilitates the material's breakdown beyond simple dehydration. Therefore, the thermal profile for the dehydration of $CeCl_3$-7·H_2O needs to be modified. Referring back to the data from the first dehydration run, reference Figure 4.6, the steepest mass loss occurred between 50-60 °C. A 7 hour, 55 °C, high vacuum dehydration experiment was run in the STA. The experimental data for each of these is plotted in Figure 4.7.

The 55 °C dehydration corresponded to a 29% mass loss as recorded by the STA. The immediate downward trend in the STA data generally indicates that mass was lost at room temperature while high vacuum was initially reached. The mass loss
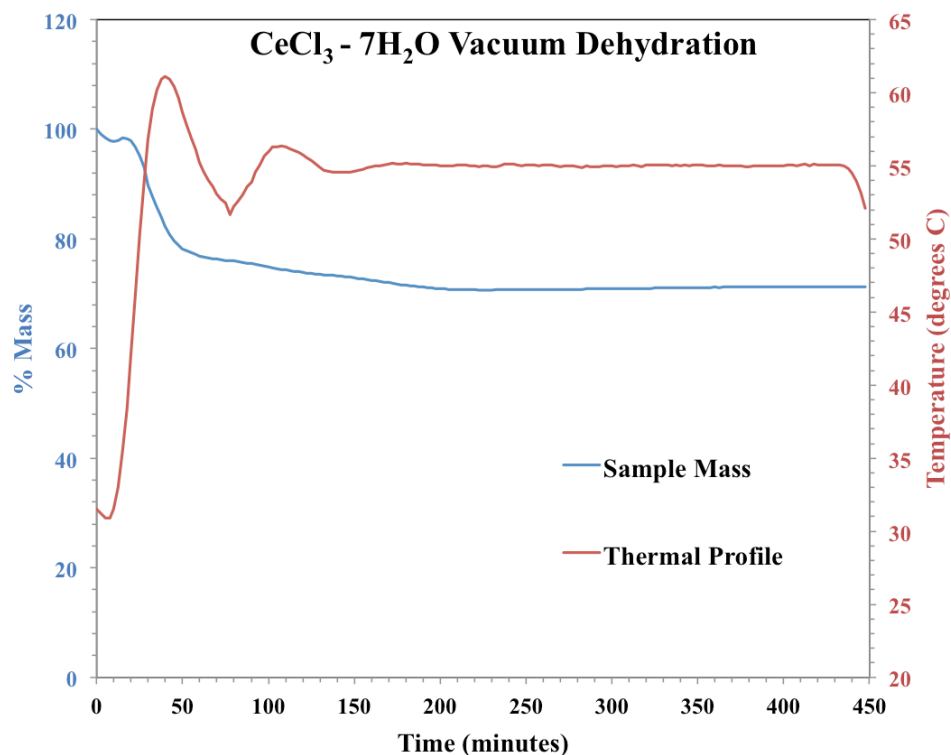
Figure 4.7: Plotted is the mass loss over time of CeCl$_3$. The blue trend is the percentage Mass of the sample and the red trend is the thermal profile. This thermal profile was modified after initial results indicated a lower temperature and shorter hold duration could achieve complete dehydration.

on the bench top balance is not a reliable measure of loss in the salt systems as the hydroscopic material readily absorbs water even after only seconds of exposure to air.

It is assumed at this point that the 55 °C, 7 hour heat treatment completely dehydrates the salt. The thermal profile is run on the hydrated CeCl$_3$ in the nitrogen glove box. The resulting salt is loaded into an environmentally sealed X-Ray Diffraction (XRD) chamber and sent for XRD analysis. The XRD data for both the hydrated CeCl$_3$ and the "dehydrated" sample are displayed in Figure 4.8.
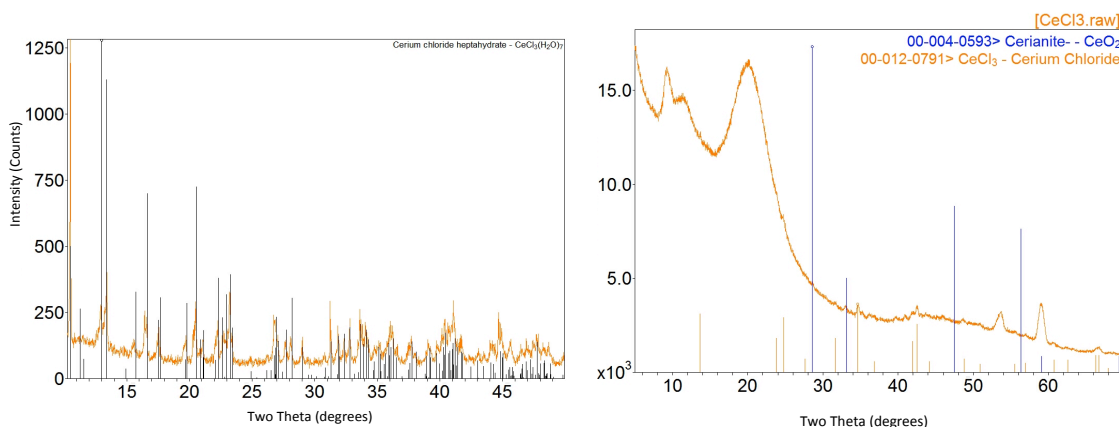
Figure 4.8: Left: $CeCl_3$-7·H_2O XRD diffraction patter. Right: The resulting powder from the dehydration experiment. The right diffraction pattern displays some $CeCl_3$, amorphous material, and some unwanted compounds.

There is one peak in particular at $2\theta=59$ ° which corresponds well to the (310) peak of $Ce(OH)_3$. During the drying process it is evident that an amorphous material containing oxides, hydroxides, and possibly hydrides of Ce were formed along with $CeCl_3$.

Our team at LANL is not the only group who experiences difficulties producing dry, pure $CeCl_3$. A U.S. based chemical supplier produces and sells "99.99% Ultra Dry $CeCl_3$ Anhydrous." Upon receipt of the material, a Au-plated stainless steel, sealable crucible was loaded into the DSC for a melt point test. The data indicates very separate liquidus and solidus temperatures with melting and solidifying far from the melt point of pure $CeCl_3$. Therefore, XRD data was obtained of the commercially supplied $CeCl_3$, to identify the impurity. The impurities were concluded to be hydrates of $CeCl_3$, per the XRD data displayed in Figure 4.9. A second order was placed, specifying a new lot of material. Similar results were observed. Finally, after performing the drying procedure used on the fully hydrated $CeCl_3$, on the commer-
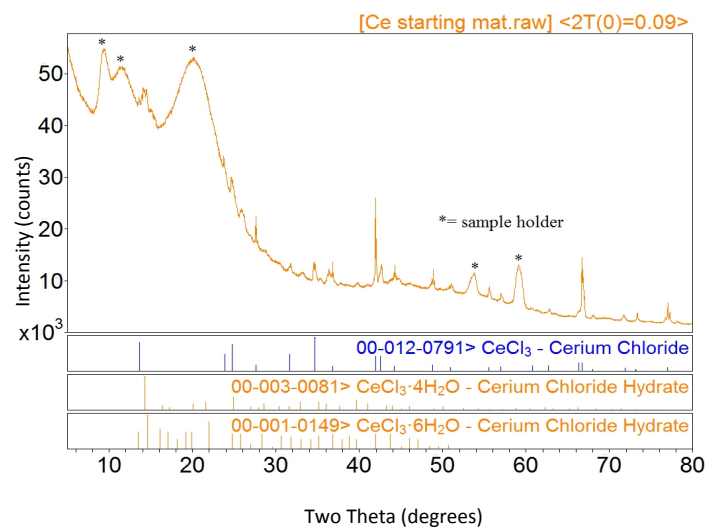
Figure 4.9: XRD Spectrum of commercially supplied 'dry' $CeCl_3$. The elevated background and broad peak in the lower angle portion of the scan are due to the environmental chamber polymer dome ('sample holder'). Some hydrate peaks are resolved which are a contaminate to this material and explain the dual peaked DSC data.

cially purchased $CeCl_3$ a dry material was successful. The resulting material is within $\pm$ 2 °C of the 817 °C melt point when correcting for the thermocouple calibration.

4.2 Melt Point Determination and Phase Diagram Investigation

The ADAM core contains actinides dissolved in a host salt, NaCl. The melt point of this composition is a critical part in determining the core's operating temperature, heat transfer, and criticality. For several of these systems, as described in Section 2 of this dissertation, the phase diagrams have either not been investigation experimentally or have not been investigated in recent history (since the 1970's). An experimental effort to investigate the NaCl-CeCl$_3$, NaCl-UCl$_3$, and NaCl-UCl$_3$-CeCl$_3$ salt systems is performed in the Fuels Research Laboratory at LANL. The use of CeCl$_3$ here is as a surrogate for PuCl$_3$. The experimental and analysis techniques are described here.

While the vapor pressures of these salts are low, the vapor deposits from the salt melts can be very corrosive to components exposed to air frequently, particularly metals. Thermal analysis equipment can be very sensitive to the oxidative corrosion over time, and therefore the salt samples must be encapsulated during thermal analysis experiments. The initial engineering hurdle for this study was identifying a practical encapsulation technique to allow the sample to be sealed in a dry atmosphere and transferred to the Differential Scanning Calorimeter. A group in Germany at the Institute for Transuranium Elements (ITU) employs two methods of encapsulation for their fluoride salt tests.[17] The first is a laser welded nickel crucible. This is not practical at the FRL, since there is not a laser welder readily available in the radiological lab. The second is cost prohibitive, as the manufacturing of each crucible is an intricate process. After discussing with scientists at INL, the high pressure, Au-plated stainless steel DSC crucibles available from Netzsch were identified as having the most potential.[62] The crucible is the gold cup with the hex bottom. A thin, gold plated copper seal is place atop the rim of this crucible, and a stainless steel lid is

56

threaded onto the top of this assembly; (male threads are located on the gold plated crucible). A torque wrench is used to make seal between the rim of the crucible and the gold plated copper disc. The assembly is displayed in Figure 4.10. Initial testing

Figure 4.10: 27 μL, Au-plated crucible used in the melt point investigations (left) and the sealing assembly for this type of crucible (right).

indicated that the crucible and lid could not be separated after exposure to temperatures in excess of 600°C. Lowering the torque applied during the sealing process and using an either reducing or inert external atmosphere in the DSC during the thermal cycling allows for these to be reused at temperatures exceeding 500 °C.

The second engineering challenge pertained to loading the crucibles with salt. Static became a hindrance in the nitrogen glove box. A deionizer was purchased to minimize this effect. The weighing set up in the glove box is depicted in Figure 4.11. The deionizer is black and located to the left of the work area. The deionizer allowed for precision weighing of salt directly into the crucible.

Initially, melt points of pure salt compounds were investigated to validate the experimental setup. NaCl and KCl were readily available. The DSC head holds a sample crucible and an empty reference crucible. The temperature/energy of each is monitored as the furnace takes both crucibles through the programmed thermal

Figure 4.11: Overhead view of the melt point sample preparation area in the N_2 glove box. In the center of the image is the balance, to attain 0.1 mg mass measurements accurate to $\pm$ 0.1 mg. The black box to the left is the deionizer used to minimize the static in the working area.

profile. The endothermic transition during the melting of a substance is detected as a difference in energy between the control/reference crucible and the sample crucible. Likewise, upon freezing, the exothermic transition is detected. The onset of these endothermic/exothermic curve on the energy curve indicates the liquidus/solidus temperature of the material. The DSC data for the first KCl melt point validation experiment is in Figure 4.12.

The melt point is indicated by the onset of the endothermic peak. The onset initially was 5 °C lower than the reported value for this number. Performing a calibration of the sample thermocouple provides a correction file for the thermal profile, which brings the onset to within $\pm$ 2 °C of the reported melt temperature. With confidence in our ability to seal the salt in the stainless steel crucibles and detect the melt point of the salt, NaCl was tested in the same way.

Mixing of these salts is a primary concern. Typically, an ingot of salt for a composition is prepared and salt from that homogenized mixture is segmented for DSC analysis. A good deal of waste is generated in this process as 100-200 mg of salt
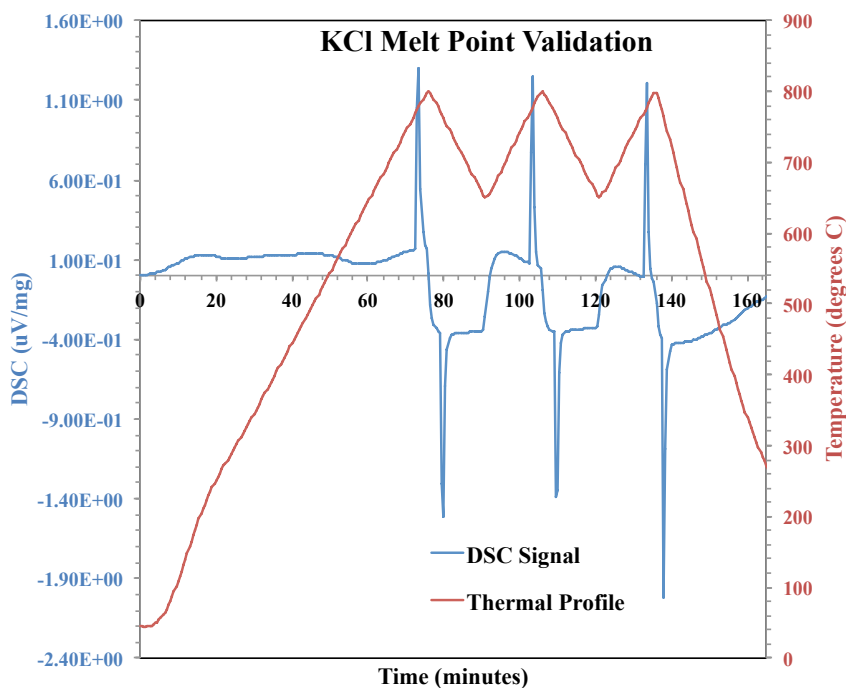
Figure 4.12: KCl DSC signal obtained from the first salt melt in the Au-plated crucibles. The blue trend is the μV/mg calorimetry signal and the red curve is the thermal profile as detected by the sample thermocouple.

is a reasonable amount to precisely weigh out and mix, however the DSC crucibles only hold 20-30 mg of material. The other concern is homogenization of the salts, without a long duration melt. To test the feasibility of avoiding a homogenizing milling or melting processes, NaCl-KCl eutectic was tested.

Without mixing of the compounds, the eutectic is measured withing ± 2 °C of the known value. The result allows us to conclude that a homogenizing step is unnecessary and experiments were carried forth to test the NaCl-CeCl$_3$ and NaCl-UCl$_3$ binary systems.

When analyzing the DSC signal for an off-eutectic composition, the Netzsch Proteus software will reliably find the onset of the eutectic melt (the solidus point). The onset is the intersection of the interpolated baseline signal and the tangent of the
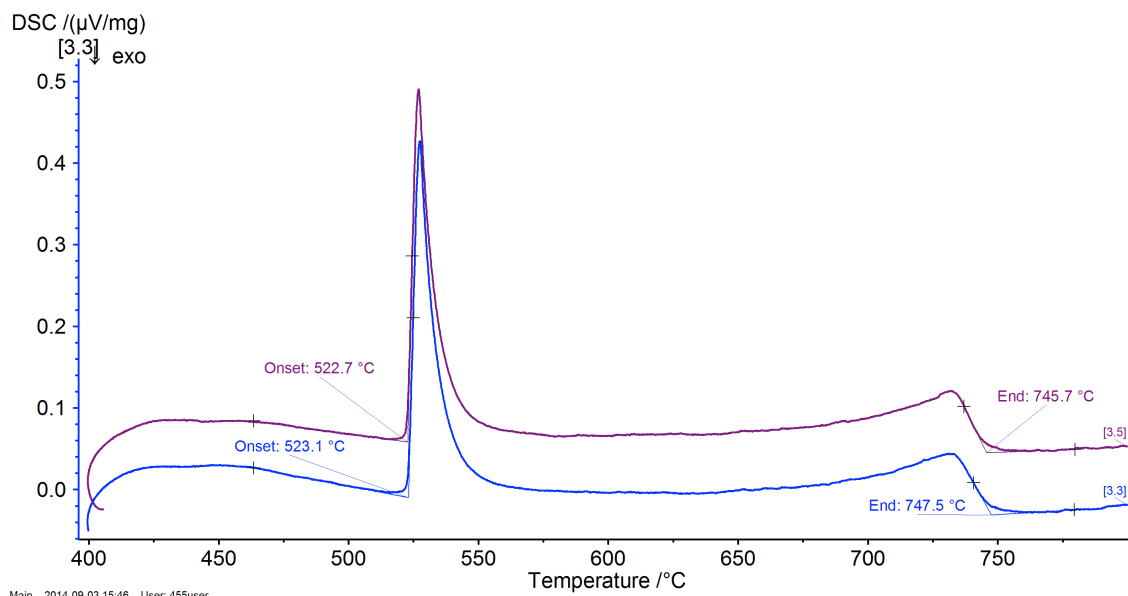
Figure 4.13: NaCl-UCl$_3$ (88-12 mol%) heating curves as functions of temperature. The upper signal if off-set vertically. The energetics are nearly identical. Indicated on the DSC signal are the solidus (onset) and liquidus (end) transitions. For each of these transitions, Netzsch Proteus Analysis software calculates intersection of the increasing and decreasing tangents with the baseline signal.

peak's positive, endothermic slope. The liquidus point can also be identified as the "end point" or rather the end of the phase transformation. To identify this point the software finds the intersection of the down-coming slope at the end of the elevated energy regime and the interpolated baseline. A prime example of a heating curve of a binary system is displayed in Figure 4.13 with both the solidus and liquidus points identified. Results for the NaCl-UCl$_3$, NaCl-CeCl$_3$, and NaCl-UCl$_3$-CeCl$_3$ phase diagrams are presented in Section 5 of this dissertation.

4.3 Static Corrosion Testing

The corrosivity of these salt systems is driven by several factors, which are discussed in length in Section 1 of this dissertation. To minimize the number of variables in a given experiment, the aim of the corrosion testing reported here is to look at

60

solely the corrosion of a molten salt in contact with a metal. Flowing salt induces erosion and material transfer. Salt flow is not incorporated here, as I want to investigate possible material transfer that occurs without the aid of fluid transport. Also, impurities are minimized to limit impurity-driven corrosion. Described here are the experimental techniques used in a series of 24 hour corrosion experiments and a 100 hour corrosion experiment.

4.3.1   Chlorides vs Bromides

Early in the ADAM host salt and candidate vessel material investigation, a collaboration was formed with Idaho National Laboratory to investigate the use of bromide based fuel salt systems. The choice of molten salt system for the core is an important element to optimize its performance, as is discussed in length in Section 2 of this dissertation. While the neutronic, thermodynamic, and corrosive properties of alkali and alkaline earth molten fluoride and chloride salts are relatively well documented, no studies on the bromide based salts have been performed to date. Bromide salts offer three advantages over both fluoride and chloride salts. First, the heavier salt system can sustain fast neutronics (reduce the energy a neutron loses per scattering). Second, bromides offer lower eutectic melting points (e.g. LiCl-KCl-CsCl at 335 °C vs. LiBr-KBr-CsBr at 228 °C). Third, bromide salts can potentially offer a better basis for separating lanthanides from actinides - a key provision in the ADAM design.

Over the summer of 2011, an experimental plan to study the behavior of heavy metal bromide chlorides was devised. In this experimental approach, I had the opportunity to form $LaBr_3$, a surrogate for UBr_3. The $LaBr_3$ experiment is discussed in 4.1. The bromide fuel salt investigation was quickly discontinued due to a lack of experimental data on these salt systems, observations made during this body of work, and a limited amount of activity coefficients for the actinide-bromide interaction to

use in MD modeling. That said, a corrosion study of candidate vessel materials was completed comparing the effects of both chloride and bromide salts. That corrosion investigation is discussed here.

The primary objectives of the static, chloride vs. bromide corrosion study are to expose a broad variety of metals to both salts separately at high temperature (700 °C) for 24 hours. The samples should be designed in such a way to allow for electron microscopy analysis and tension testing. The initial static, (not flowing), tests of eleven different metals are performed in LiCl-KCl eutectic (58-32) and LiBr-KBr (60-40) eutectic. The experiments were performed at 700 °C in an argon glove box; the metal coupon samples were exposed for 24 hours. The materials tested were the following metals and metal alloys:

- Niobium
- ECAE Niobium (Equal Channel Angular Extrusion)
- Tantalum
- Nickel
- Zircaloy (two types)
- 316 Stainless Steel
- Tungsten
- Hastelloy-N
- HT-9 Steel
- T91 Steel

Samples of Nb, ECAE Nb, Ta and W were obtained from the Mechanical Engineering department at Texas A&M, Prof. Karl T. Hartwig's laboratory. These samples are assumed to be 99.5% pure. For the alloys which were used in this experiment, the commonly reported compositions (ASM Handbook) are reported in Table 4.1. Great care is taken to control the atmosphere of the corrosion experiments.

Table 4.1: Composition of Metal Alloys

Wt % Composition	Ni	Cr	Zr	Mo	Sn	C	Mn	Fe	Si	P	S	Co	W	Cu	B	V
Ni	99.5	–	–	–	–	0.08	0.18	0.2	–	–	–	–	–	–	–	–
Hastelloy-N	Bal	7.0	–	16.5	–	0.06	0.4	3.0	–		0.25	0.25	0.2	0.1	0.01	–
Zr 2	.03-.08	0.05-0.15	Bal	–	1.2-1.7	–	–	0.07-0.2	–	–	–	–	–	–	–	–
Zr 4	0.007	0.05-0.15	Bal	–	1.2-1.7	–	–	0.07-0.2	–	–	–	–	–	–	–	–
316 SS	10-14	16-18	–	2-3	–	0.08	2.0	Bal	1.0	0.045	0.03	–	–	–	–	–
HT9	–	12.0	–	1.0	–	–	–	Bal	–	–	–	–	–	–	–	0.3
T91	–	8.3	–	0.75	–	0.11	–	Bal	–	–	–	–	–	–	–	0.18

The samples are cut via wire EDM (electric discharge machining) to ensure precise dimensions for tension testing. Each sample is etched to remove bronze residue from the EDM wire. The etching/pickling solutions for each type of material are found in the ASM Handbook. The samples are baked at 150 °C to remove any residual water and residue from the etching process. Samples are then introduced to the glove box environment and corroded. The glove-box is a positive pressure, Braun glove box displayed in Figure 4.14. The atmosphere in the glove box is held to <0.1 ppm O_2 and H_2O. The salt used was 99.99% pure LiCl-KCl eutectic obtained from Fischer Scientific. The salt is held at 700 °C $\pm$ 2 °C.

Figure 4.14: Pictured is the 'Vandals' glove box at the Center for Advanced Energy Studies. All 24 hour corrosion tests are performed in this positive pressure glove box. The box is kept at a slight positive pressure to protect the hydroscopic, air sensitive salts, in the event that there is a glove tear or other atmosphere breech. A chiller system is fixed to the box to keep the temperature of the box itself and the seals in particular below 50 °C.

The chemically cleaned, non-polished surface is assumed to most accurately emulate a vessel material. However, the lack of polishing will prove to prevent quanti-

tative analysis of grain boundary penetration made by the salt. To avoid excessive galvanic corrosion, Al_2O_3 crucibles are used, and while two samples are introduced at a time, they were the same material. The Al_2O_3 crucible is placed in a jeweler's furnace with a graphite sleeve placed between the furnace coils and the crucible. The set up is designed to minimize electrical conductivity to the electrolytic salt, minimizing external corrosion drivers. The furnace setup is displayed in Figure 4.15. During the ICP-MS analysis, Al was found in the salt, indicating that the crucibles react with the salt.

Figure 4.15: Pictured here is metal melt furnace, also known as a jeweler's furnace. The top loading, open design allows the experiment to be observed using the mirror mounted above the furnace. The compact and isolated nature of these furnaces are ideal for not only open corrosion experiments but also for other pyroprocessing experiments such as ion-exchange and reduction/oxidation experiments.

4.3.2   Thickness Changes after Chloride Salt Exposure

The thicknesses of the samples are measured in three places along the straight of the dog-bone before and after each experiment. For the chloride experiments, the average change in thickness is displayed in Figure 4.16. The average thickness
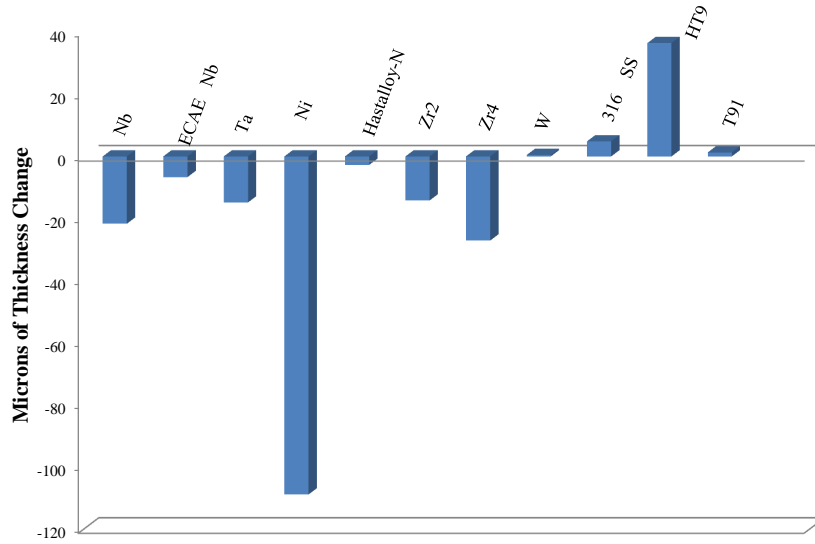
Figure 4.16: Plotted is the average thickness change of each alloy exposed to the 700 °C LiCl-KCl salt for 24 hours. The Ni thickness reduction is thought to be artificially high due to non-uniformity in the initial sample. It should be noted that the growth in the steel samples is indicative of oxidative growth on the surface.

change does not provide a full explanation for the corrosion behavior. For example the amount of thickness gained in the steel experiments is measurable and significant. It appears an oxide or oxy-chloride layer formed. Oxidative growth is apparent in both the thickness increase and the color change of the sample noted during the experiment. Plating is observed in the nickel and tungsten experiments, consistent with galvanic process driven by a difference in thickness of the initial samples. The

nickel sample is particularly interesting. A thin section on the sample prior to corrosion remains nearly the same thickness after corrosion, while the rest of the sample and the other sample shed material until they reached approximately that thickness. Additionally, 74 μm of material was plated at the top of the dog bone, closest to the salt surface. A diagram describing the samples before and after is displayed in Figure 4.17.
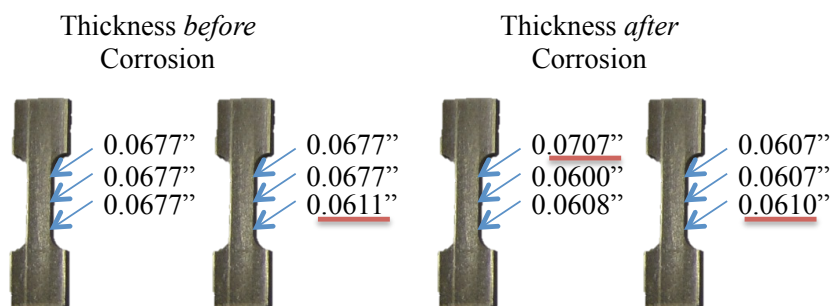
Figure 4.17: As depicted here, the thickness of the straight of each 'dog bone' sample is measured in 3 places before and after the corrosion experiment. A low spot the Ni sample is thought to be the driving mechanism for the large thickness reduction plotted in Figure 4.16.

Bubbling on the surface of the nickel samples was evident during the early hours of the experiment. Hastelloy-N is expected to behave similarly to pure Ni. It displays the least amount of thickness reduction. The Hastelloy-N samples are more uniform in thickness. Also, competing oxidation could account for lower levels of material loss.

The Zircaloy alloys, while measuring little thickness change, displayed the most radical visual changes. During the experiments for both the Zircaloy 2 and 4 alloys, the LiCl-KCl host salt became blue after only 2 hours. Each sample also exhibits
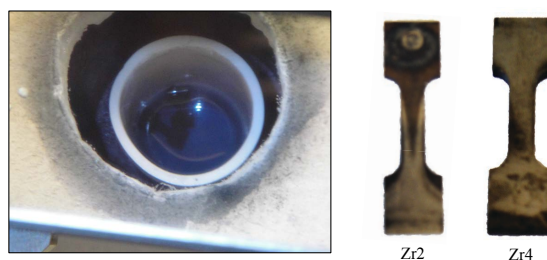
Figure 4.18: The Zircaloy 2 and 4 samples display the most visible changes during the 24 hour chloride exposure. The picture to the left shows the 'blue' salt which occurred between 4 and 12 hours into the experiments and cleared by the end of the experiment.

a 'swirled' black and gray coloration after the corrosion test. Figure 4.18 shows the blue salt and both samples after corrosion. In each experiment that exhibited a color change in the salt, by 12 hours into the experiment the salt returned to a clear state. The salt becoming clear indicates that either the corrosion product responsible for the change volatilizes or deposits on the bottom. From other visual observations and ICP-MS data, it can be concluded that it is likely a combination of the two, but a saturation limit is certainly reached. What is also possible in the Zircaloy experiments is the formation of $ZrCl_3$ which is known to have a blue-black hue. The melt point of this compound is 627 °C. If the $ZrCl_3$ is further oxidized $ZrCl_4$, the resulting compound is white in color and would most likely volatilize, due to a low, <400 °C boiling point. However, this reaction would have to be impurity driven, as the formation of either of these compounds in LiCl-KCl is energetically unfavorable. Other visual observations include the following: Tungsten shows almost no change at all, visually. Both niobium samples darkened during the experiment. In all experiments a dark deposit is found on the bottom of the dried salt after exposure to the metal samples.

68

4.3.3   Thickness Changes after Bromide Salt Exposure

For the bromide salt experiments, a completely different behavior is observed across the board with respect to the thickness change. It should be noted that after the observations made in the chloride experiments, samples with more uniform thicknesses are used in the bromide corrosion experiment. The thickness change is plotted in Figure 4.19. In almost every material from the refractories to the steel alloys, thickness increased by measurable amounts. The growth indicates a surface oxidative reaction, either picking up residual oxygen or the formation of a bromide layer which is not bromide salt soluble. It is important to restate that the O_2 level in the glove box was measured to be less than 0.1 ppm throughout all of these experiments. It is unlikely that such appreciable growth could be solely attributed to oxide formation. It should be noted that such a layer does not appear to form in the nickel alloys.
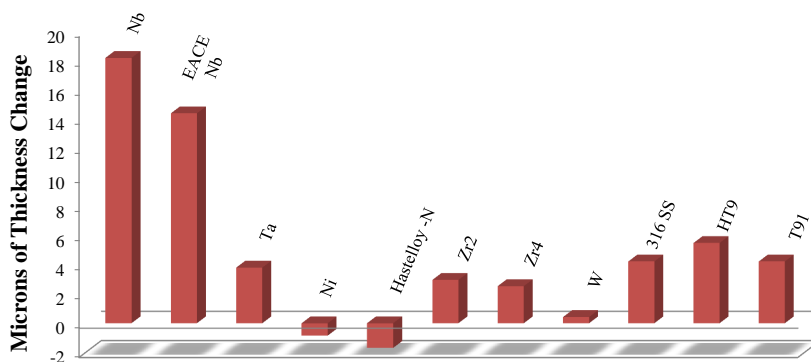
Figure 4.19: Plotted is the thickness change of each alloy exposed to the 700 °C LiBr-KBr salt for 24 hours. Nearly all samples display signs of surface oxidative growth. The only exceptions, which therefore lost some thickness, were Ni and Hastelloy-N.

69

The Zircaloy experiments exhibited the same color change, however it happened immediately upon introducing the sample to the salt. However, in the Zr_2 case this blue shade is much lighter. Many of the samples came out of the salt white on the surface, although the refractories showed darkening, resulting in almost black surfaces after exposure. The darkened surfaces further exemplifies the surface oxidative reaction indicated in the thickness change. The same is true for the steels exposed to the bromide salt.

Perhaps the most telling visual observation made during the bromide experiments was the constant vapor formation coming from the top of the furnace. While the vapor pressure of the salt is know to be a bit higher than that of the chlorides, the constant formation of vapor during these experiments makes them nonideal candidates for fuel host salts.

4.3.4 ICP-MS Experimental Method

In addition to sample thickness measurements and visual observations of the samples, Inductively Coupled Plasma-Mass Spectrometry is used to analyze the trace amount of metal corrosion products deposited into the salt throughout the experiments. Samples are taken at 2 hour intervals for the first 6 hours and in 6 hour intervals for the remaining 18 hours of the experiments. A piece of stainless steel foil formed into a cup is used to sample the salt from the experiments. The Al_2O_3 crucible holds approximately 30 g of salt in each experiment and the ICP-MS samples weighed 0.31 g. A picture of a salt sample method is displayed in Figure 4.20. During sampling the cup is lowered to the bottom of the salt crucible in an attempt to acquire a salt sample that is characteristic of the entire salt system, which is likely inhomogeneous. At the end of each experiment, the salt samples collected for ICP-MS analysis are extracted from the stainless steel cups. The salt in each

Figure 4.20: Pictured is the salt sample apparatus used in both chloride and bromide 24 hour corrosion experiments. A stainless steel foil cup is formed and then fixed to the alligator clip. The set up allows for safe, clean acquisition of salt samples during the 24 hour experiments.

sample is homogenized using a mortar and pestle, and a small amount is digested into a H_2O-HNO_3 matrix and transported to the ICP-MS on the University of Idaho campus. For each sample, standard concentrations of the elements of interest are digested into the same H_2O-HNO_3 matrix. During the refractory metal analysis, a standard containing trace amounts of Nb, Zr, Ta, W, and Sn. Concentrations of 0, 1, 10, 50, 100, 200, 500, 1000, 3000, 5000, and 10,000 ng/L are made. Then the instrument is calibrated accordingly. This process was performed for the steels and nickel alloys. A characteristic calibration result can be seen in Table 4.2.

ICP-MS is sensitive to interference signals. The quadrupole, tubing, etc can shed some material during the analysis, resulting in artificially high readings. One can compensate for these interferences, by telling the instrument when there should be no Fe, for example, by setting its calibrated signal to zero. Unfortunately that leads to

Table 4.2: Calibration Standard Results for Refractory Metals

Concentration (ng/L)	Zirconium (ng/L)	Niobium (ng/L)	Tin (ng/L)	Tantalum (ng/L)	Tungsten (ng/L)
0	0	0	0	0	0
1	0	0	0	0	0
10	3.25	4.381	2.3	5.625	1.727
50	40.14	41.83	22.02	35.27	53.67
100	102.9	98.58	103.7	111.8	80.44
200	214.6	205.3	255.2	183.4	224.7
500	496.8	514	459	503.5	547.1
1000	1070	1059	1029	1076	990.6
3000	2907	2971	2911	2906	3000
5000	5059	5020	5048	5014	4980
10000	9974	9749	9897	10100	9836

a high threshold for trace elemental analysis of the steel alloying elements. Likewise, Zr is apparently used in the processing of the test tubes used to hold the digested salt samples. Therefore our Zr results are buried in the noise of the interferences caused by the sampling method. The same is true for nickel and the steels below certain concentrations. That said, the 316 stainless steel sample had *ample* Fe in the salt sampled during the experiments. Therefore a comparison can be made between the refractory materials: Nb, Ta, and W and the stainless steel run. HT9 and T91 did not lose enough material to the salt to surpass the interferences concentration region. These results can be found in the results section of this dissertation, Section 5.

4.3.5 SEM Preparation and Tension Testing

Lastly, the characterization of the metal samples remains. Three samples are collected for each experiment: a control sample, (which has only been through the metal prep process discussed above), an SEM sample, and a sample for tension

testing. The 'dog bone' shape of each sample is specifically for tension testing, and for the SEM characterization these samples are sectioned using a diamond saw at CAES. For each material, a control sample top-down surface sample and cross section sample were potted in a conductive graphite resin alongside two surface samples and one cross section sample of the salt exposed sample. The cross sections are the most valuable for the purpose of comparison. Theses samples are then polished for SEM and EDS characterization on the FEI Quanta 600 FE-SEM at the Microscopy and Imaging Center at Texas A&M University. The Quanta has a voltage range of 200 V to 30 kV, with beam current > 100nA. The resolution is stated as 1.2 nm at 30 kV, using the Everhart-Thornley (secondary electron) detector, with a magnification capability of 7-2MX. SEM micrographs for select samples can be found in Section 5 of this dissertation

Tension testing is performed in the High Bay Structural and Materials Testing Laboratory at Texas A&M. Figure 4.21 displays the set up for tension testing in that facility. It is also capable of high temperature tension testing. The gauge displayed in the image to the left is a strain gauge. Some samples were not able to be tested in this unit due to sample thickness, a restriction I was not aware of before the testing. Therefore, if an experiment of this type were to be run again, samples approximately 1 mm in thickness will be optimal for testing in the existing facility.

Figure 4.21: The tensionmeter at the High Bay Structural and Materials Testing Laboratory with strain gauge fixed to an NVD Nickel sample (left) and the necking displayed in the sample after testing (right). Samples from the 24 hour corrosion experiments were tested on this instrument though some were too thick to complete the tension test, without breaking the pins supplied by the Mechanical Engineering department.

4.4 100 Hour Salt Corrosion Experiment

Learning from the 24 hour static corrosion tests, a 100 hour static test of commercially pure Ni-200/201 is designed. The sample is polished to 0.05 μm using SiC grinding discs to 1200 grit and diamond polishing paste and colloidal silica to achieve the final polish. The salt chosen for the experiment is NaCl-CeCl$_3$, a NaCl-PuCl$_3$ surrogate eutectic. This salt system is also proposed for the simultaneous salt corrosion and irradiation damage experiment (SCID) as a surrogate chloride fuel salt. The melt point of the eutectic is 495 °C. The SCID experimental operating temperature is 550 °C. Therefore the target set point for the 100 hour corrosion test is also 550 °C.

The crucible material plays a role in the corrosion behavior of the system, as noted in the previous experiment when Al was found in the molten salt samples taken for ICP-MS investigation. Luke Olson also noted this in his dissertation on fluoride salt corrosion.[36] Therefore, the crucible for the 100 hour corrosion test was machined out of the same commercially pure nickel rod stock as the sample. The interior of the crucible was ground to reduce surface roughness. Both the sample and the crucible were ultrasonically cleaned in acetone and ethanol to remove surface contaminants from the machining and grinding/polishing procedures. The sample and crucible were loaded into an argon glove box to prevent surface oxidation.

The salts used for this experiment were purchased from Alfa Aesar: Ultra-dry NaCl, the same as ordered for the phase diagram investigations, specified at 99.99% pure and $CeCl_3$ anhydrous 99.5% (REO). The salts were received at Texas A&M and kept in the argon glove box. It is important to note here that the argon supply to the ARL glove box is commercially pure, known to have CO_2 contamination. For an ideal test, high purity argon with a glove box on line regenerator is preferred.

As stated in previous sections, the extent of corrosion due to molten salt exposure is greatly enhanced by the H_2O, O_2, and other containment concentrations. Therefore, the corrosion assembly, (nickel crucible, salt, and sample), is sealed inside a conflat assembly in the glove box. 2 3/4 inch (70 mm) conflat assembly is used. The gaskets available to make the knife-edge seal were copper. Copper is prone to rapid salt corrosion. To protect the seal and avoid an gas leaks during the test, silver foil was placed on the interior seals. The foil is sufficiently thin and soft to allow the knife-edge to bite into it and the copper gasket simultaneously.

The density of the NaCl-$CeCl_3$ eutectic composition was calculated using the PIM molecular dynamics model described in Section 3 of this dissertation. With a density of 1.9 g/cc, 11.1 g of dry eutectic is necessary to fully immerse the sample

and provide an approximate surface area to volume ratio of that in an ADAM core. The salt was weighed and mixed in the glove box, loaded into the nickel crucible, and the sample placed on top of the dry salt powder. The crucible with salt and sample is then loaded into the conflat assembly and sealed inside the glove box, and then transferred out to the ARL furnace.
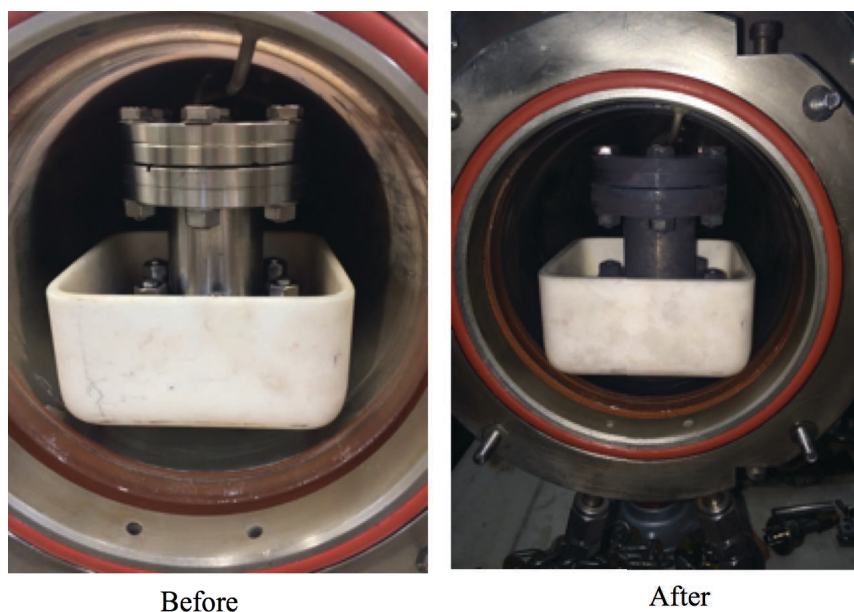
Before   After

Figure 4.22: The conflat assembly before the 100 hour corrosion test (left) and after (right). Commercially pure argon was purged throughout the duration of the experiment; however commercially pure argon does not provide a sufficiently inert atmosphere to avoid oxidation of the the stainless steel assembly.

The furnace used for this experiment is an 8 inch (203.2 mm) diameter tube furnace. A witness/sample thermocouple was used in a preliminary heating cycle to determine the appropriate set point for the controller to ensure 550 °C at the sample's location. The set point is found to be 567 °C to ensure 550 °C at the sample location with gas flowing. The conflat assembly is placed in an Al_2O_3 boat

as a ternary level of containment to prevent, in the event of a leak, the etching of the quartz tube by the molten salt. The furnace is evacuated using a roughing pump and purged with argon three times to minimize the amount of air in the system to avoid excessive oxidation of the conflat assembly. The furnace is then ramped to the melt point of NaCl (801 °C) to facilitate full melting of the salt. Once at temperature, the furnace temperature is lowered to 550 °C for the remainder of the 100 hour corrosion test. The conflat assembly before and after test can be seen in Figure 4.22.

The conflat assembly does experience oxidation during the test due to the impurities in the commercially pure argon. The silver on copper seal proved sufficient to prevent gas leaks either in or out the the assembly. The intact silver foil and copper gasket are displayed in Figure 4.23.

Figure 4.23: Image taken after opening the conflat end cap at the top of the corrosion assembly. The silver foil used was successful in both protecting the copper gasket from the salt vapor and sealing the interior of the corrosion assembly.

The interior of the assembly did have some oxidation from the use of commercially pure argon in the glove box. In future tests, silver foil could be used on the inside of the assembly to prevent FeO contamination in the salt. The microscopy analysis and results can be found in Section 5 of this dissertation.

4.5   SCID Sample Design and Preparation

The simultaneous salt corrosion and irradiation damage (SCID) sample design needs to allow for both a thinned section between 80-90 μm in thickness for the proton beam to pass through and a thick 2 mm section to make the vacuum seal. A previous experiment made the sample domed to allow for more structural support in the sample.[63] However with a domed sample, precise prediction of the damage dose is difficult to calculate since the thickness varies. As we learned modeling in SRIM, thickness changes of even just a micron or two can drastically effect the damage induced. Therefore, the thinned portion was designed to be flat, and the radius in the corners of the thinned diameter where the sample transitions to the 2 mm thick portion were designed to minimize the stress on the center of the thinned portion. A mechanical drawing of the proposed sample is displayed in Figure 4.24.

Initially the sample was designed to be produced via a combination of electric discharge machining (EDM) steps and electro-polished to produce a precision final sample. NVD nickel is proposed to make the vessel liner, and therefore was investigated for use as the window. During EDM sectioning of tensile test samples of the NVD, large holes were found in the interior of a large plate produced. The plate was 1 inch (25.4 mm) thick, and it is assumed that at some point during the deposition the grains could not nucleate efficiently, and therefore large, macroscopic voids were formed. NVD material is inherently susceptible to the formation of micropores throughout the grain structure, however these cracks were much larger than what
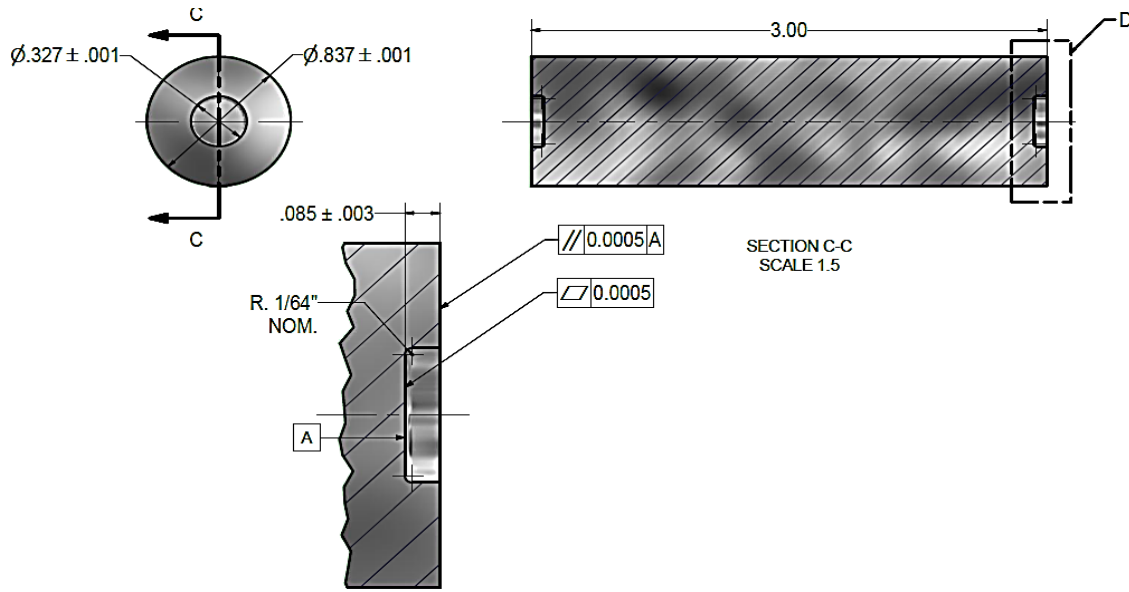
Figure 4.24: The SCID sample mechanical design is displayed here. The units of the mechanical drawing are in inches.

had been seen before. An SEM micrograph of one crack can be seen in Figure 4.25 More on the NVD microstructure can be found in Appendix 1.

Therefore, commercially pure Ni is chosen for the sample material in this test. In step one, we turned down a piece of inch long commercially pure nickel (Ni 200/201) bar stock to the proper OD of a typical 1 1/3 inch (33.9 mm) conflat gasket. The bar stock was faced on each end using a wire EDM, to provide a flat, parallel surface to work with. Then a precision depression was plunged into each face using a plunge EDM. This provides a precision, flat face that will be the surface the beam passes through. The plunge EDM can allow for a precision flatness specification on the window surface, however the finish is not ideal.

The best route identified to polish this surface utilized a lathe, polishing compound, and q-tips. The soft q-tip end minimized the material removal, and the small diameter of the q-tip allowed the diamond compound contact point with the surface
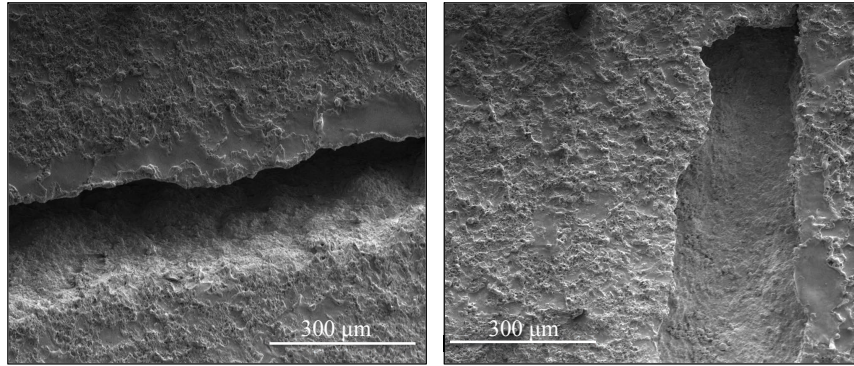
Figure 4.25: Large crack found in 1 inch (25.4 mm) thick NVD nickel slab. The material around the crack appears to be amorphous, indicating a lack of grain nucleation in this region.

to be varied- keeping the flatness of the EDM surface relatively intact. A picture of the polishing setup is displayed in Figure 4.26.

After a mirror surface is achieved, the sample, still on the rod stock, is put through an 8-12 hour 750 °C anneal in a reducing atmosphere to relieve the stress induced in the surface from polishing. Without this anneal, the samples proved to tear on the wire EDM when being cut to the final dimension. Evidence of the induced strain was seen using SEM. Figure 4.27 shows the torn sample and SEM image displaying the results of the strained surface, which relieved and tore on the wire EDM.

Figure 4.26: Polishing the beam window surface using a lathe, polishing compound and q-tips.
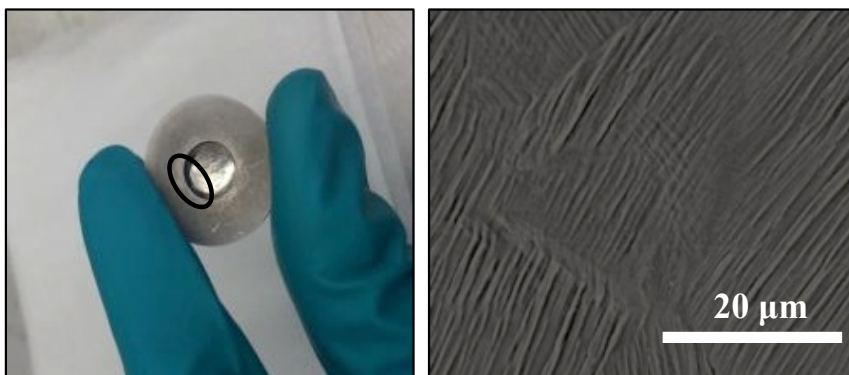
Figure 4.27: A window-gasket cut on the EDM without being first annealed after polishing. The sample with the tear along the edge (left) and an SEM image displaying the lines of strain in the material (right).

After the first anneal, the sample is cut from the remaining rod stock using a wire EDM. The wire EDM also leaves a flat but rough surface finish. Therefore, 76 μm of additional material is left on the backside of the sample. The depression is then filled with crystal-bond, to provide structural support to the thinned section, as the

sample is mounted and polished to the final thickness. Due to the very involved, hands-on sample preparation process there is some varying thickness on the order of 5-10 μm across the entire surface. That said, in the region of interest, a few square mm area in the center of the sample, the flatness was measured to be within a couple of microns.

Four samples were prepared that met specification. One sample is used for a pressure test of the sample. The sample is mounted in a 1 1/3 inch (33.9 mm) conflat and pressurized to 2 ATM differential pressure at 600 °C and left for 100 hours. No leaks were detected during this time. Another sample is mounted on the beam line and tested at high vacuum. Again, no leaks were identified. The remaining samples are reserved for use in the SCID experiment, with one left as a backup sample.

4.6 Sample Thickness Determination Using Protons

The thickness of the beam window is measured both with depth micrometer and a micrometer fitted with point adapters to allow for multiple measurements across the depressed surface. The thickness is measured to be 88 μm. While the desired thickness is between 80-85 μm, sample preparation proved less precise than initially suspected. The samples started to dome below 100 μm when remounted for polishing. Therefore, it was decided to move forward with this SCID sample without risking doming the sample in an attempt to get the window thinner.

The micrometer used is specified to be accurate within ± 2 μm. The damage induced on the back surface is sensitive to within that tolerance, so another method to determine the final beam energy is employed. A proton transmission tests are performed at a range of energies and the transmitted peak energy detected. The detected peak is then compared to TRIM to identify the residual energy anticipated

for the incident energy. The SCID sample is mounted in a vacuum chamber at the end of the Tandem accelerator beam line in the IBML. Low current (0.25 nA) is used to avoid heating and damage to the sample during testing. A scintillator is places to the right of the sample to visualize the beam, and then the sample is moved into the scintillators place. A detector is mounted 170 mm from the target at a 10 ° angle. An aperture is placed between the sample and the detector to limit the current on the detector. The beam energies tested ranged from 5.6 MeV to 5.8 MeV. The collection time for each cycle is 10 seconds. The energy detected is plotted in Figure 4.28.
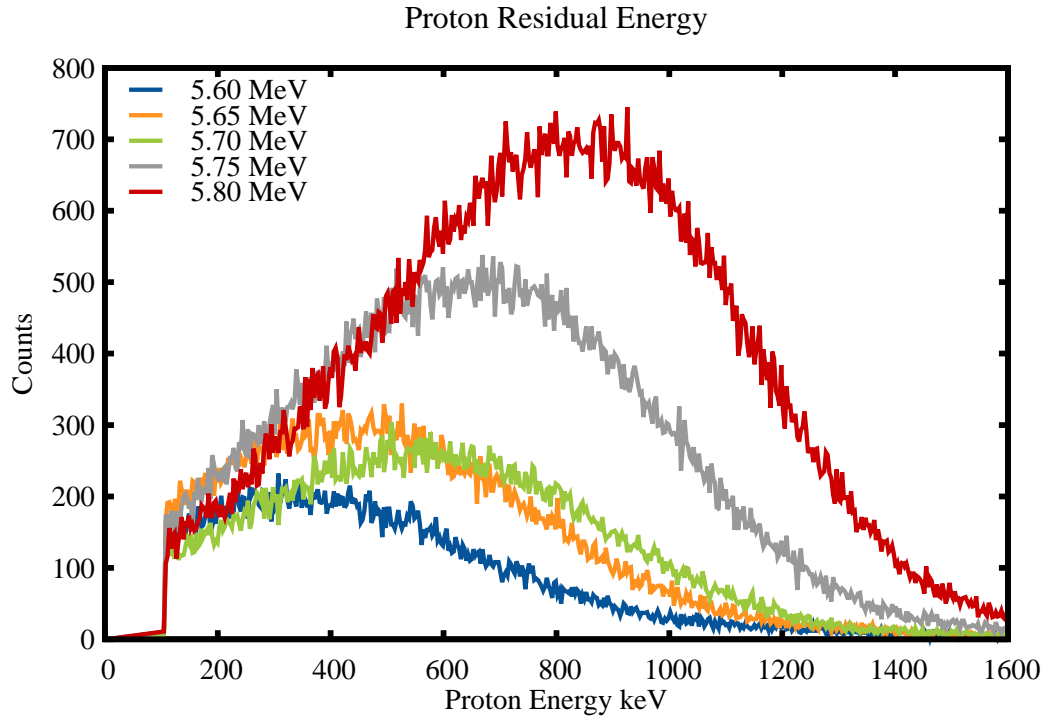
Figure 4.28: The energy recorded by a silicon detector of the protons transmitted through the SCID sample at energies varying from 5.6-5.8 MeV.

Running several SRIM models, varying the thickness and incident beam energy, I can compare the residual energy to that detected experimentally. An example of a modeled system is assigning Layer 1 in SRIM as Ni that is 90 μm thick followed by a layer of Si, the detector material. The residual energy is calculated by subtracting the energy loss to electronic and nuclear interactions from the incident beam energy. Then the residual energy as a function of sample depth can be calculated. Comparing the calculated energies to the experimentally recorded peak, the sample thickness can be determined. For each of the recorded energy spectra, the peak correlates to a nickel sample of thickness 89.6-90.1 μm. Therefore, a sample of 90 μm thick is assumed. SRIM calculations to determine the optimal beam energy were performed, as described in Section 3 of this dissertation. To sit on the shoulder of the Bragg peak of the damage deposited on the salt interface, a beam energy of 5.8 MeV is required. More on the beam parameters run on the SCID 1 experiment is detailed in the following section.

4.7   Beam Detection during Operation

The fluence of particles during irradiation is requisite to calculate the displacements per atom a sample experiences during an irradiation experiment. Beam current and spot size are the most influential variables in calculating the fluence. In traditional ion bombardment experiments, scintillators can be placed in front of the target to ensure the beam is in the correct location and approximately the size necessary to deposit the damage or implantation necessary for the experiment. During the sample thickness measurement, a scintillator was used to ensure we were placing the beam on the thinned portion of the window gasket. During SCID, this technique is not possible. The beam tube is a 6 inch (152.4 mm) tube with conflat fittings, and the sample capsule fits a 1 1/3 inch (33.9 mm) conflat gasket and flange assembly.

A zero length conflat reducer is not preferred, since the capsule is held at 550 °C. Therefore, the sample is placed at the reduced end of a conical reducer.

During the ICE experiments, an array of quartz pieces were placed around the target. If the beam hit the quartz, it would scintillate and indicate that the beam was no longer aligned with the target. During SCID the length the beam would have to traverse, after passing through the quartz ring, is much longer than it was in ICE. Therefore, if the beam made it through the scintillators, there would be no guarantee that the beam is on target. One can envision a system of mirrors or CCD cameras to remedy this issue. Focal lengths of the camera and mirrors can make this tricky, particularly in a dark vacuum chamber with no scintillators at the end of the conical reducer. A more clever solution was chosen.

Carbon has a unique gamma signature, as does nickel. The (p,γ) ground state transition of an excited ^{12}C gives a unique 4.439 MeV signature. The ^{58}Ni (p,γ) ground state transition sits at 1.454 MeV, coincidentally close to silicon's gamma signature. A graphite disc, machined to sit in the flange of the reducer, provides a carbon source. An aperture, nearly the same size as our desired beam spot size, is located on the beam axis at the center of the graphite disk. Therefore, if the beam interacts with the graphite rather than passing through the aperture, a carbon gamma signature can be detected. Likewise, when the beam is on the sample, a nickel gamma signature is detected. The ratio of these two signals, nickel to carbon, can be maximized by beam steering to ensure the beam is on the sample.

To test this approach, a quartz window was fixed to the conical reducer and a NaI detector employed to monitor the silicon to carbon gamma ratios. The carbon signal was first minimized and visually the spot size was confirmed to be maximized.

It should be noted that this only ensures that the beam is on the sample. The spot size itself is a more tricky parameter to control. As previously stated during the

quartz window test, the beam could be seen scintillating on the quartz. Therefore, the slits in the beam line could be fixed and the spot size manually measured. A balancing act is required to ensure the beam use is maximized. While the slits maintain a well-defined spot size, they absorb a significant portion of the beam. If the slits are broadened, the graphite aperture catches a significant portion of the beam and the current measured by the Faraday cup is greater than the current at the target face. Precisely determining the fluence of the beam is critical to accurately calculating the DPA deposited on the sample. Therefore, it was determined that a smaller spot size, sacrificing a significant amount of beam capability, is preferred.

When the beam interacts with the slits, the current on the slits can be recorded. The current can be balanced on the slits to ensure the beam is centered and minimized on the slits via quadrupole focusing of the beam. The slit readouts allow us to ensure the spot size is controlled by the slit dimensions, as long as current is deposited on the slits.

4.8 Experimental Setup for Simultaneous corrosion and Irradiation Damage Experiment

A Tandem accelerator beam line at the Ion Beam Materials Laboratory (IBML) is used to perform the simultaneous salt corrosion and irradiation damage experiment on a nickel sample. A proton transmission measurement determined that the sample is 90 μm thick. The salt interface is designed to sit on what is called the "shoulder" of the Bragg peak of damage events in Nickel. See Figure 4.29 for the Bragg peak of 5.8 MeV protons in nickel. The red portion of the plot is the "shoulder" and the furthest right point is the location of the salt/Ni interface of a 90 μm window. The displayed beam profile in Figure 4.29 allows damage most characteristic of neutrons to be simulated on the sample surface in contact with the molten salt. An NaCl-

5.8 MeV Protons in Nickel
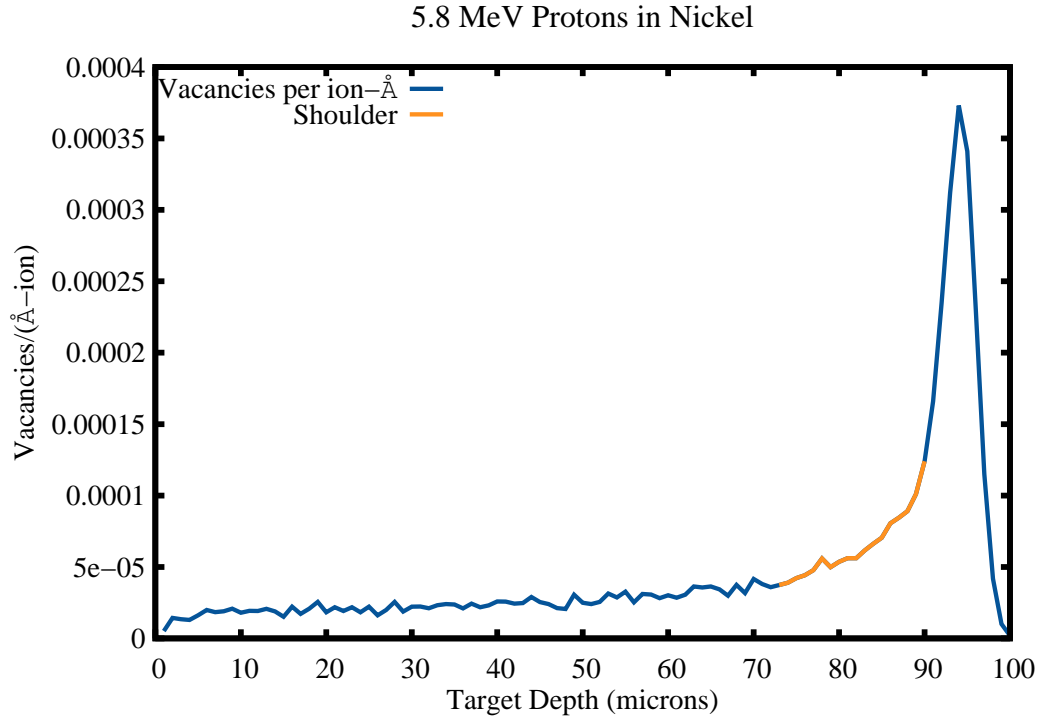
Figure 4.29: the Bragg peak of 5.8 MeV protons in nickel. The red portion of the plot is the "shoulder" and the furthest fight point is the location of the salt/Ni interface of a 90 μm window.

CeCl$_3$ salt composition acts as a surrogate for the fuel salt of an ADAM fission system. The schematic drawing of the experimental setup is detailed in Figure 4.30. To the far right of this assembly sits the small salt capsule which will contain 12 mL of molten salt. The heating jacket has been designed and manufactured at LANL. The sample capsule was designed and produced at Texas A&M, with the machining and tube welding performed at Bailey Tool and Manufacturing and the Texas A&M University High Energy Physics Machine Shop. A picture of the first SCID capsule is displayed in Figure 4.31. The capsule is designed to connect to a 1 1/3 inch (33.9 mm) conflat flange. The IBML beam line ends in a 6 inch (152.4 mm) conflat
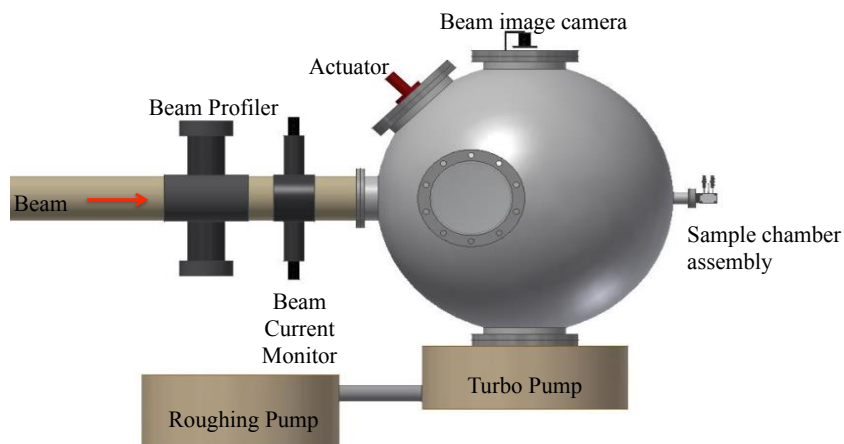
Figure 4.30: Schematic of IBML beam-line to the far right is the SCID experimental chamber.

connection. A conical reducer is used to then step down the SCID capsule. The capsule is machined out of the same nickel rod stock at the sample, minimizing galvanic corrosion due to dissimilar materials. The knife edge machined in the face is the critical sealing surface. The tubes welded to the capsule are to provide an argon purge at the beginning of the experiment and a port for an inconel sheathed
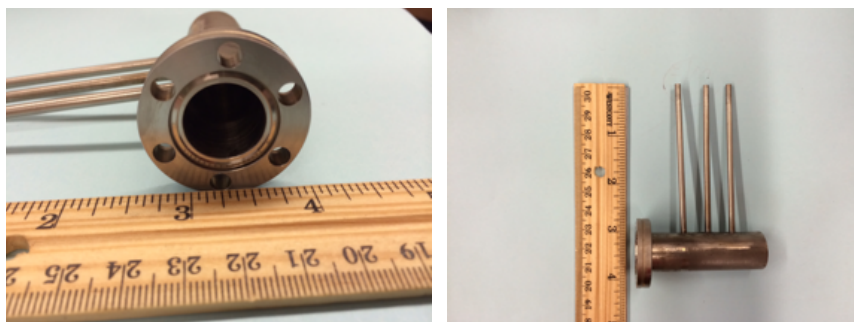
Figure 4.31: Photo of the SCID molten salt capsule. The capsule is designed to contain 12 mL of molten NaCl-CeCl$_3$ salt. The knife edge machined into the face of the capsule makes a seal with the SCID sample and the conical reducer from the beam line.

thermocouple. The heating jacket holds 4 cartridge heaters, which are designed to hold the capsule and salt at 550 °C. The assembly attached to the end of the beam line during a high-vacuum–high-temperature test is displayed in Figure 4.32.
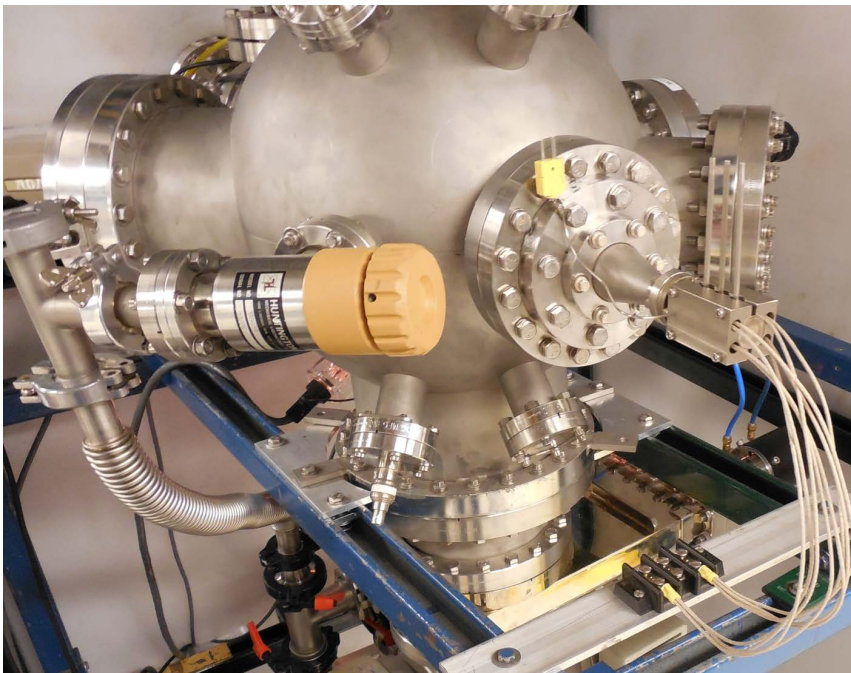
Figure 4.32: The capsule sealed to the beam line with the heating jacket in place during a high vacuum-high temperature test of the nickel on nickel seal.

A thermocouple read out is wired outside of the shielding area, along with the voltage control for the cartridge heaters. The voltage supply to the heaters can be adjusted to either raise or lower the temperature inside the salt capsule.

The beam is aligned using a quartz window to visualize beam size and shape and telescoping lens to observe slit locations down the beam line. The source cathode was replaced, in anticipation of a 70 hour experiment. The salt capsule was loaded and sealed in the nitrogen glove box at the Fuels Research Laboratory at LANL. The

dried $CeCl_3$ (see Section 2) is Spex milled with NaCl, for homogenization. Ideally the capsule would be loaded to 75% capacity, but due to a lowered packing fraction after Spexing, it was loaded to only 60%. The loaded amount is still sufficient to cover the irradiation region.

Inside the glove box, the sample is placed on the knife edge and the conical reducer sealed to the capsule. The gas inlet and outlet tubes are sealed with Swagelok fittings. The entire assembly is transfered to the IBML, and fixed to the beam line. Shielding has to be applied to the entire beam line and sample area to shield personnel from emitted gamma rays and produced neutrons from the beam interaction with both the sample and the slits along the beam line. A graphite aperture is placed between the conical reducer and the IBML beam tube to allow beam detection. The previous section goes into detail on beam detection on sample.

The salt sample assembly is brought up to 550 °C and left to equilibrate for 24 hours. Approximately 6 hours into the experiment, material deposit near a weld is discovered. Initially it is difficult to determine if this is a weld leak or surface contamination which settled into the crevice during loading. It is decided at this time that high purity argon will be purged throughout the duration of the experiment to minimize O_2 and H_2O contamination. Note, at sample disassembly it is confirm that the weld did in fact leak.

Once all the shielding is in place, the beam is ramped up slowly. Approximately 45 minutes into the experiment, the fast acting valve is triggered due to a drop in the vacuum level by 3 orders of magnitude. The vacuum level immediately returns to 10^{-7} Torr, and therefore the beam is turned back on. Soon after, the valve tripped again, and the experiment is stopped. A salt leak is quickly detected visually. Salt is found inside the conical reducer and the graphite aperture. The capsule is dismounted from conical reducer. No obvious tear or hole is initially seen. Images

90

taken immediately after dismounting the conical reducer from the beam line are shown in Figure 4.33.
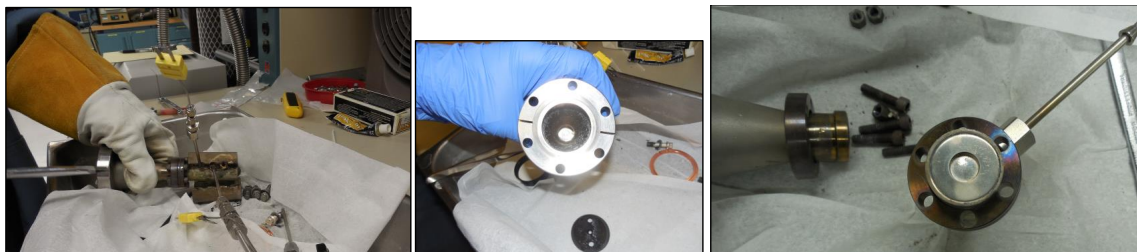
Figure 4.33: Images following the SCID 1 attempt: (Left) removing the thermocouple. The exposed weld joint can be seen where a salt leak corroded the weld and tube to the extent that the tube snapped off upon disassembly. (Middle) a view down the conical reducer where a few grams of salt were found. (Right) the face of the SCID sample where no tearing was found and possible pin holes were identified.

For a leak substantial enough to leak gram quantities of salt in a very short (seconds) amount of time, no large tear or hole was identified. A 200 μm pin hole is later identified as the only sample leak during microscopic investigation.

The sample is at 25 mR at contact, and therefore needs to be isolated to radioactively cool until it has decayed to less than 5 mR on contact with no removable contamination. In less than a week, the sample is cooled from transfer and is taken to the Fuels Research Lab for disassembly and microscopic examination. The results of the post irradiation examination are in Section 5 of this dissertation.

5. EXPERIMENTAL RESULTS AND DISCUSSION

5.1 Phase Diagram Investigation

The melt points of these salt systems are crucial to the modeling of the core neutronics. The melt point determines the minimum operating temperature of the entire core, which is generally chosen to be 50°C higher that the liquidus temperature of the salt. Most of these salt system have nice eutectic binary phase diagrams, like that NaCl-UCl$_3$ phase diagram which was reported in previous years, and was displayed in Section 1 of this dissertation. Since the 1970's, when that particular phase diagram was last investigated experimentally, melt point determinations have become more sophisticated and the environments and salt purities have bettered as well. Discussed in this section will be the results of the phase diagram investigation performed just this past summer in the Fuels Research Laboratory.

5.1.1 UCl$_3$-NaCl

There is specific importance to the NaCl-rich side of the NaCl-UCl$_3$ phase diagram. If a cooling event were to occur during an off-normal even in the ADAM core, NaCl would solidify initially until the eutectic point is reached. At the composition when the eutectic is reached, these will solidify as a NaCl-UCl$_3$ complex. The more dense solid eutectic salt will cause an increase in temperature as the densification facilites more efficient fission. The increase in temperature should melt the salt. If the core is to operate on the actinide rich side, then when a cooling even occurs the actinide salt will solidify and can create hot-spots on the vessel wall. A number of compositions have been tested and the liquidus and solidus points of the melts are reported in Table 5.1. Plotting the data along with the phase diagrams of Beneš and Taube, we see that the curvature on the NaCl rich side of the phase diagram

Table 5.1: Table of Liquidus and Solidus Temperature of a Range of Mole Fractions in the NaCl-UCl$_3$ Binary System.

Mole Fraction		Liquidus	Solidus
UCl$_3$	NaCl	($\pm 2°$C)	($\pm 2°$C)
1	0	842.3	842.3
0.61	0.39	712	520.5
0.557	0.443	687	522
0.336	0.664	523	523
0.226	0.774	661	522
0.122	0.878	747	523
0	1	802.1	802.1

is significantly different, up to 30-40 °C at points; see Figure 5.1. The higher liquidus points on this diagram indicate that the core will have to operate at higher temperature to avoid solidification in the cool sections of the heat exchanger.

The NaCl-PuCl$_3$ diagrams which have been studied to date exhibit similar curvature to those from 1978 and 2008, which lead me to think that an investigation of that phase diagram will prove beneficial, if the behavior of the system is similar to the UCl$_3$ system. The agreement on the UCl$_3$ rich side of the phase diagram and eutectic point indicates that a systematic error could exist in the calculation of the NaCl-rich side of the diagram.

5.1.2 CeCl$_3$-UCl$_3$-NaCl

CeCl$_3$ is used in these studies as a surrogate for PuCl$_3$. Pu is expensive and difficult to work with due to both its proliferation hazard and toxicity. The study of the CeCl$_3$-UCl$_3$-NaCl phase diagram aims to first and foremost pin down the proper technique to probe the ternary system. Collaborators at LANL can, at some point, investigate the PuCl$_3$ containing system. The secondary goal of this side of the project is to assess CeCl$_3$ as a surrogate for PuCl$_3$. That said, the PuCl$_3$ side of
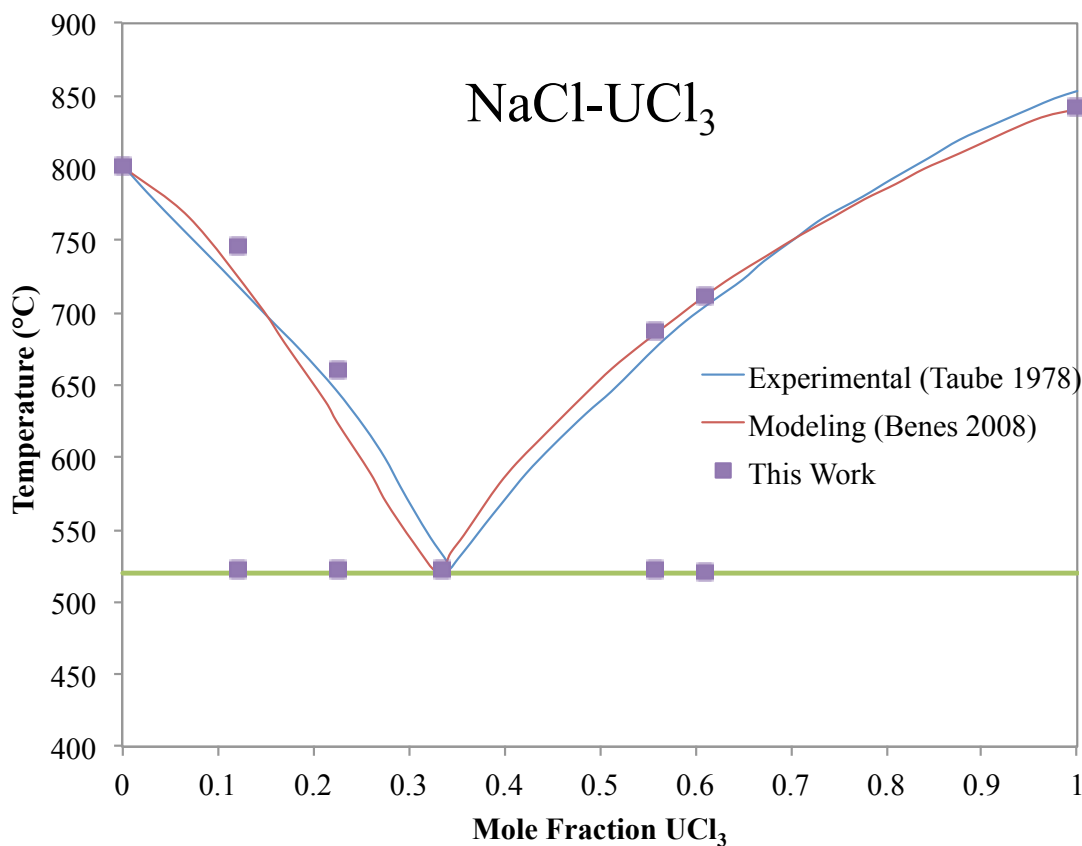
Figure 5.1: The NaCl-UCl$_3$ melt point results plotted along side the experimental results from Taube in 1978[64] and the modeled results of Benes in 2008.[17]

the study must be performed before a proper comparison of the two systems can be made. The solidus and liquidus points for a number of compositions is displayed in Table 5.2.

Note that there are very few compositions which contain high molar percentages of UCl$_3$ and CeCl$_3$. in trying to measure the binary phase diagram between these two high melt point salts, the crucibles were consistently compromised. These crucibles are designed to withstand high pressure, however there internal pressure of the crucibles above 801 °C is enough to cause a rupture in the sealing disc. Therefore,

Table 5.2: Table of Liquidus and Solidus Temperature of a Range of Mole Fractions in the NaCl-UCl$_3$ Binary System.

| Mole Fraction | | | Liquidus | Solidus |
UCl$_3$	CeCl$_3$	NaCl	(±2°C)	(±2°C)
1	0	0	842.3	842.3
0.557	0.443	0	687	522
0.336	0.664	0	523	523
0.226	0.774	0	661	522
0.122	0.878	0	747	523
0.61	0.39	0	714.1	520.5
0	1	0	802.1	802.1
0.46	0.38	0.16	715.8	511.2
0.2	0.56	0.24	621.5	507.4
0.16	0.59	0.25	588.7	497.8
0.1	0.6	0.3	571	501.4
0.16	0.62	0.22	559.5	502.3
0.31	0.39	0.3	698.5	506.1
0.2	0.54	0.26	605	506.9
0	0.7	0.3	495	495

a different method will be necessary to measure the UCl$_3$-CeCl$_3$ binary and heavy metal chloride rich portion of the ternary phase diagram.

Using data from the FactSage Database for the NaCl-CeCl$_3$ side of the ternary phase diagram, the data collected here can be combined to plot a ternary phase liquid surface. Figure 5.2 displays the liquid surface of the NaCl-UCl$_3$-CeCl$_3$ system as measured here. The dark green areas are the lowest melt portion of the diagram and are the most thermally ideal compositions to operate with. Investigation of the NaCl-CeCl$_3$-UCl$_3$ systems correlation with the NaCl-PuCl$_3$-UCl$_3$ system will hopefully continue in FY2015. It is expected that there will be a reduction in these compositions by approximately 50 °C, as the melt point of CeCl$_3$ is 50 °C higher than PuCl$_3$. The same trend is true in their binaries with NaCl.
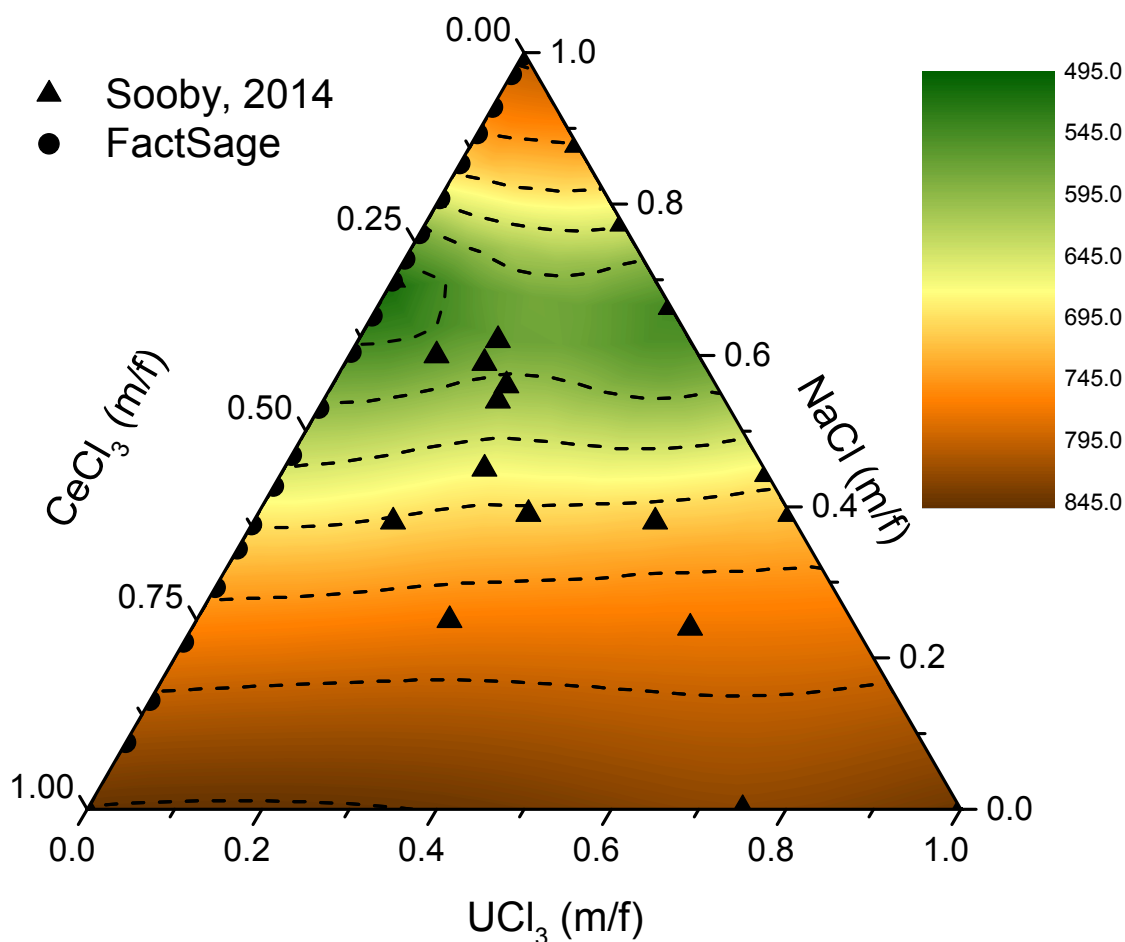
Figure 5.2: The contour plot displays the liquid surface of the NaCl-UCl$_3$-CeCl$_3$ system. The system is a surrogate fuel complex for the ADAM core. The darkest green portions are ideal thermal conditions for the core. The CeCl$_3$-NaCl binary points, represented by circles, are data extrapolated from the FactSage online database.[65]

5.2   24 hour Static Corrosion Test Comparing Bromide and Chloride Salt Corrosion of Metals

Eleven metals were tested in both molten chloride and bromide salts. In an attempt to minimize the variables at play in such a large sample set the salt temperature, sample preparation, and characterization methods were held constant. The sample preparation and experimental methods were discussed in Section 4. There

are four forms of characterization attempted for each metal-salt pair: visual observations, SEM imaging, tensile testing, and salt characterization via ICP-MS. Perhaps the most telling characterization is that performed by simple visual observations of the experiments while they were running as well as observations of the resulting salt and metal products. The thickness change of the alloy in each metal-salt pair is discussed in length in Section 4. To summarize those results, a comparative chart can be found in Figure 5.3. Combining this thickness change with the ICP-MS data
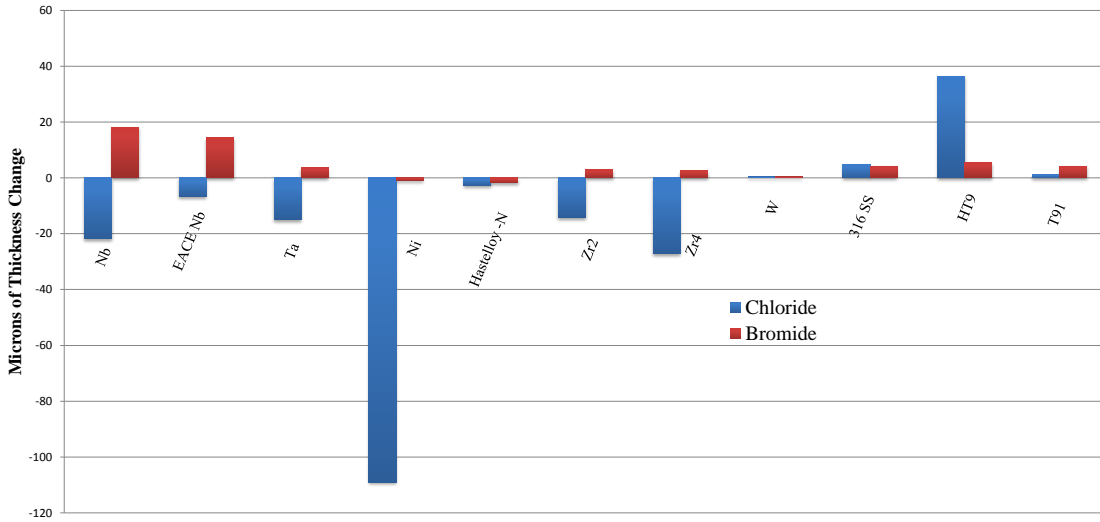
Figure 5.3: Plotted is the thickness change of each alloy exposed to the 700 °C LiCl-KCl (blue) compared to the LiBr-KBr (red) for 24 hours.

helps to describe the corrosion behavior in each of these systems.

5.2.1   The Refractory Metals

Niobium and Tantalum displayed a distinct pattern in their concentrations in the salt over time. The analysis for these samples is performed twice to verify the

validity of the trend. The data for the ECAE niobium, as received niobium, and as received tantalum is displayed in Figure 5.4. The ECAE (equal channel angular
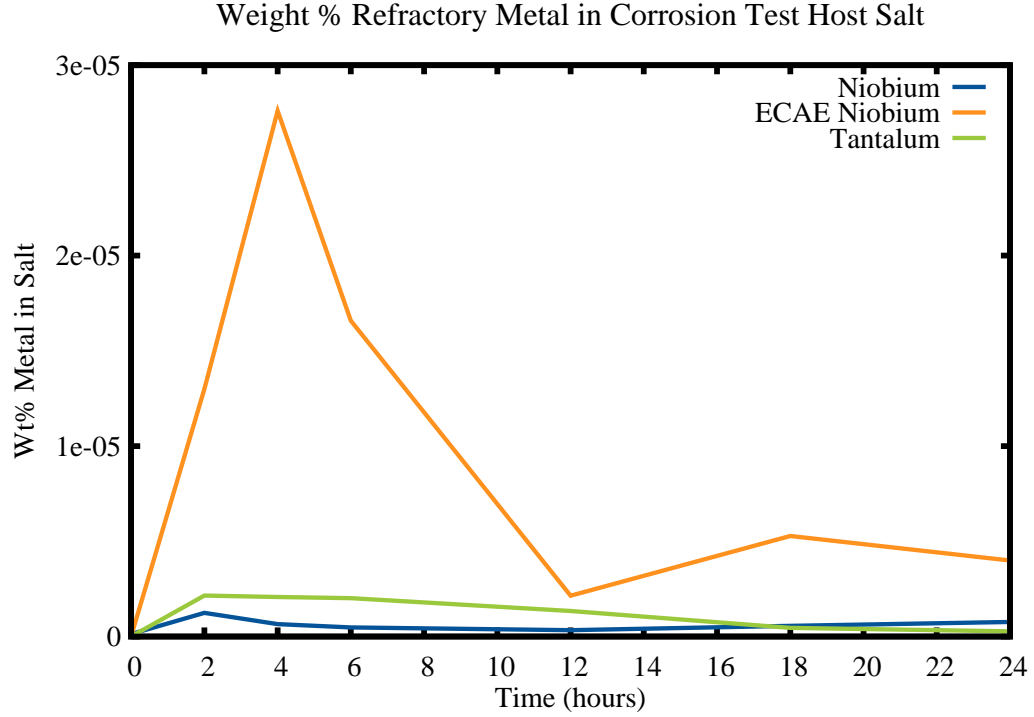
Figure 5.4: Wt % metal in the host salt as a function of time. The red trend is Equal Channel Angular Extrusion Niobium, a cold world Nb which is displaying more Nb in the host salt than the as-received Nb and Ta.

extrusion) is a cold worked niobium provided by Prof. Hartwig's research group. Judging by the higher peak in concentration at the four hour interval, it appears that the grain boundary working of this material causes it to be more susceptible to molten salt corrosion. Referring back to the thickness results, the sample showed the

least amount of thickness change amount these three samples. Therefore, I believe the primary corrosion method for these metals is at the grain boundaries, and the cold working facilitated more etching in the ECAE case.

Weight % Refractory Metal in Corrosion Test Host Salt
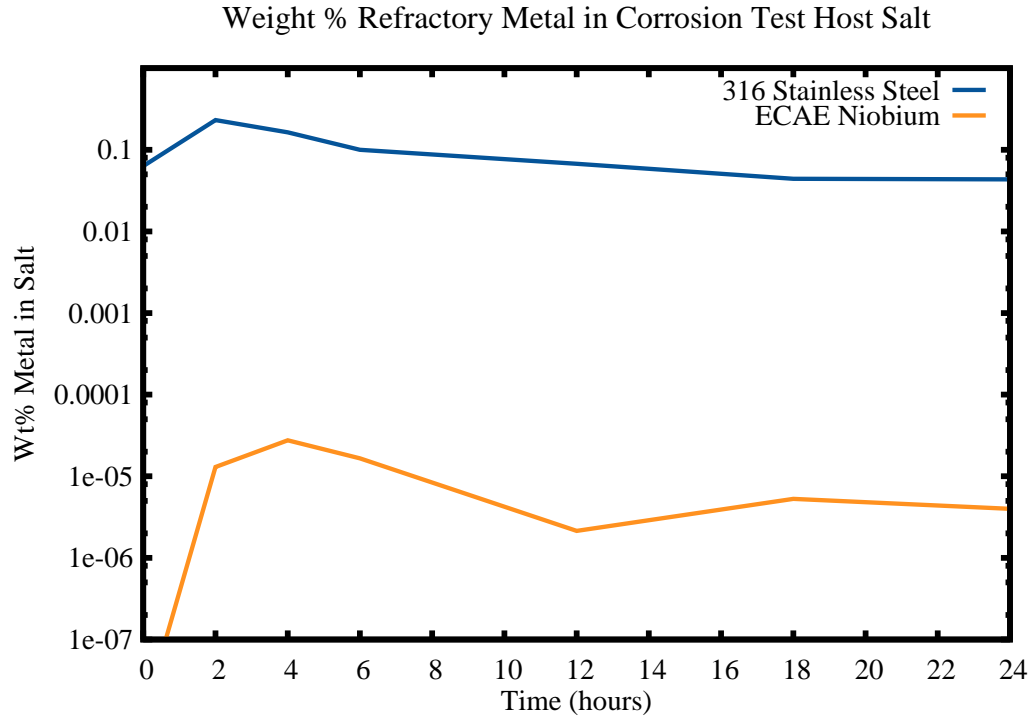
Figure 5.5: Wt % metal found in the host salt as a function of time for 316 stainless steel and ECAE Nb, as analyzed via ICP-MS.

5.2.2   Steels

In both the chloride and the bromide corrosion sets of experiments the steels increased in thickness. It is typical of steels to form oxidative layers in corrosive

environments. The ICP-MS data provides strong evidence that we are also losing Fe to the salt during this process. A comparison between the ECAE sample mentioned above and the iron lost to the salt in the 316 Stainless Steel experiment is displayed in Figure 5.5. Note the y-axis is a logarithmic scale. The initial value of the stainless steel data speaks to the higher noise threshold discussed in Section 4. The wt% Fe found in both the T91 and HT9 samples are too low to surpass the interference threshold. Likewise, the steel alloying elements, including Ni, did not surpass their thresholds.

For the SEM analysis, surface preparation is key to identify the salt corrosion effects vs surface roughness and etching. The T91 sample showed some signs of corrosion, however I did not find the oxide layer we expected to see; however if the oxide is brittle, it could have been sloughed off during segmentation on the diamond saw. The T91 sample cross section is displayed in Figure 5.6.

Tension testing is performed on 7 of the 22 samples. Some samples failed during testing, and others caused the pins used to pull the sample to fail due to increased ductility. Of the samples tested, there is an indication that the exposure to bromide salt actually increased the yield strength of a the refractory metals. In the future, several samples should be exposed to obtain more accurate and statistically relevant results and the control sample needs to be thermally annealed, to ensure it is in the same stress state.
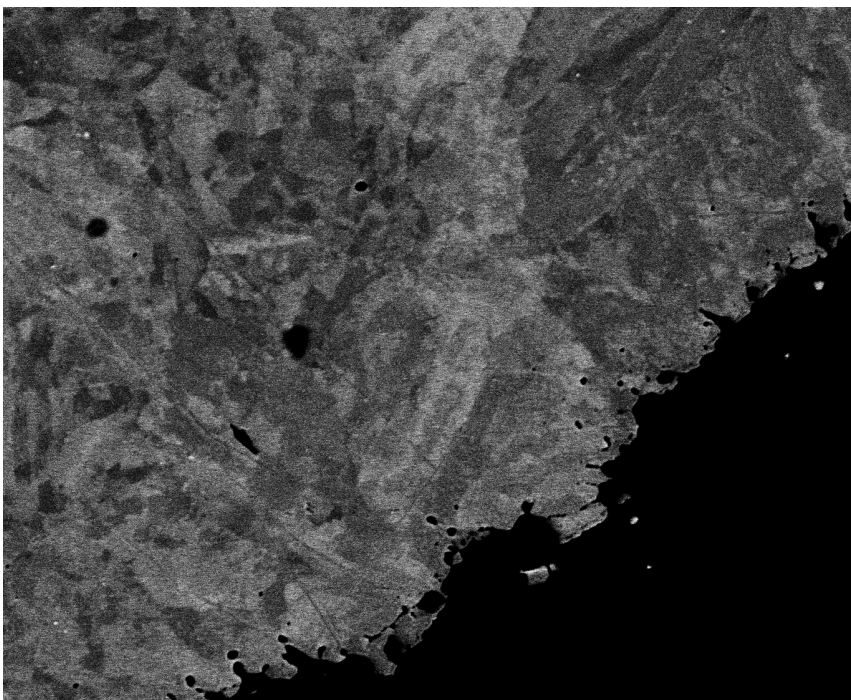
Figure 5.6: The cross section of the T91 steel sample after exposure to LiCl-KCl.

5.3 100 hour Salt Corrosion Results

Prior to introduction to the glove box, the sample is measured in five locations using micrometers fixed with point adapters. The specific location of each measurement cannot be confirmed, as the point adapters measure a very small portion of the sample. The measurements at each quadrant and in the center vary, however the average across the sample shows no change, within the error of the measurement device, as shown in Table 5.3. The sample entered the melt with a mirror finish and by the end of the 100 hour exposure the surface appears etched. Figure 5.7 shows the top-down secondary SEM image, revealing what appears to be grain boundary etching. The image to the left in Figure 5.7 is a 200x image, showing a rough surface as shown by the contrast in the secondary electron microscope. The image to the right is an 800x magnification of the same area, displaying the etched grain bound-

101

Table 5.3: Average Thickness across the 100 Hour Corrosion Sample Measured before and after Salt Exposure

100 Hour Corrosion Sample Thickness	Before inches	After inches
Average	0.01102	.0.01104

aries. Zooming in to 1500x, the surface microstructure appears to be ridged. The grains also appear to be overlapping some.
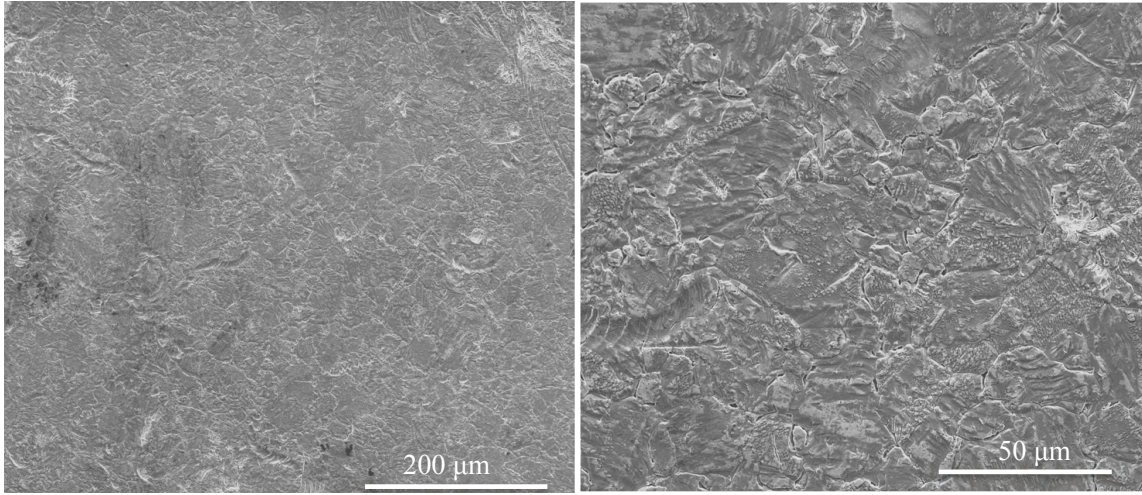
Figure 5.7: A secondary SEM micrograph of a top-down view of the 100 hour corrosion sample at 200x (left) and 800x (right) magnification. The surface appears etched, though the average sample thickness remains the same.
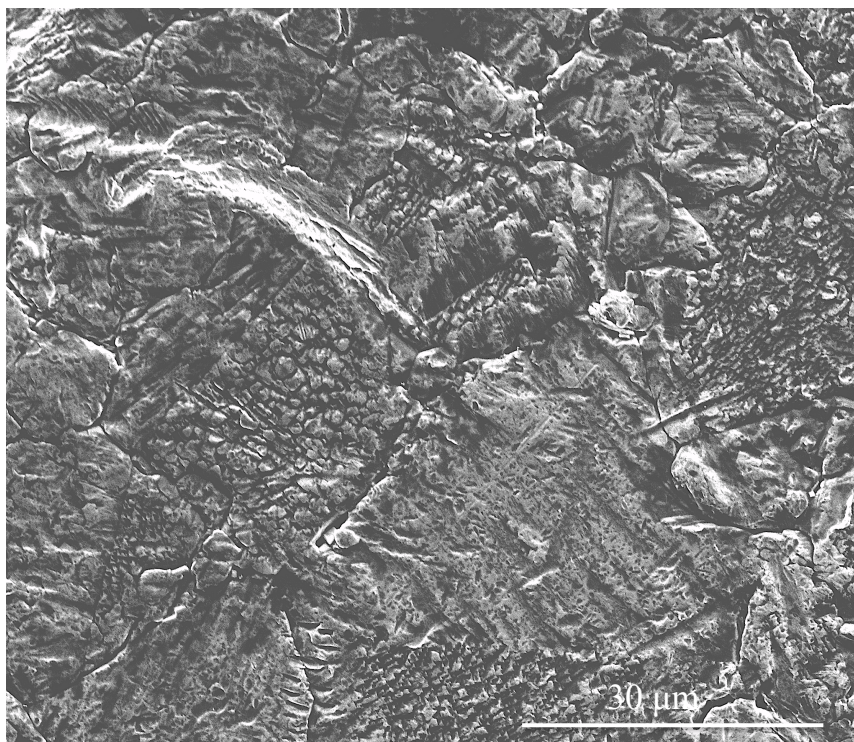
Figure 5.8: A secondary SEM micrograph of a top-down view of the 100 hour corrosion sample at 1500 x. Here we see a ridged structure on the surface. EDS examination only revealed Ni across the surface.

Going to 3000x, in Figure 5.9, the ridging appears to be facetting of the surface grains, which can be typical of some ceramic materials and has been seen in stressed and heat treated metals.[66] The lack of measurable material loss to the surface of the sample indicates that there could be significant grain boundary penetration. To investigate the depth of penetration, an SEM equipped with a Focus Ion Beam mill can allow us to extract a "liftout" from the surface to look at the cross section of the upper few microns. Scott Parker, a Master's student at the University of California at Berkeley working with me in the Fuels Research Laboratory, performed the FIB lift out and thinning for TEM analysis.
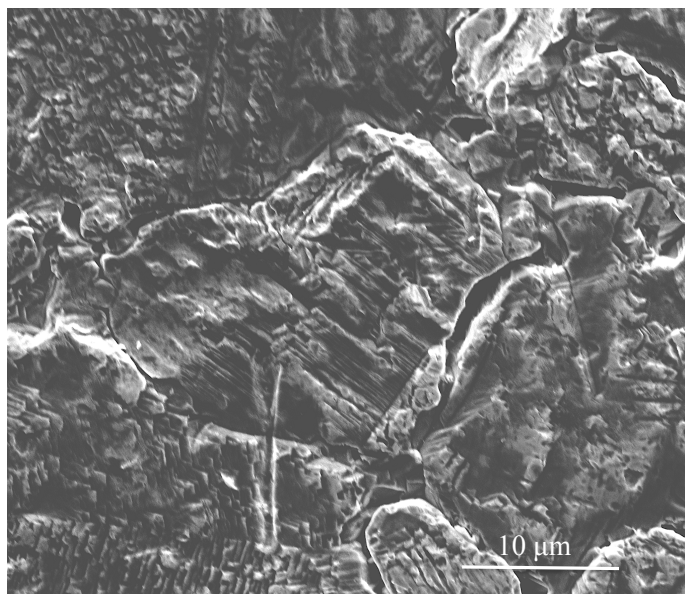
Figure 5.9: A secondary SEM micrograph of a top-down view of the 100 hour corrosion sample at 3000x. Here we see a ridged structure on the surface appears to be faceting. EDS examination only revealed Ni across the surface.

We isolated one grain boundary and milled across it to reveal the depth of the attack. The grain boundary and lift out segment are displayed in Figure 5.10. The lift out exposed a grain boundary which had been etched approximately a micron of material down the surface of the sample. Once the sample is fully thinned, the top region, leading down to the second layer is significantly thinned in the center along the original top boundary. Images taken during the thinning process are displayed in Figure 5.11 The image to the left in Figure 5.11 is of the lifted sample before it is thinned for STEM analysis. The very top portion is the original surface, which was seen in previous figures. The image to the right is after the sample is thinned. In this image a multi-layered sample is revealed, with a crevice in the center. A high resolution STEM image of this thinned sample is displayed in Figure 5.12. The micrograph reveals a layer of metal above the original/native nickel surface. The large crevice in the center is partially void space, and is the original corroded grain
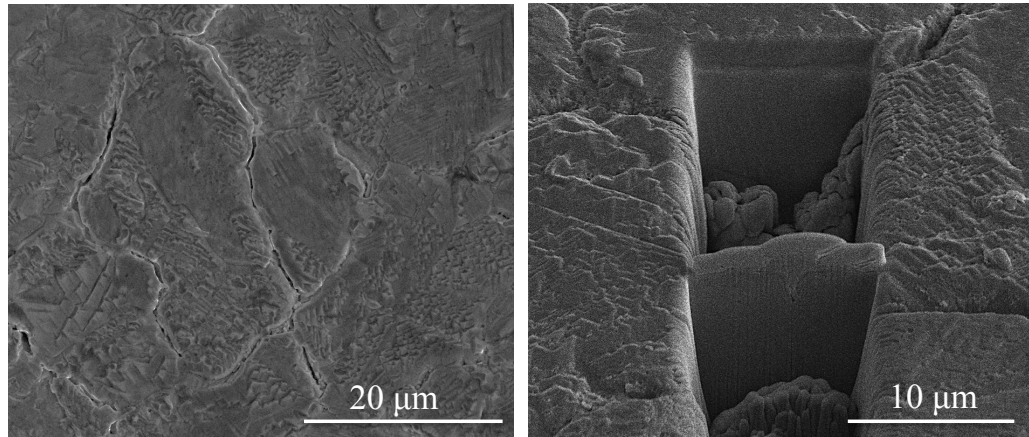
Figure 5.10: Micrograph of the isolated grain boundary and FIB milled region of the corroded sample, prior to lift out.
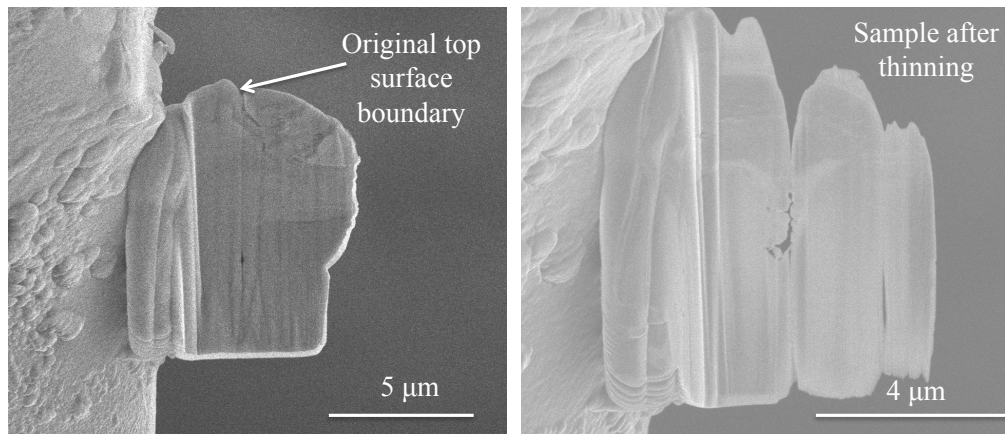
Figure 5.11: Micrographs of the lift out before (left) and after (right) thinning.

boundary. Figure 5.13 displays this sample rotated 90 ° with an EDS line scan performed across the various layers.

The EDS signal confirms that this is in fact nickel which has been plated onto the surface of the corroded grain boundary. As discussed in the early sections of this dissertation, the molten salt is an electrolyte and can facilitate electro-deposition of metals. The visualization of this layer further supports the result of nickel plating
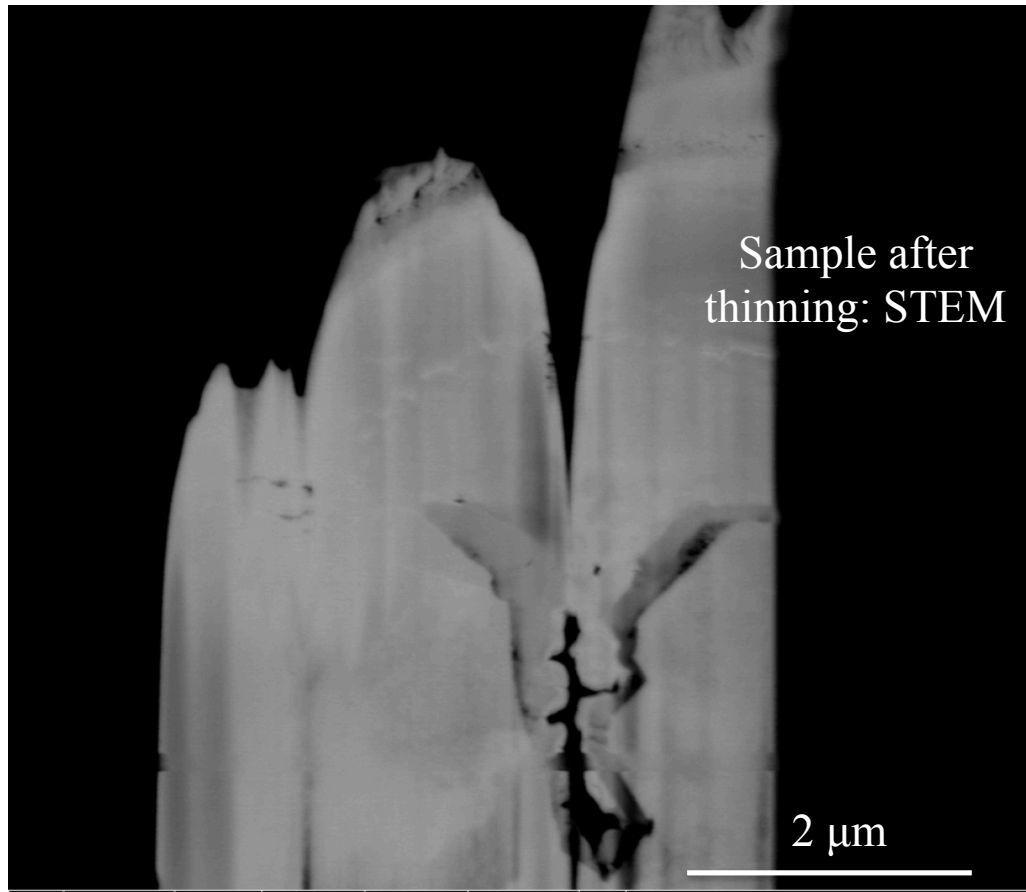
Figure 5.12: STEM micrograph of the thinned FIB lift out. The very top ragged structure is the platinum coating which is plated to help lift the sample. Directly below that is a bi-layer structure leading to what is believed to be the original, corroded grain boundary.

during the 24 hour corrosion test. The uniqueness of this result lies in the plating location. The sample is fully submersed in salt during the 100 hour exposure, unlike in the 24 hour experiment where part of the dogbone was outside of the salt-creating a cold spot. The plating observed in this sample is due to solely the variation in thickness of the sample, rather than a thermal gradient.
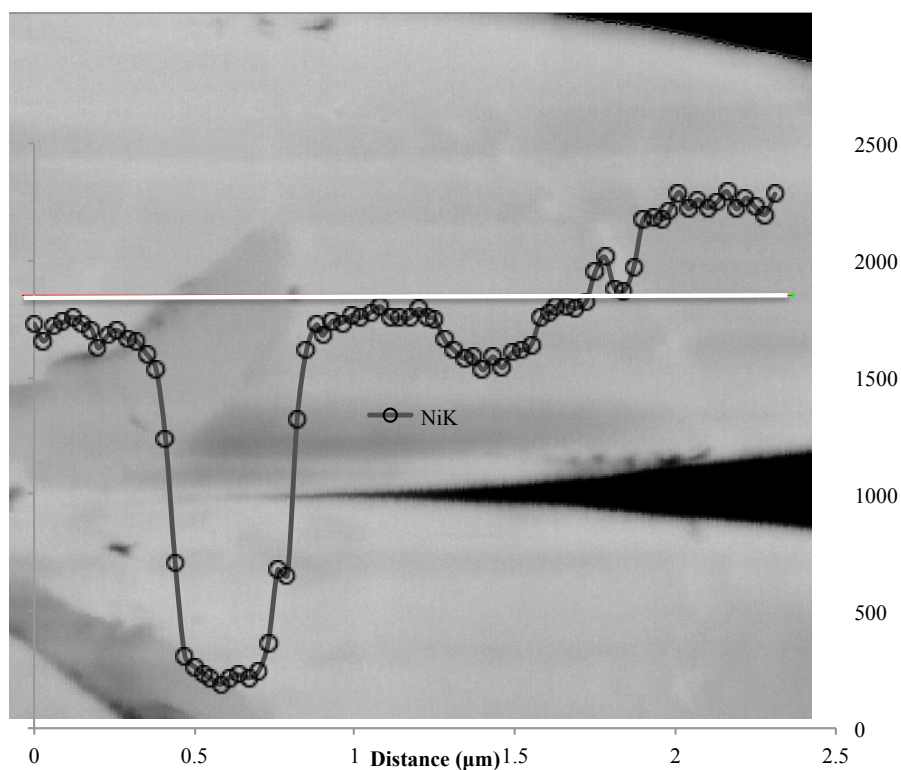
Figure 5.13: The sample has been rotated here 90 ° and a line scan along the white line is performed. The NiK signal intensity (counts) is plotted as a funtion of sample depth.

Lastly, to further emphasize the importance of minimizing corrosion, Figure 5.14 displays a backscatter electron micrograph of the 100 hour corrosion sample.* The bright, rectangular pieces in the grain boundaries and embedded in the grains are salt crystals. EDS revealed that these are primarily NaCl-CeCl$_3$ with significant amounts of F and Si, common contaminants in these salts. The impurities are found only in the salt crystals and not in the rest of the bulk material.

---

*Special thanks to Terry Holesinger, PhD for his help with the final microscopy of the 100 hour corrosion sample.
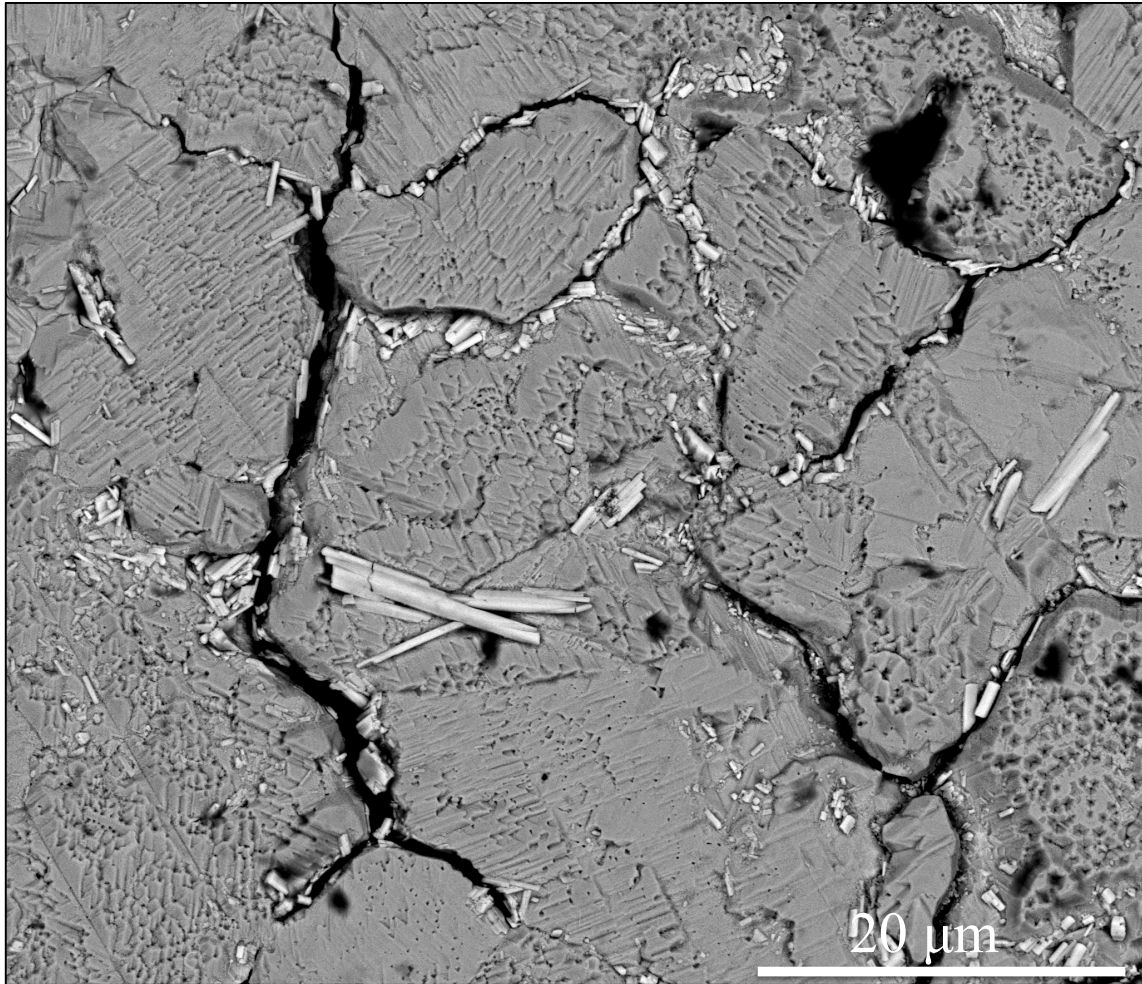
Figure 5.14: BSED micrograph of the 100 hour corrosion sample. The grain faciting is clear in this image, as are salt crystals. EDS spot scans of the salt crystals indicate that they have significant impurity, F and Si, content.

5.4   Salt Corrosion and Irradiation Damage Run 1

The failure of the first run of the molten salt corrosion ion beam irradiation test is assumed to be due to beam heating. Both optical and electron microscopy are employed to analyze the failed sample. Energy dispersive spectroscopy (EDS) is also used to search for any intergrannular corrosion products remaining after the clean-

up of the sample. Thermal modeling of the failure provides insight to the maximum temperature reached on the beam surface.

It took approximately a week for the sample's activation to decay below background. The primary radioactive isotopes activated during the beam time are ^{61}Cu and ^{64}Cu, which have beta decays with half lives of 3.3 and 12 hours, respectively. Once the sample decayed 5 mRem/hr on contact, from the original 24 mRem/hr on contact, it could be transfered to the Fuels Research Laboratory for disassembly and analysis.

Figure 5.15: Displayed here is John Dunwoody carefully opening the molten salt capsule as to avoid both sample deformation and contamination of the lab area with salt.

When disassembling the capsule, care was taken to not to further damage the sample surface. To start, the gas line tubes were removed, and the capsule body opened using tube cutters, as shown below in Figure 5.15. The capsule was sectioned three times, inching closer to the sample. Salt was still in contact with the sample surface, so it was then placed in a beaker of deionized water to dissolve the salt from the sample surface. The beam side of the sample was imaged using an optical

microscope, in the Fuels Research Laboratory. No sample preparation was performed, aside from gently wiping the sample surface of debris from the leak. Once the sample was cleaned, a small pin hole was observed on the beam side. The pin hole can be seen in the photograph in Figure 5.16. The pin hole is located below center of the

Figure 5.16: Displayed here is a photograph the pin hole caused by a failure in the sample.

sample, as it was oriented on the fixturing. The position of the pinhole indicates that the beam was positioned below the center of the sample, which is not optimal. If the failure had been either at the center of the sample or around the edges of the thinned area, a purely mechanical failure would be likely.

Optical microscopy of the beam side of the sample indicated that grain growth in the beam spot occurred. Also, the area of grain growth is limited to the original beam size, leading one to believe that the growth is either caused by irradiation and/or the beam caused significant localized heating. The latter of these is assumed to be the

cause of failure. Optical microscopy images of the beam side of the sample can be seen in Figure 5.17. The left image displays a brightened region which is assumed to be
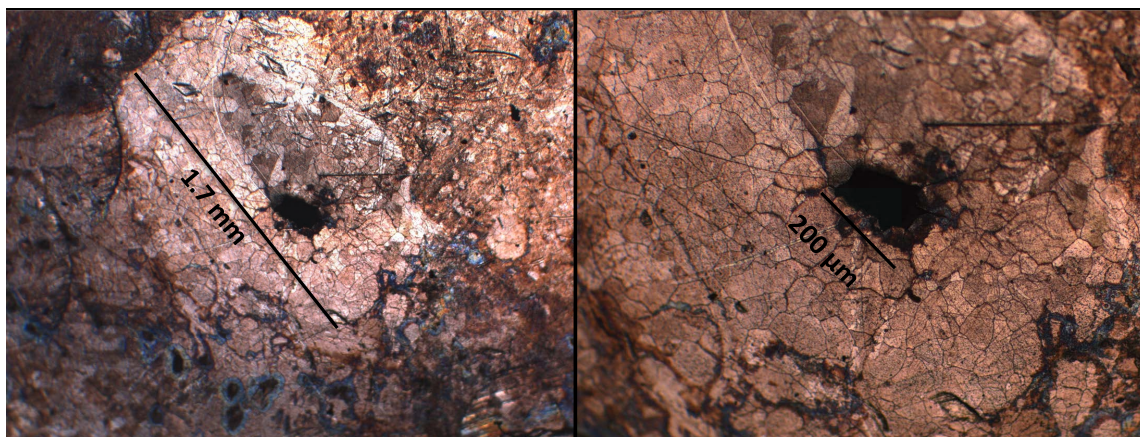
Figure 5.17: Left: 20x magnification of the pin hole on the beam side of the SCID sample. 1.7 mm bar indicates the overall beam irradiation area. Right: 50x magnification of the pin hole. 200 μm bar measures the length of the hole.

the beam size, due to its width being approximately that of the planned beam spot. The illuminated area is also the location of the larger grains, indicating increased heating. The image to the right in Figure 5.17 shows the increased grains as well as the 200 μm pin hole size. It can also be noted that the shape of the pin hole resembles the shape of the beam spot. The similar shape indicates that the beam's Gaussian distribution needs to be broadened in future experiments, as the inner portion of the irradiation region will have a much larger applied dose due to the increase fluence of particles in that region. The intercrystalline failure seen surrounding the pin hole is assumed to be the cause of the death/failure. The failure at the grain boundary can likely be attributed to beam heating and the stress applied to the sample as a result of the differential pressure between the salt side and the beam side of the sample.

Once the salt is fully dissolved from the inner side of the sample assembly, the sample is carefully removed from the knife edge using tube cutters. The blades of the cutters were placed in the small gap between the sample and the capsule, and the sample easily popped off of the knife edge. Again, no preparation was performed on the sample before optical imaging. The optical microscopy results can be found in Appendix B. During the optical microscopy process it is concluded that the grain size was stable through all corroded regions which did not see the beam. That said, substantial grain growth occurred in the irradiated area, particularly surrounding the failure region.
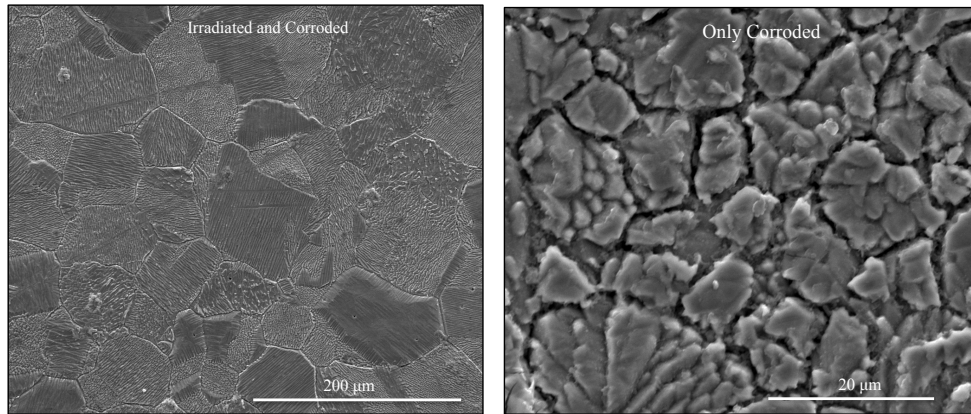
Figure 5.18: SEM micrographs of the beam affected region (left) and solely corroded region (right) of the SCID sample. Not the large grain size in the beam affect region, believed to be primarily due to excessive beam heating in that area.

Using scanning electron microscopy (SEM) and energy dispersive spectroscopy (EDS) a more careful investigation of the sample is made. A comparison of the beam affected area (irradiated) and the solely corroded regions of the sample is displayed in Figure 5.18. In the beam affected area (left) twinning and two distinct

grain orientations become obvious. The solely corroded region (right) displays the characteristic 10-20 μm size gains which are exposed due to molten salt corrosion. The grain growth falls off rapidly at the edge of the beam affected area as evident in Figure 5.19. Taking a closer look at the grain boundaries of the beam affected area
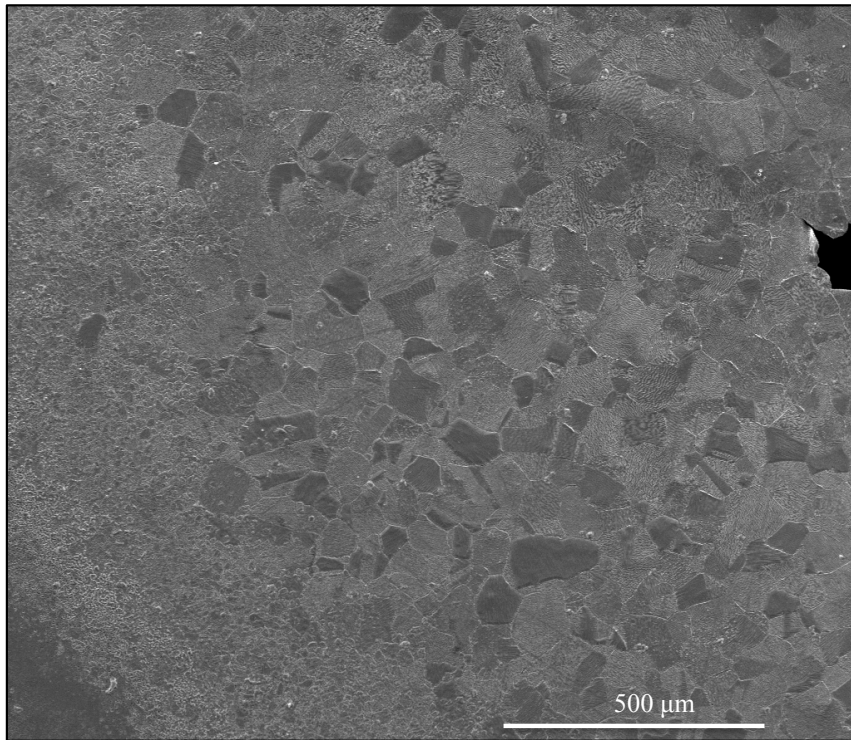
Figure 5.19: Micrograph of the beam affected radius. To the far right of the image is the hole in the sample and towards the left, the grains return to their 10-15 μm size.

away from the failure, we see distinct grain boundary etching. Figure 5.20 shows high magnification of the grain boundary effects in the beam spot on the salt side of the sample.

Using EDS, Ce and Cl were both found in a line scan across the grain. Figure
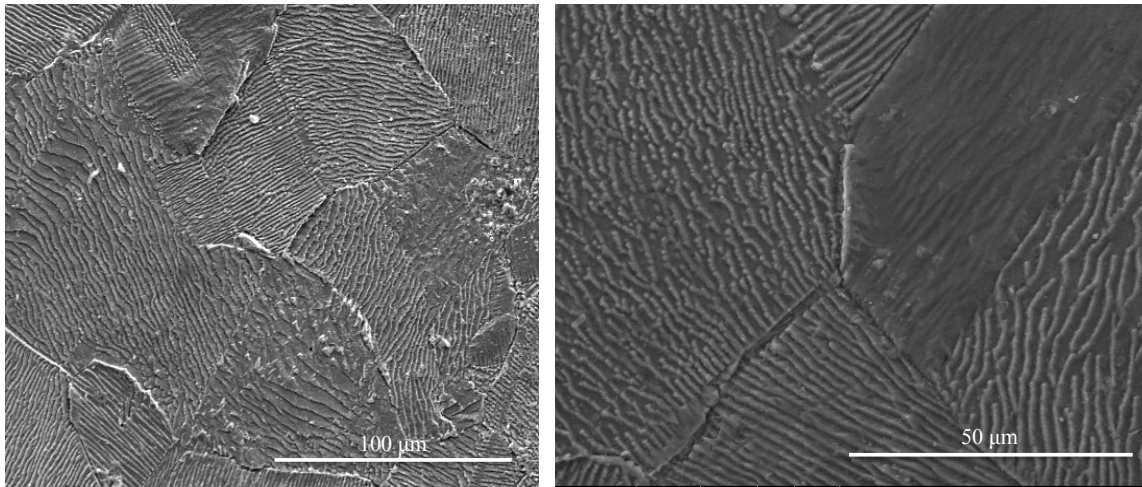
Figure 5.20: Micrographs of the grain structure in the beam affected region. Ridged grains (left) thought to be due to faceting. Twinning right as seen by the difference of grain orientation/texture.

5.21 plots the increase in Ce and Cl and decrease of Ni as the beam scans across the grain boundary selected in the sample. The next question to ask is how deep the grain boundary penetration is in this region. Focused Ion Beam (FIB) milling paired with SEM and STEM can answer this question.

A grain boundary is isolated and trenched. Then the portion straddling the grain boundary is lifted out, and we can see that the actual grain boundary penetration is on the order of 0.5 μm; see Figure 5.22

Unlike the 100 hour corrosion sample, no plating is observed in this particular sampling location. EDS across the boundary shows that it is a nickel-nickel grain boundary. There are no other elements present. The white layer at the top of the boundary is the Pt which is plated onto the surface to help facilitate the liftout process. The reasons for a lack of plating could be a very uniform surface in this region of the sample. Likewise, it could be that we have been unlucky and found a region which didn't experience plating. It is unlikely that the beam could have
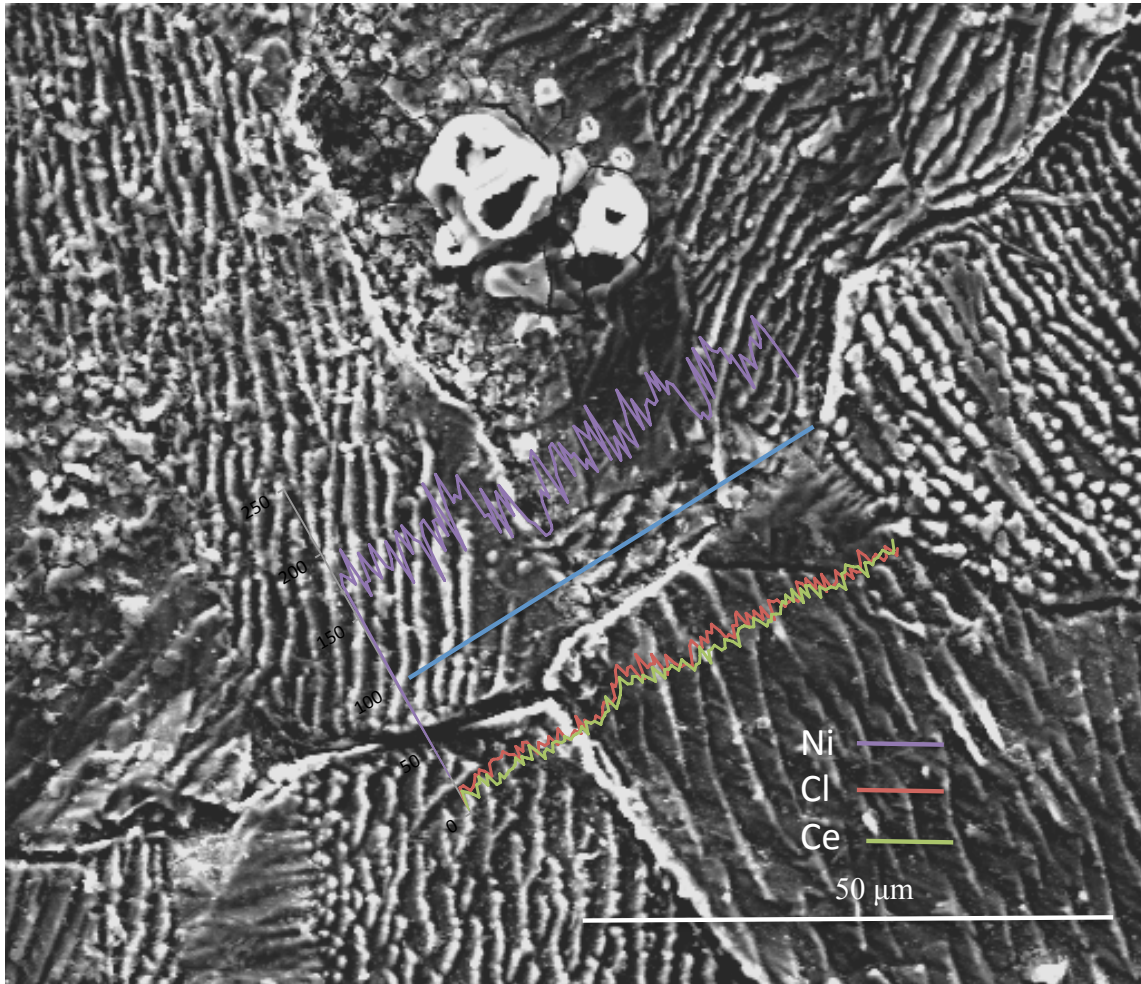
Figure 5.21: EDS line scan across a grain boundary displaying decreased Ni counts and increased Cl and Ce counts on the boundary itself.

inhibited the nickel plating as the sample was only exposed to it for a short amount of time. However, since the plating is an electrolytic process, charging of the nickel sample will surely effect the deposition process.

The significant grain growth leading to intercrystalline failure is decidedly the cause of the failure of the SCID sample. There are a limited number of physical mechanisms which can lead to this failure. The temperature limit of the Ni 200/201 dual certified alloy is approved for service up to 677 °C. Ni 201 has a lower carbon
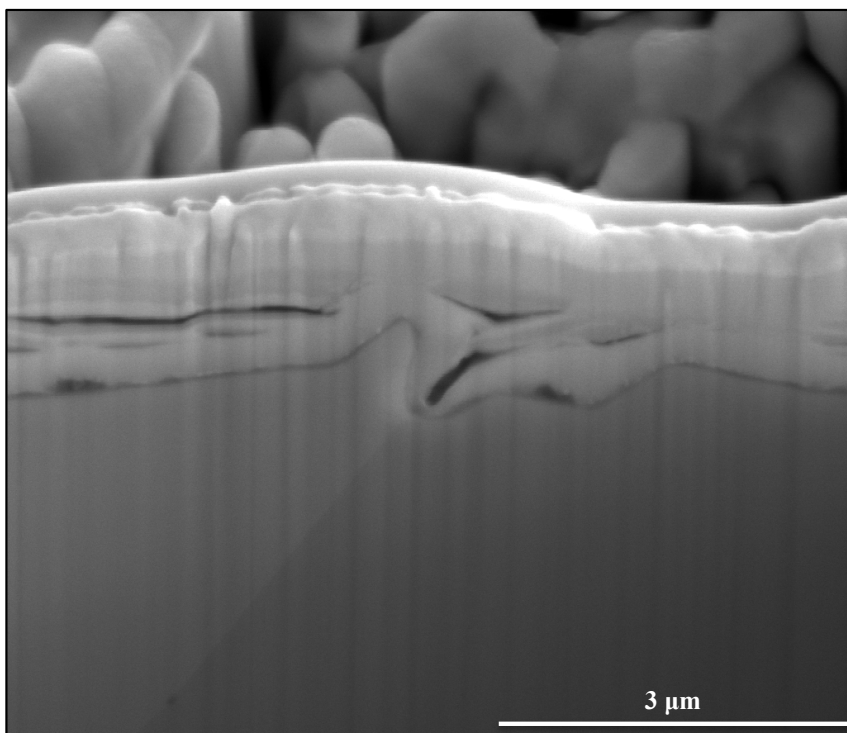
Figure 5.22: Grain boundary penetration as revealed via FIB.

content than Ni 200, minimizing graphitization at high temperature. With the dual certified material, this alloy can provide both the high temperature strength of Ni 201 as well as the ductility of Ni 200. However, if the temperature of the sample exceeded this service temperature, all bets are off.

Monitoring the sample surface temperature can be challenging. A thermocouple was placed in a gas tube in the vapor head above the salt in the capsule, approximately a centimeter away from the sample. While the beam was ramping up in current, the thermocouple saw an increase in temperature of only 5-10 °C. The grain boundary growth and the lack of significant temperature increase in the capsule as the beam current increases indicates that the salt did not take away the heat induced in the sample.

Studying the literature for data on grain growth in commercially pure nickel at high temperatures, a relatively recent article plots the grain growth as a function of temperature. Randle (2008) states that the average grain size at 900 °C is 70 μm. The study also identifies rapid grain growth between 900 - 1000 °C; the average grain size at 1000 °C is stated to be close to 140 μm.[67] Therefore the thermal model and the literature data both point to a maximum temperature in the irradiated region reaching upwards of 950 °C.

Thermal modeling of the system assuming the thermal conductivity is that of NaCl concludes that the temperature of the sample rose to 920 °C. The thermal model was made by Dr. Akhdiyor Sattarov using COMSOL Multi Physics. A snapshot of the model can be seen in Figure 5.23.[†]

There are two probable causes of the temperature increase. The first, the 0.79 W/m-K thermal conductivity of NaCl is not enough to take away the heat from the sample surface. The second: while ramping the beam there is reason to believe that the center of the beam was much more focused, and therefore the power density in the center of the beam spot would be much greater. Suggested improvements to mitigate these effects are proposed in the Future Work section of Section 6 in this dissertation.

It should be noted that during an ion beam irradiation damage experiment, the beam affected region can experience grain growth due to irradiation.[68] While this first test does not provide an ideal sample to observe this affect, since heating from the beam is the primary cause for grain growth, in future tests I expect to see grain growth due to irradiation. Previous experiments on steels have observed this effect.[69]

[†]Special acknowledgment to Dr. Akhdiyor I. Sattarov, Ph.D. for the thermal modeling using COMSOL Multi Physics.
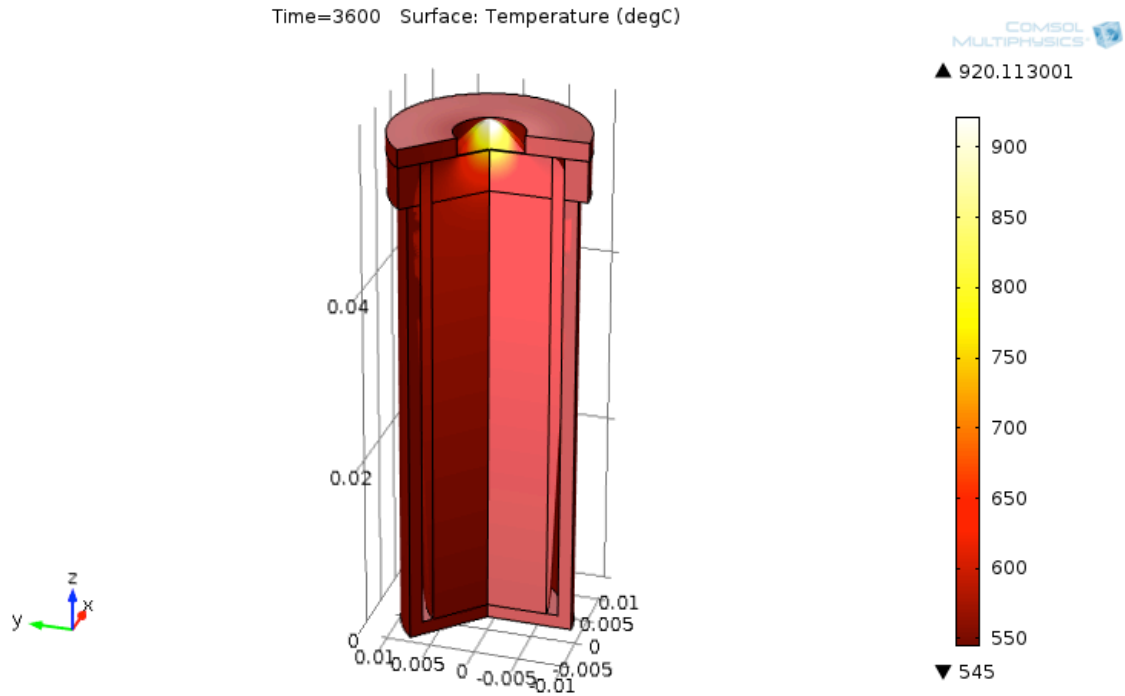
Figure 5.23: Thermal model to estimate the peak temperature of the sample during beam irradiation. The model indicates that the peak temperature of the sample reached 920 °C at the center of the beam and this heat was not dissipated by either the Ni or salt.

Furthermore, stress corrosion cracking can be the cause of failure in these systems.[70] Irradiation induced stress corrosion cracking is very well documented[71] and embrittlement is a hypothesized cause for crack formation at grain boundaries. Due to nickel's propensity for embrittlement, as discussed in Section 2 of this dissertation, crack inducing mechanisms such as hydrogen and helium accumulation at grain boundaries as well as dislocation loops leading to increased hardness are expected to be observed in future irradiation damage and corrosion experiments employing nickel.

6. CONCLUSIONS AND FUTURE WORK

6.1 Conclusions

Computational modeling and experimental investigations to explore the physical, transport, and corrosive properties of candidate host salts for the ADAM project have been investigated. Molecular dynamics provides the frame work for computational analysis of ionic liquids. Using the polarizable ion model (PIM) the density and heat capacity of candidate fuel salt systems containing UCl_3, $PuCl_3$, and various lanthanide compounds have been modeled. La interaction potential parameters have successfully been utilized as surrogates for the Pu system. Employing the La ion, which has a similar ionic radius to Pu, physical and transport properties consistent with experimental results in other actinide systems have been modeled.

Experimentally, an improved salt drying technique has been developed for 3^+ 4^+ ions (e.g. Ce). A significant (over 100 hour) reduction in drying time has now been achieved, and complete dehydration of H_2O contaminated salts has been achieved. Vacuum conditions in the mid 10^{-5} Torr are utilized for 5-7 hours at 55 °C. It is shown here that these conditions can succussfully remove trace H_2O from $CeCl_3$ partially hydrated salts.

New accurate and repeatable data been acquired using differential scanning calorimetry to map the liquidus-solidus phase diagram of the $NaCl$-UCl_3 system. The new liquidus curve on the NaCl-rich portion of the binary phase diagram more accurately represents the typical parabolic behavior of these phase systems. The significant liquidus correction to the NaCl-rich side of the binary phase diagram provides new insight to the allowable operating temperatures for U containing molten salt reactors. With this new data, the reactor systems can more accurately be modeled to predict

performance of the power producing system. A similar correction is anticipated in the NaCl-PuCl$_3$ containing system based on similar curvature on the NaCl-rich liquidus curve. The Pu containing system is of the utmost importance to a molten salt reactor which is configured as a transuranic burner, such as ADAM. The NaCl-UCl$_3$-CeCl$_3$ liquidus surface has been mapped experimentally for the first time. In this diagram, two low melt regions are identified as candidate surrogate fuel salt compositions.

Material transport of Ni in a NaCl-CeCl$_3$ salt at 550 °C system has been identified and characterized using SEM, FIB, and EDS. Material deposition is observed within a corroded grain boundary, providing evidence of conformal deposition. The evidence of such deposition suggests the potential for a new mechanism for dynamic stabilization against corrosion.

Finally, in a simultaneous ion beam irradiation damage and molten salt corrosion experiment, heat transport from the metal-salt interface proves to be the limiting experimental design constraint. The heat capacity and thermal conductivity of candidate chloride fuel salts are too poor to enable heat dissipation away from the region of study during testing to appreciable doses, (more than 5 DPA). The poor heat transfer properties of the surrogate fuel salt causes over heating of the sample surface, which leads to intercrystalline failure in the beam affected region.

6.2   Future Work

6.2.1   Chloride Salt Phase Diagram Investigations

Continued work at LANL's Fuels Research Lab will include a design to perform molten salt thermal conductivity measurements using Laser Flash Analysis. Also, as the Plutonium Facility continues to resume operations, the PuCl$_3$ containing systems will be investigated. While access to both the scientific staff and equipment in this

facility will be limited, we will be able to test points in the vicinity of our $CeCl_3$ data to assess cerium's use as a surrogate. Lastly, a sealed Ni crucible design will be pursued to enable accurate heat capacity measurements of these salt systems. A new Al_2O_3 heat capacity head for the DSC in the FRL will allow us to remove the thermal barrier constrains discussed in Section 5 of this dissertation, and possible reactions between the crucibles and the measurement head will be eliminated.

6.3   Static Salt Corrosion Testing

In review of the observations and data obtained to date, 24 hour molten salt corrosion tests could prove to be beneficial if a number of changes are made to the sample preparation and analysis techniques. First and foremost, impurities must be minimized. As stated in a recent publication, impurity driven corrosion can dominate the corrosion kinetics in molten salt for the first several weeks of exposure. Therefore, the purchase of high purity materials is ideal, if available. If not, HCl purges, drying lines, and other purification techniques must be employed, and analysis of the salt via XRD needs to confirm the purity of the salt system.

Future work for corrosion testing includes developing an understanding of the nickel plated layer observed in the 100 hour corrosion test. The sample will be segmented in three more locations to assess the variation of plating across the surface.

Similar analysis will be performed when the irradiation damage and corrosion experiment resumes. Also, samples are being designed at LANL in the FRL to have strategically varied thicknesses across the sample surface. A challenge here will be to ensure a sufficient surface finish to visualize the grain boundary attach in the preferentially corroded regions. Lastly, dynamic testing is necessary to predict the effect of erosion-corrosion on the ADAM core.

6.4 Salt Corrosion and Irradiation Damage

Multiple research teams have been involved in the design, execution, and analysis of the simultaneous irradiation damage and salt corrosion experiment. There is a willingness on all sides to make this work, and we would like to run again, as it is the first experiment of its kind using molten salts.

In order to successfully test the sample using simultaneous corrosion and irradiation damage, the heat must be taken away from the sample surface and the beam spread. To most efficiently remove the heat, a small molten salt pump could constantly refresh the salt volume. The pump configuration would require not only a very specialized pump but also a reservoir of salt.

Spreading the beam and therefore creating a larger irradiation area is a more complicated endeavor, if attempting to achieve appreciable damage in the sample. A spread beam results in a lower flux of particles through the sample, therefore either decreasing the total DPA achieved in the experiment or increasing the run time significantly. A thermal model a 3 mm x 3 mm spot size, as opposed to the 2 mm x 2 mm spot used in the first experiment, led to only a 10% temperature decrease. The same change would result in a reduction from a total dose in 60 hours of 5.2 DPA, with 2 mm x 2 mm and 1.3 μA (the failure current at 5.8 MeV for the sample 1), to 2.3 DPA with a 3 mm x 3 mm spot size under the same beam and sample profile.

Decreasing the current will also lower the beam power, however this approach likewise leads to either an increase in run time or decrease in dose. A thermally acceptable scenario is modeled with a 1 mm x 1 mm spot size and 0.325 μA current. Unfortunately, in 72 hours this configuration deposits only 0.69 DPA, again assuming the same sample thickness and beam energy as initial SCID parameters.

The thermal complications imply only two reasonably foreseeable configurations: 1) actively circulating the salt with a pump or 2) employ a salt with a higher heat capacity than the surrogate fuel salt. Addressing the second option since it is more economical, LiCl-KCl has a higher heat capacity, thermal conductivity, and more well known physical properties as functions of temperature. Comparatively, a spot size of 1 mm^2 and beam current of 0.325 μA leads to a 150 °C decrease in temperature from an NaCl-CeCl$_3$ system modeled with the same parameters. Nevertheless, a 1 mm x 1 mm spot size is very challenging to control on the Tandem, and most importantly, leaves very little room for post irradiation examination.

The most simple route to a rerun of this experiment is to aim for a lower dose and use LiCl-KCl as the salt. Running at 0.75 μA, 5.8 MeV with a 400 °C LiCl-KCl will have a maximum temperature of 607 °C. The dose after 72 hours is 3.6 DPA. The new experiment will allow us to use the last back-up sample previously made for SCID 1, and new sealing techniques can be employed, since the Ni-Ni weld failed in SCID 1. Introducing a pump into this very complicated experiment will need to come after a proper sealing mechanism is proven in a non-flowing system. Thermal analysis indicates that to achieve the initial SCID parameters a flow rate of close to 1 m/s will be necessary to keep the window temperature below the material limits. The sample thickness of the SCID 2 sample will be measured using the proton transmission test described in Section 4 of this dissertation. LiCl-KCl is an off the shelf anhydrous salt, and the melt point and purity will be verified using DSC. If this proves a successful configuration, 5 DPA can be delivered in just over 3 days of beam time.

REFERENCES

[1] World Nuclear Association. *Nuclear Power in the World Today*, April 2014, Retrieved: August 12, 2014 from http://www.world-nuclear.org/info/Current-and-Fugture-Generation/Nuclear-Power-in-the-World-Today/.

[2] LH Hamilton, B Scowcroft, MH Ayers, VA Bailey, A Carnesale, PV Domenici, S Eisenhower, C Hagel, J Lash, AM Macfarlane, et al. Blue ribbon commission on america's nuclear future: Report to the secretary of energy. *US Department of Energy, Washington, DC*, 2012.

[3] Peter McIntyre, Saeed Assadi, Karie Badgley, William Baker, Justin Comeaux, James Gerity, Joshua Kellams, Al McInturff, Nathaniel Pogue, Supathorn Phongikaroon, Akhdiyor Sattarov, Michael Simpson, Elizabeth Sooby, and Pavel Tsvetkov. Accelerator-driven subcritical fission in molten salt core: Closing the nuclear fuel cycle for green nuclear energy. *AIP Conference Proceedings*, 1525(1), 2013.

[4] F Carminati, C Roche, Juan Antonio Rubio, Carlo Rubbia, Jean Pierre Charles Revol, and Robert Klapisch. "An Energy Amplifier for Cleaner and Inexhaustible Nuclear Energy Production Driven by a Particle Beam Accelerator", Technical Report, P00019698, 1993.

[5] S Andriamonje, A Angelopoulos, A Apostolakis, F Attale, L Brillard, S Buono, J Calero, F Carminati, F Casagrande, P Cennini, et al, Experimental determination of the energy generated in nuclear cascades by a high energy beam. *Physics Letters B*, 348(3):697–709, 1995.

[6] M Seidel and PA Schmelzbach. Upgrade of the PSI Cyclotron Facility to 1.8 MW, *Proc. Cycl. and their Applications*, 2007.

[7] MW Rosenthal, PR Kasten, RB Briggs, et al. Molten salt reactors-history, status, and potential. *Nuclear Applications and Technology*, 8(2):107–117, 1970.

[8] Murray Rosenthal. "An account of oak ridge nation laboratory's thirteen nuclear reactors", Oakridge National Laboratory, TM-2009/181, March 2010.

[9] Kazuo Furukawa, Eduardo D Greaves, L Berrin Erbay, Miloslav Hron, and Yoshio Kato. New sustainable secure nuclear industry based on thorium molten-salt nuclear energy synergetics (thorims-nes). *Nuclear Power-Deployment, Operation and Sustainability*, 2011.

[10] Charles D Bowman. Once-through thermal-spectrum accelerator-driven light water reactor waste destruction without reprocessing: Special on accelerator applications. *Nuclear Technology*, 132(1):66–93, 2000.

[11] V Berthou, I Slessarev, and M Salvatores. Proposal of a molten salt system for long term energy production. *Advanced Reactors with Innovative Fuels: Second Workshop Proceedings*, Chester, United Kingdom, 22-24 October 2001, page 401.

[12] L Mathieu, D Heuer, E Merle-Lucotte, R Brissot, C Le Brun, E Liatard, JM Loiseaux, O Méplan, A Nuttin, D Lecarpentier, et al, Possible configurations for the thorium molten salt reactor and advantages of the fast nonmoderated version, *Nuclear Science & Engineering*, 161(1):78, 2009.

[13] D Lecarpentier, C Garzenne, J Vergnes, H Mouney, and M Delpech, Amster: A molten-salt reactor concept generating its own ^{233}U and incinerating transuranium

elements, *Advanced Reactors with Innovative Fuels: Second Workshop Proceedings*, Chester, United Kingdom, 22-24 October 2001, page 381.

[14] Miloslav Hron. Project sphinx spent hot fuel incinerator by neutron flux (the development of a new reactor concept with liquid fuel based on molten fluorides). *Progress in Nuclear Energy*, 47(1):347–353, 2005.

[15] Kazuo Furukawa, Yoshio Kato, and Sergey E Chigrinov. Plutonium (tru) transmutation and ^{233}U production by single-fluid type accelerator molten-salt breeder (AMSB), *AIP Conference Proceedings*, pages 745–751, IOP Institute of Physics Publishing, 1995.

[16] Alexandre Mourogov and Pavel M Bokov. Potentialities of the fast spectrum molten salt reactor concept: Rebus-3700. *Energy Conversion and Management*, 47(17):2761–2771, 2006.

[17] Ondrej Beneš. *Thermodynamics of Molten Salts for Nuclear Applications*, JRC Technical Notes, 2008.

[18] T Takizuka, T Nishida, T Sasa, H Takada, and M Mizumoto. Studies on accelerator-driven transmutation at JAERI, *Proc. 4th Intl. Information Exchange Meeting*, page 161, 1996.

[19] Gary S. Was. *Fundamentals of Radiation Materials Science: Metals and Alloys*. Springer, 2007.

[20] L.K Mansur, A.F Rowcliffe, R.K Nanstad, S.J Zinkle, W.R Corwin, and R.E Stoller. Materials needs for fusion, generation {IV} fission reactors and spallation neutron sources - similarities and differences. *Journal of Nuclear Materials*, 329-333, Part A(0):166 – 172, 2004.

[21] V.A. Kazakov, H.-C. Tsai, V.P. Chakin, F.W. Wiffen, A.F. Rowcliffe, D.L. Smith, A.E. Rusanov, A.A. Teikovtsev, N.V. Markina, and L.R. Greenwood. Experience in irradiation testing of low-activation structural materials in fast reactor bor-60. *Journal of Nuclear Materials*, 258-263, Part 2(0):1458 – 1465, 1998.

[22] G.S Bauer, M Salvatores, and G Heusener. Megapie, a 1 {MW} pilot experiment for a liquid metal spallation target. *Journal of Nuclear Materials*, 296(1-3):17 – 33, 2001.

[23] R.S. Nelson and D.J. Mazey. Void formation in stainless steel during charged particle irradiation at elevated temperatures, *Radiation Damage in Reactor Materials*, (2), 157–163.

[24] Go Lo Kulcinski, JJ Laidler, and DG Doran. Simulation of high fluence fast neutron damage with heavy ion bombardment. *Radiation Effects*, 7(3-4):195–202, 1971.

[25] GL Kulcinski, AB Wittkower, and G Ryding. Use of heavy ions from a tandem accelerator to simulate high fluence, fast neutron damage in metals. *Nuclear Instruments and Methods*, 94(2):365–375, 1971.

[26] MJ Norgett, MT Robinson, and IM Torrens. A proposed method of calculating displacement dose rates. *Nuclear Engineering and Design*, 33(1):50–54, 1975.

[27] Nikolai I Budylkin, Elena G Mironova, VM Chernov, VA Krasnoselov, SI Porollo, and Francis A Garner. Neutron-induced swelling and embrittlement of pure iron and pure nickel irradiated in the bn-350 and bor-60 fast reactors. *Journal of Nuclear Materials*, 375(3):359–364, 2008.

[28] Thomas M Angeliu, John T Ward, and Jonathan K Witter. Assessing the effects of radiation damage on Ni-base alloys for the prometheus space reactor system. *Journal of Nuclear Materials*, 366(1):223–237, 2007.

[29] M.B. Chadwick, M. Herman, P. ObloÅŸinskÃœ, M.E. Dunn, Y. Danon, A.C. Kahler, D.L. Smith, B. Pritychenko, G. Arbanas, R. Arcilla, R. Brewer, D.A. Brown, R. Capote, A.D. Carlson, Y.S. Cho, H. Derrien, K. Guber, G.M. Hale, S. Hoblit, S. Holloway, T.D. Johnson, T. Kawano, B.C. Kiedrowski, H. Kim, S. Kunieda, N.M. Larson, L. Leal, J.P. Lestone, R.C. Little, E.A. McCutchan, R.E. MacFarlane, M. MacInnes, C.M. Mattoon, R.D. McKnight, S.F. Mughabghab, G.P.A. Nobre, G. Palmiotti, A. Palumbo, M.T. Pigni, V.G. Pronyaev, R.O. Sayer, A.A. Sonzogni, N.C. Summers, P. Talou, I.J. Thompson, A. Trkov, R.L. Vogt, S.C. van der Marck, A. Wallner, M.C. White, D. Wiarda, and P.G. Young. Endf/b-vii.1 nuclear data for science and technology: Cross sections, covariances, fission product yields and decay data. *Nuclear Data Sheets*, 112(12):2887 – 2996, 2011. Special Issue on ENDF/B-VII.1 Library.

[30] FA Garner. "Void Swelling and Irradiation Creep in Light Water Reactor Environments," *Philip G. Tipping (Ed.)*, pages 308–365, 2010.

[31] JR Keiser. "Compatibility studies of potential molten-salt breeder reactor materials in molten fluoride salts", Technical Report, Oak Ridge National Lab., Tenn.(USA), 1977.

[32] JW Koger. "Alloy compatibility with LiF-BeF_2 salts containing ThF_4 and UF_4", Technical Report, Oak Ridge National Lab., Tenn.(USA), 1972.

[33] Jackson Harvey DeVan, "Effect of alloying additions on corrosion behavior of nickel–molybdenum alloys in fused fluoride mixtures", Technical report, Oak Ridge National Lab., Tenn., 1969.

[34] C Edeleanu and R Littlewood. Thermodynamics of corrosion in fused chlorides. *Electrochimica Acta*, 3(3):195–207, 1960.

[35] Frederic Lantelme and Henri Groult. *Molten Salts Chemistry: From Lab to Applications.* Newnes, 2013.

[36] Luke Christopher Olson. Materials corrosion in molten lithium fluoride-sodium fluoride-potassium fluoride eutectic salt. *University of Wisconsin at Madison Dissertation*, 2009.

[37] Yuji Hosoya, Takayuki Terai, Toshiaki Yoneoka, and Satoru Tanaka. Compatibility of structural materials with molten chloride mixture at high temperature. *Journal of Nuclear Materials*, 248(0):348 – 353, 1997.

[38] S Assadi, C Collins, J Comeaux, K Damborsky, J Kellams, F Lu, P McIntyre, K Melconian, N Pogue, M Salanne, et al. Accelerator-driven subcritical fission to destroy transuranics and close the nuclear fuel cycle, *AIP Conference Proceedings* 1525(1), 2013

[39] N. Pogue, S. Assadi, K. Badgley, J. Comeaux, J. Kellams, A. McInturff, P. McIntyre, and A. Sattarov. A strong-focusing 800 mev cyclotron for high-current applications. *AIP Conference Proceedings*, 1525(1), 2013.

[40] DE Holcomb, GF Flanagan, BW Patton, JC Gehin, RL Howard, and TJ Harrison. Fast spectrum molten salt reactor options. *ORNL/TM-2011/105*, 2011.

[41] O. Beneš and R.J.M. Konings. Thermodynamic evaluation of the NaCl-MgCl$_2$-UCl$_3$-PuCl$_3$ system. *Journal of Nuclear Materials*, 375(2):202 – 208, 2008.

[42] CF Baes Jr, JH Shaffer, and HF McDuffie. UO$_2$ and ZrO$_2$ behavior in molten fluorides. *Transactions of the American Nuclear Society (US)*, 6, 1963.

[43] M Wilson and PA Madden. Polarization effects in ionic systems from first principles. *Journal of Physics: Condensed Matter*, 5(17):2687, 1993.

[44] Paul A Madden and Mark Wilson. 'covalent effects in ionicsystems. *Chem. Soc. Rev.*, 25(5):339–350, 1996.

[45] Norikazu Ohtori, Mathieu Salanne, and Paul A Madden. Calculations of the thermal conductivities of ionic materials by simulation with polarizable interaction potentials. *The Journal of Chemical Physics*, 130(10):104507, 2009.

[46] Mathieu Salanne, Christian Simon, Pierre Turq, and Paul A Madden. Heat-transport properties of molten fluorides: determination from first-principles. *Journal of Fluorine Chemistry*, 130(1):38–44, 2009.

[47] Mathieu Salanne, Christian Simon, Pierre Turq, Robert J Heaton, and Paul A Madden. A first-principles description of liquid BeF$_2$ and its mixtures with LiF: Network formation in LiF-BeF$_2$. *The Journal of Physical Chemistry B*, 110(23):11461–11467, 2006.

[48] Mathieu Salanne, Christian Simon, Pierre Turq, and Paul A Madden. Calculation of activities of ions in molten salts with potential application to the pyroprocessing of nuclear waste. *The Journal of Physical Chemistry B*, 112(4):1177–1183, 2008.

[49] Y Okamoto, PA Madden, and K Minato. X-ray diffraction and molecular dynamics simulation studies of molten uranium chloride. *Journal of Nuclear Materials*, 344(1):109–114, 2005.

[50] Francis Hutchinson, Adrian J Rowley, Malcolm K Walters, Mark Wilson, Paul A Madden, Jonathan C Wasse, and Philip S Salmon. Structure of molten mcl3 systems from a polarizable ion simulation model. *The Journal of Chemical Physics*, 111(5):2028–2037, 1999.

[51] Yoshihiro Okamoto, Shinichi Suzuki, Hideaki Shiwaku, Atsushi Ikeda-Ohno, Tsuyoshi Yaita, and Paul A Madden. Local coordination about La3+ in molten LaCl$_3$ and its mixtures with alkali chlorides. *The Journal of Physical Chemistry A*, 114(13):4664–4671, 2010.

[52] VN Desyatnik, MP Vorobei, NN Kurbatov, IS Kalashnikov, and OV Siiba. Melting diagrams of ternary systems containing sodium and potassium chlorides, thorium tetrachloride, and plutonium trichloride. *Atomic Energy*, 38(3):219–221, 1975.

[53] Kazuhito Fukasawa, Akihiro Uehara, Takayuki Nagai, Nobuaki Sato, Toshiyuki Fujii, and Hajimu Yamana. Thermodynamic properties of trivalent lanthanide and actinide ions in molten mixtures of LiCl and KCl. *Journal of Nuclear Materials*, 424(1):17–22, 2012.

[54] John H Burns, JN Stevenson, and JR Peterson. Crystallographic studies of some transuranic trihalides: ^{239}PuCl$_3$, ^{244}CmBr$_3$, ^{249}BkBr$_3$ and ^{249}CfBr$_3$, *Journal of Inorganic and Nuclear Chemistry*, 37(3), 1975.

[55] Austin Alan Baty. *Molecular Dynamics Simulation of the Transport Properties of Molten Transuranic Chloride Salts*. Undergraduate Honors Thesis, Texas A&M University, 2013.

[56] James F Ziegler, Jochen P Biersack, and Matthias D Ziegler. *SRIM, The Stopping and Range of Ions in Matter*, SRIM Co., Chester, Maryland, 2008.

[57] R.E. Stoller, M.B. Toloczko, G.S. Was, A.G. Certain, S. Dwaraknath, and F.A. Garner. On the use of {SRIM} for computing radiation damage exposure. *Nuclear Instruments and Methods in Physics Research Section B: Beam Interactions with Materials and Atoms*, 310(0):75 – 80, 2013.

[58] Michael F Simpson, Tae-Sic Yoo, Robert W Benedict, Supathorn Phongikaroon, Steven Frank, Prateek Sachdev, and Kellianne Hartman. Strategic minimization of high level waste from pyroprocessing of spent nuclear fuel. *Proceedings of Global 2007*, page 1394, 2007.

[59] BR Westphal, KJ Bateman, and SD Herrmann. Top ten reasons for deox as a front end to pyroprocessing. *Transactions of the American Nuclear Society*, 97:71, 2007.

[60] S. D. Herrmann, S. X. Li, M. F. Simpson, and S. Phongikaroon. Electrolytic reduction of spent nuclear oxide fuel as part of an integral process to separate and recover actinides from fission products. *Separation Science and Technology*, 41(10):1965–1983, 2006.

[61] Vladimir Dimitrov, Kalina Kostova, and Miroslav Genov. Anhydrous cerium(iii) chloride - effect of the drying process on activity and efficiency. *Tetrahedron Letters*, 37(37):6787 – 6790, 1996.

[62] Toni Y. Gutknecht and Guy L. Fredrickson. *Thermal Characterization of Molten Salt Systems*, INL/EXT-11-23511, September 2011.

[63] Staffan Qvist, Alan Michael Bolind, Peter Hosemann, Yongqiang Wang, Joseph Tesmer, Magdalena Serrano De Caro, and Mark Bourke. Capability demonstration of simultaneous proton beam irradiation during exposure to molten lead–bismuth eutectic for HT-9 steel. *Nuclear Instruments and Methods in Physics Research Section A: Accelerators, Spectrometers, Detectors and Associated Equipment*, 698:98–105, 2013.

[64] Mieczysław Taube. Fast reactors using molten chloride salts as fuel. Technical report, Eidgenoessisches Inst. fuer Reaktorforschung, Wuerenlingen (Switzerland), 1978.

[65] Christopher Bale. *FactSage*, "Fact Salt Phase Diagrams", Retrieved on July 8, 2014 from www.crct.polymtl.ca/fact/documentation/FTsalt/.

[66] SP Lynch, DP Edwards, RB Nethercott, and JL Davidson. Failure of nickel-aluminum-bronze hydraulic coupling, with comments on general procedures for failure analysis. *Practical Failure Analysis*, 2(6):50–61.

[67] V. Randle, P.R. Rios, and Y. Hu. Grain growth and twinning in nickel. *Scripta Materialia*, 58(2):130 – 133, 2008.

[68] CW Allen and LE Rehn, "Irradiation-induced grain growth", *Proceedings of Beam-Solid Interactions, Physical Phenomena*, 22(17), 1990.

[69] S.M Bruemmer, E.P Simonen, P.M Scott, P.L Andresen, G.S Was, and J.L Nelson, Radiation-induced material changes and susceptibility to intergranular failure of light-water-reactor core internals. *Journal of Nuclear Materials*, 274(3):299 – 314, 1999.

[70] R.B. Rebak. "Stress corrosion cracking (scc) of nickel-based alloys", V.S. Raja and Tetsuo Shoji, editors, *Stress Corrosion Cracking*, Woodhead Publishing Series in Metals and Surface Engineering, pages 273 – 306. Woodhead Publishing, 2011.

[71] G.S. Was and P.L. Andresen. "Irradiation assisted corrosion and stress corrosion cracking (iac/iascc) in nuclear reactor systems and components". *Nuclear Reactor Systems and Components*, Woodhead Publishing Series in Energy, pages 131-185, Woodhead Publishing, 2012.

[72] Debbie Davy. Nickel vapor deposition technology. *Rapid Tooling: Technologies and Industrial Applications*, page 145, CRC Press, 2000.

APPENDIX A.   CVD NICKEL INVESTIGATION

Section 4 mentions a material which is gown via nickel vapor deposition (NVD). The NVD product is proposed for use as a vessel liner for the ADAM project. Conceptually, a layer of 1/4" thick nickel can be deposited onto a Hastelloy-N substrate to act as a protective, pure nickel layer. As discussed in depth in Section 1, corrosion in molten salt can be driven electrodynamically by the potential differences in alloying elements in a material. Also, the least noble metal can form a chloride and then lead to impurity driven corrosion. The pure nickel layer deposited on the Hastelloy-N mandrel can limit the process.

Weber Manufactuing in Ontario, Canada utilizes a carbonyl nickel process to deposit nickel onto aluminum mandrels. A diagram of this process taken from Davy (2000) depicts the typical NVD deposition process;[72] see Figure A.1. Weber states that their deposition rate is on overage 0.010"/hr.

A microstructure investigation of this material is taken on at ARL. The micrographs show evidence of typical CVD Ni phenomina, such as columnar grain growth
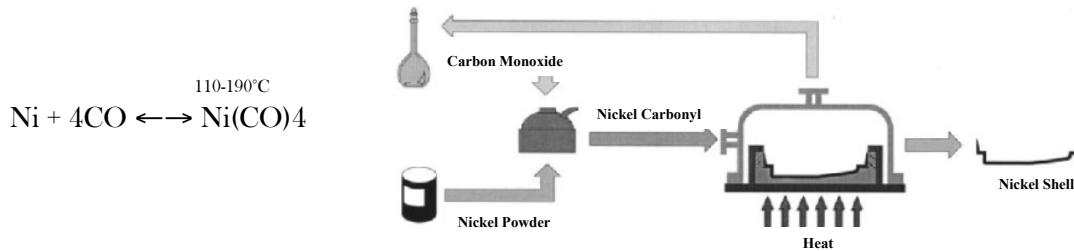

$$\text{Ni} + 4\text{CO} \longleftrightarrow \text{Ni(CO)}4$$

110-190°C

Carbon Monoxide

Nickel Carbonyl

Nickel Powder

Heat

Nickel Shell

Figure A.1: The nickel vapor deposition process begins with reacting a high purity nickel powder with carbon monoxide gass to form Ni(CO)_4. the carbonyl nickel gas is then transfered to a deposition chamber. The deposition substrate or mandrel is held at the appropriate temperature to dissociate the Ni from the carbonyl gas, resulting in a pure nickel shell.[72]

135

in the vertical deposition direction, twinning of nickel grains, and amorphous Ni remaining from un-nucleated nickel grains. Figure A.2 displays SEM micrographs taken by me of the substrate side of a 1/4" nickel plate received from Weber. From
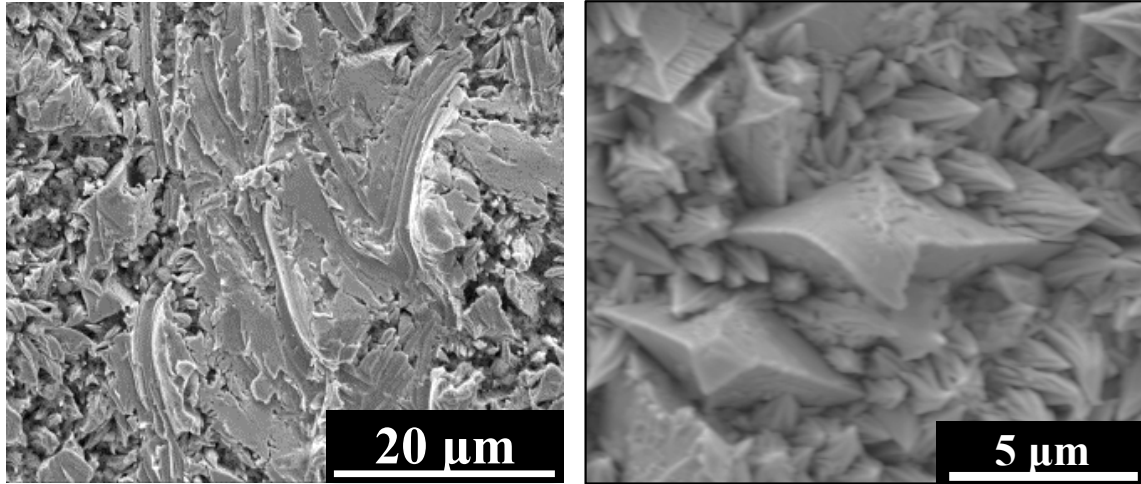

Figure A.2: These two SEM micrographs display the substrate/mandrel side of a 1/4" NVD plate received by ARL. The image to the left shows a 20 μm scale bar and the smearing of material is amorphous nickel which did not nucleate grains on the surface. The right image shows individual grains grown from the substrate. The bending of the end of the grains is assumed to be from the material removal from the aluminum substrate.

these micrographs we see that some of the nickel deposited does not nucleate grains, as displayed by the smearing effect. Also, the grains grow away from the surface, as seen in the right image in Figure A.2. Figure A.3 displays a transmission electron micrograph I obtained of twinning in the grains, as well as the tendency towards forming triple point grain boundaries.

In the microstructure investigation, analysis of the grain orientation and size is performed by Feng Lu, Ph.D., a post doctoral fellow in the ARL group. He found
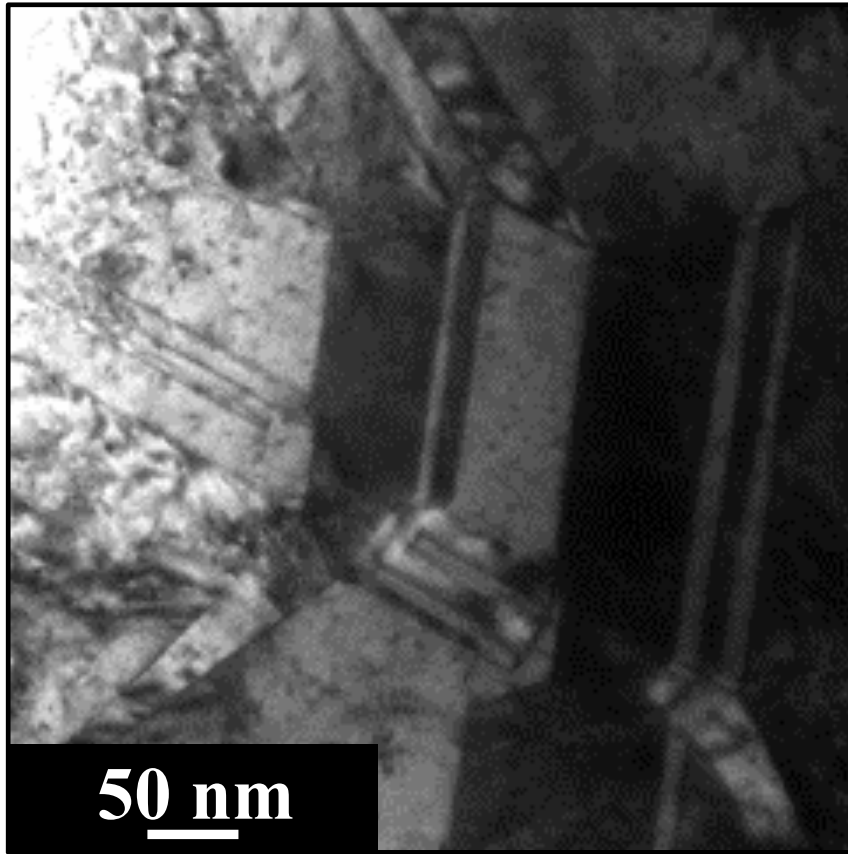
Figure A.3: Transmission electron microscope (TEM) micrograph taken of a top-down section of the NVD product. Visible are twinned grains and triple point grain boundaries.

small pin holes in the grain structure. After heat treatments, we saw that these holes grow and migrate to the triple point boundaries. SEM micrographs taken of the NVD material before and after a 700 °C heat treatment are displayed in Figure A.4

After consulting with Weber, they decided to use a dopant in their process, which produces finer grain size. The dopant appears to aid nucleation of small grains and help prevent the formation of pin holes within the microstructure. After analyzing the new material, while pin holes are still found in the raw material, the heat treated
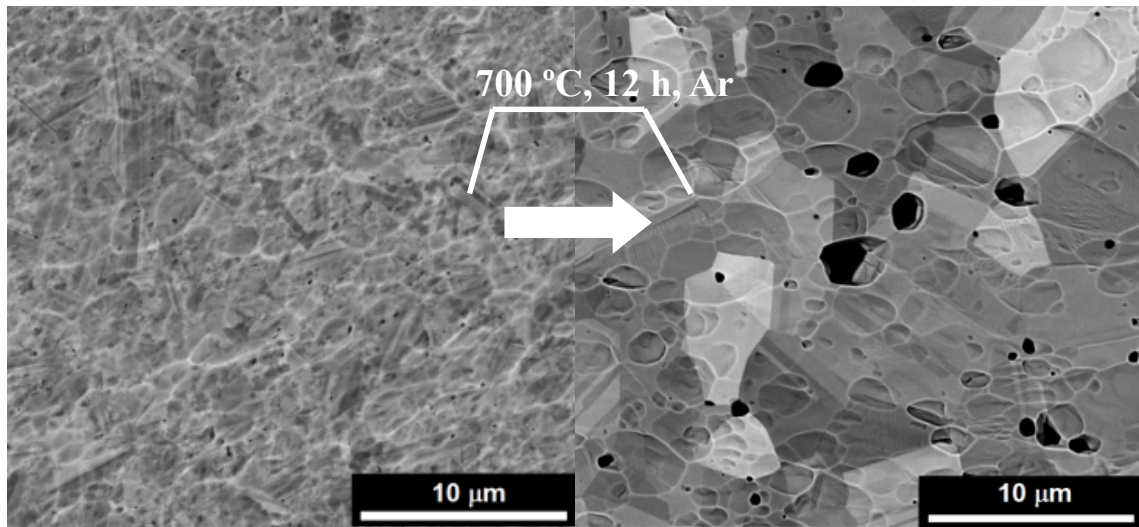
Figure A.4: The left micrograph is of a top-down cross section of the NVD material. Small pin holes are visible. After a 700 °C heat treatment, the pin holes grow significantly in size and accumulate at triple points in the grain boundaries (left). Images taken by Feng Lu, Ph.D at TAMU.

material shows to have a much lower hole density. Images of the material undoped (standard) and doped (New) after the same 700 °C, 12 hour anneal are shown in Figure A.5 Weber then prepared a one inch thick slab of doped NVD to use to machine the SCID 1 sample from. Upon sectioning of the material, large interstitial cracks were found. The concluding theory behind the cracks is a loss of sufficient thermal transport to the surface of the material during deposition inhibited grain nucleation in larger regions than previously seen. The lack of nucleation caused large columnar holds in the material. A micrograph of displaying one of the cracks relieved during sectioning is shown in Figure A.6, which can also be found in Section 4.
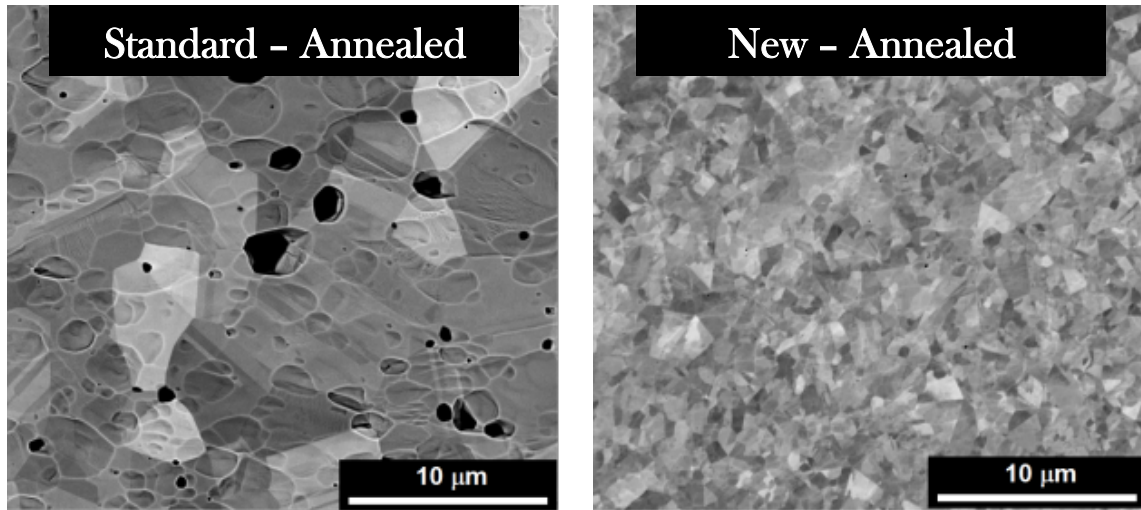
Figure A.5: The left images is the standard NVD material after a 700 ∘C, 12 hour anneal, and the right image is of the doped NVD material after the same anneal. The hold density is much smaller in the image to the right and the grain size finer. Images taken by Feng Lu, Ph.D at TAMU.
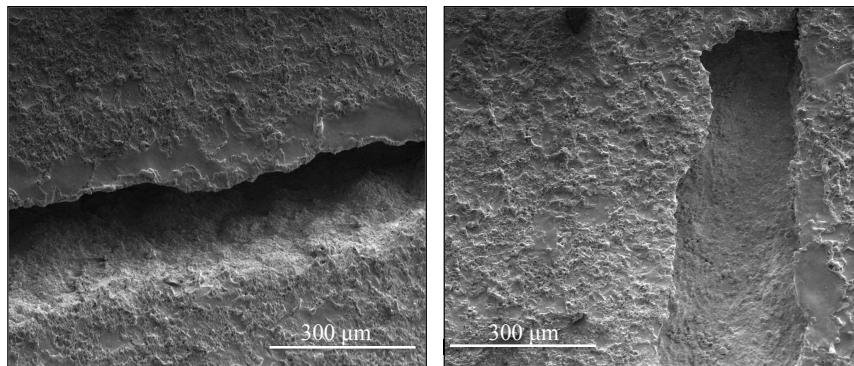

Figure A.6: Large crack found in 1" thick NVD nickel slab. The material around the crack appears to be amorphous, indicating a lack of grain nucleation in this region.

It is because of these large cracks found in the material that the NVD material is decided to be unreliable for the machining of the SCID 1 sample.

APPENDIX B.   OPTICAL MICROSCOPY OF THE SCID 1 SAMPLE

The area of the sample which was only corroded and neither stressed nor irradiated can be seen in Figure B.1.   The damage to the sample is characteristic of the
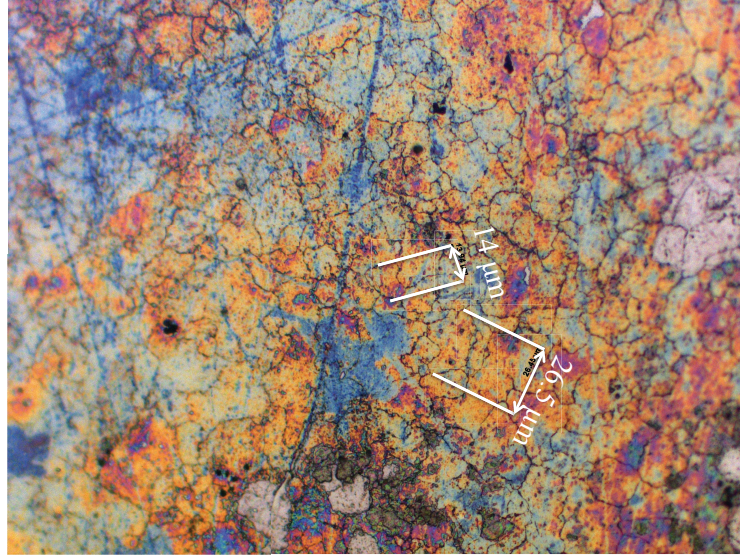

Figure B.1: The image displayed is a 10x magnification of the salt side of the SCID sample. The region imaged here is of the thicker area of the sample which is corroded, but has not been irradiation. Also, no appreciable stress is on this part of the sample as it is orders of magnitude thicker than the thinned, irradiation sample area.

100 hour corrosion test, in that there is no significant grain growth and the grain boundaries are lightly etched. Here we see the average grain size is 15-20 μm. The area of the sample which is thinned to 90 μm is the only area assumed to be under appreciable stress during the experiment. In the thinned region there is also an area which did not see any beam. The thinned, non irradiated area therefore has undergone both stress and corrosion and is displayed in Figure B.2. The average grain size
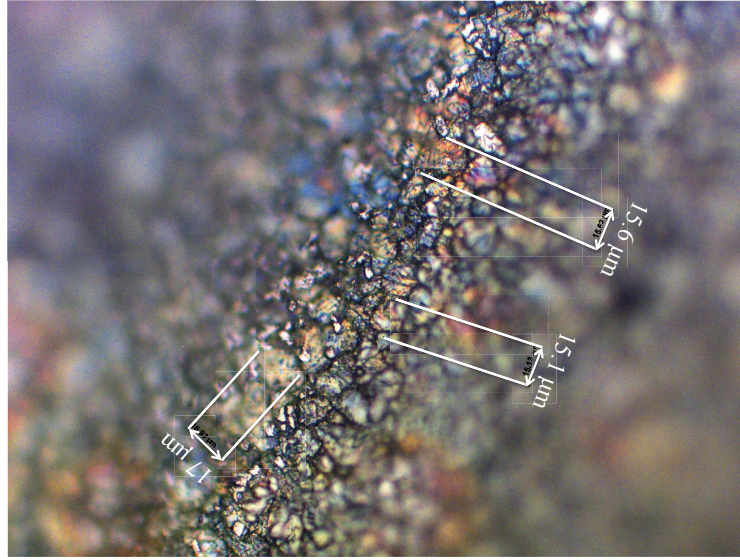
Figure B.2: Displayed is a 10x magnification of a region of the sample which has been both stressed due to the differential pressure across the sample and corroded. This region did not see any irradiation. The outer portions of the image are not in focus due to the curvature of the sample cause by doming.

is approximately 15 μm. The stressed region of the sample is difficult to image in the manner due to the doming caused by the differential pressure across the sample.

The sample's non-flat surface causes challenges for imaging at higher magnification. To acquire a smooth, focused image of the failure region a Z-stacking procedure was used. To compile the image, the microscope imaged in 1 μm slices in z through the damage area. Openly available software, ImageJ, was then used to stack the images according to intensity. The final image created provides a good image to investigate; see Figure B.3. Image to the left is taken at 20x magnification. The smaller of the grains in this region is measured at 74 μm. The image to the left in Figure B.3 is taken at 50x magnification and the grain size measured >100 μm.
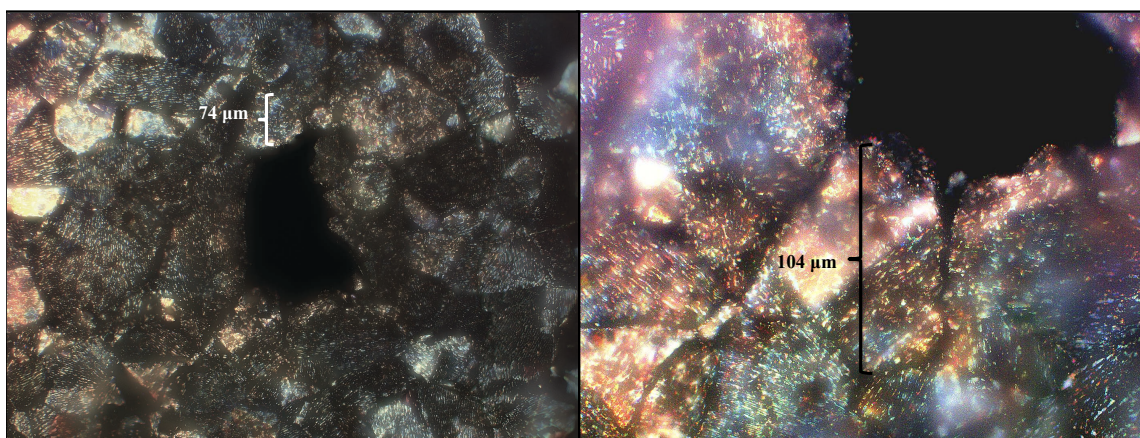
Figure B.3: The image displayed is a 10x magnification of the salt side of the SCID sample. The region imaged here is of the thicker area of the sample which is corroded, but has not been irradiation. Also, no appreciable stress is on this part of the sample as it is orders of magnitude thicker than the thinned, irradiation sample area.